Development and Analysis of Thermal Management Strategies to Improve Lithium-ion Battery Performance

By

Seham Shahid

A thesis submitted to the
School of Graduate and Postdoctoral Studies in partial
fulfillment of the requirements for the degree of

Doctor of Philosophy

in

Mechanical Engineering

The Faculty of Engineering and Applied Science

University of Ontario Institute of Technology (Ontario Tech University)

Oshawa, Ontario, Canada

January 2024

THESIS EXAMINATION INFORMATION

Submitted by: **Seham Shahid**

Doctor of Philosophy in **Mechanical Engineering**

Thesis title: Development and Analysis of Thermal Management Strategies to Improve Lithium-ion Battery Performance

An oral defense of this thesis took place on December 14, 2023 in front of the following examining committee:

Examining Committee:

Chair of Examining Committee	Dr. Amirkianoosh Kiani
Research Supervisor	Dr. Martin Agelin-Chaab
Examining Committee Member	Dr. Bale Reddy
Examining Committee Member	Dr. Xianke Lin
University Examiner	Dr. Hossam Gaber
External Examiner	Dr. Xili Duan, Memorial University

The above committee determined that the thesis is acceptable in form and content and that a satisfactory knowledge of the field covered by the thesis was demonstrated by the candidate during an oral examination. A signed copy of the Certificate of Approval is available from the School of Graduate and Postdoctoral Studies.

ABSTRACT

The transportation industry contributes more than a quarter of the global greenhouse gas emissions and transportation electrification was introduced as a means to decarbonize the industry. One of the major challenges related to the electrification of technologies are the thermal challenges associated with Lithium-ion batteries which are the leading candidate for electric batteries. In this research, these thermal challenges have been investigated with the objective of effective cooling and increased thermal uniformity within cylindrical Lithium-ion batteries. To achieve this, novel hybrid thermal management strategies have been proposed that combine air, liquid, and phase change material cooling systems. Several configurations of the proposed strategies are designed and analyzed through both experimental and numerical studies. The proposed hybrid strategies were able to limit the maximum temperature of the battery module to below ~29 ºC. The developed battery module also achieved the desired temperature uniformity to less than 5 ºC. Furthermore, the proposed hybrid strategies eliminate the requirement of a pump and reservoir system since there is no flow of liquid coolant within the battery module. This reduces the energy required for the operation of the thermal management system, thereby increasing the available energy for propulsion. Therefore, the proposed hybrid strategies and battery modules are capable of maintaining the thermal environment required by the Lithium-ion batteries for effective performance and can also be scaled to an entire battery pack for a range of applications.

Keywords: Battery thermal management; hybrid cooling; computational fluid dynamics analysis; heat transfer; cylindrical lithium-ion cells

AUTHOR'S DECLARATION

I hereby declare that this thesis consists of original work of which I have authored. This is a true copy of the thesis, including any required final revisions, as accepted by my examiners.

I authorize the University of Ontario Institute of Technology (Ontario Tech University) to lend this thesis to other institutions or individuals for the purpose of scholarly research. I further authorize University of Ontario Institute of Technology (Ontario Tech University) to reproduce this thesis by photocopying or by other means, in total or in part, at the request of other institutions or individuals for the purpose of scholarly research. I understand that my thesis will be made electronically available to the public.

SEHAM SHAHID

STATEMENT OF CONTRIBUTIONS

Part of the work described in this thesis has been published as:

Shahid, S., & Agelin-Chaab, M. (2023a). Comparison of Hybrid Cooling Concepts for Electric Battery Packs. *In Proceedings of the 10th International Conference of Fluid Flow, Heat and Mass Transfer, Carleton University, Ottawa, Canada*.

Shahid, S., & Agelin-Chaab, M. (2023b). Comparison of PCM Mediums for Hybrid Thermal Management of Electric Battery Packs. *In Proceedings of the 10th International Conference of Fluid Flow, Heat and Mass Transfer, Carleton University, Ottawa, Canada*.

Shahid, S., & Agelin-Chaab, M. (2023c). Development and Analysis of Hybrid Cooling Concepts for an Electric Battery Pack. *Journal of Energy Storage, 73(A)*, 108952. https://doi.org/10.1016/j.est.2023.108952

Shahid, S., & Agelin-Chaab, M. (2023d). Experimental and Numerical Analysis of a Hybrid Thermal Management Concept at Different Discharge Rates for a Cylindrical Li-ion Battery Module. *Batteries, 9(9),* 474. https://doi.org/10.3390/batteries9090474

Shahid, S., & Agelin-Chaab, M. (2023e). Comparison of Hybrid Cooling Concepts with PCM Cooling for Electric Battery Packs. *Journal of Fluid Flow, Heat and Mass Transfer*, *10*, 69-77. https://doi.org/10.11159/jffhmt.2023.010

Shahid, S., & Agelin-Chaab, M. (2023f). Comparison Between Different PCM Mediums and Dielectric Fluid for Hybrid Thermal Management of Electric Battery Packs. *Journal of Fluid Flow, Heat and Mass Transfer*, *10*, 62-68. https://doi.org/10.11159/jffhmt.2023.009

Shahid, S., & Agelin-Chaab, M. (2022). A review of thermal runaway characterization strategies for lithium-ion battery packs. *Energy Conversion and Management: X, 16*, 100310. https://doi.org/10.1016/j.ecmx.2022.100310

Shahid, S., & Agelin-Chaab, M. Experimental and Numerical Analysis of a Hybrid Cooling Concept for an Electric Battery Module. *International Journal of Heat and Fluid Flow* – Under Review

Shahid, S., & Agelin-Chaab, M. Phase Change Material Based Hybrid Thermal Management Strategies for Cylindrical Li-ion Cells. *e-Prime - Advances in Electrical Engineering, Electronics and Energy* – Under Review

Shahid, S., & Agelin-Chaab, M. Investigation of Thermal Properties of Phase Change Materials for Novel Hybrid Thermal Management Strategies for Cylindrical Li-ion Cells. *Applied Thermal Engineering* – Under Review

Shahid, S., & Agelin-Chaab, M. Experimental and Parametric Analysis of a Novel Hybrid Thermal Management Strategy for Cylindrical Lithium-ion Cells. *Heat Transfer* – Under Review

Shahid, S., & Agelin-Chaab, M. Investigation of Heat Transfer Enhancement Techniques on a Scalable Novel Hybrid Thermal Management Strategy for Lithium-ion Battery Packs. *Batteries* – Under Review

I conducted the literature review, developed the methodologies, and performed all the experimental and numerical studies and writing of the manuscripts.

ACKNOWLEDGEMENTS

I would like to express my earnest gratitude, appreciation, and respect to my teacher, mentor, and supervisor, Dr. Martin Agelin-Chaab, for his exemplary support, care, and guidance. He provided me with an outstanding research atmosphere and complete freedom to conduct my research which was significant for the completion of the thesis. As an outstanding academician his insightful comments, and challenging discussions and questions pushed me to think and see beyond by own capabilities and widened by research perspective. Due to his wise supervision, he educated and taught me about the various engineering and non-engineering concepts and theories, and instilled in me the immense passion for research and academics that he entails.

I am thankful to my colleagues at ACE3030B and to all my friends and relatives. Special thanks to all my professors during the course of my program at Ontario Tech University including Dr. Murat Aydin, Dr. Greg Rohrauer, and Dr. Anand Joshi and also to all my teachers and mentors throughout my education journey.

I am also thankful to my late grandmother, Mehrunnessa, for her utmost support and continuous prayers. I would also like to express my deepest gratitude, appreciation, and thankfulness to my caring parents, Shahid Mahmood and Nuzhat Seema, and my sibling and best friend, Hisham Shahid, for their limitless and continuous support, inspiration, prayers, and reassurances throughout my life. I am also thankful to my in-laws, Muhammad Mohsin Ali, Tehmina Jabeen, Muhammad Hassan Ali, and Sana Mohsin for all their support and prayers.

I would like to express my gratitude, appreciation, and love to my beloved wife, Maria Mohsin, for her immense support, love, care, patience, and prayers. She has stood by me for thick and thin

and I am very grateful to her. Finally, I would like to express my love and prayers for my son, Ibrahim Seham Alam, who has been the source of joy and happiness in our lives. I hope to serve them all and my community with the best of my abilities.

TABLE OF CONTENTS

LIST OF TABLES

LIST OF FIGURES

NOMENCLATURE

A	surface area (m^2)
Ar	Archimedes number (dimensionless)
a_i	specific surface area (m^2)
B	number of battery modules attached in series
c_P	specific heat capacity (J kg^{-1} K^{-1})
c_l	electrolyte concentration in the solution phase (mol m^{-3})
D	diffusion coefficient (m^2 s^{-1})
D_ω	cross diffusion term
E	energy (J)
E_i	equilibrium potential (V)
F	Faraday constant ($9.648456e^{04}$ C mol^{-1})
f	mean molar activity coefficient of the electrolyte
F_1	blending function in SST model
G_k	production of turbulent kinetic energy
G_ω	generation of specific dissipation rate

H	enthalpy (J)
h	sensible enthalpy (J)
h_j	specific enthalpy of species in specified phase (J g^{-1})
I_i	current (A)
j_i	specific reaction flux (mol m^{-2} s^{-1})
k	turbulence kinetic energy (J kg^{-1})
k_{eff}	electrochemical rate reaction constant (m s^{-1})
k_T	effective thermal conductivity (W m^{-1} K^{-1})
L	characteristic length (m)
L_H	latent heat (J)
m	mass (kg)
P	pressure (Pa)
Q	heat generation (W)
Q_p	polarization heat generation (W)
Q_{rea}	reversible heat generation by chemical reactions (W)
Q_c	electric contact heat generation (W)

Q_{ohm}	internal resistance heat generation (W)
R	electric resistance (ohm)
Re	Reynolds number (dimensionless)
S	user defined source term
Sc	Schmidt number (dimensionless)
S_m	volumetric heat sources
S_m	user defined function for continuity equation
S_r	strain rate magnitude
T	temperature (K)
t	time (s)
t_+	transport number
U	unit tensor
U_f	volume flux at specified timestep
V	battery working voltage (V)
Vol	volume (m^3)
y	nearest wall distance (m)

Y_k	dissipation due to turbulence for turbulent kinetic energy
Y_ω	dissipation due to turbulence for specific dissipation rate

Symbols

α^*	turbulent viscosity damping coefficient
α_q	volume fraction at specified timestep
β	liquid fraction
ϵ	turbulence dissipation rate (J kg^{-1} s^{-1})
$\vec{F}$	external body forces (N)
$\vec{g}$	gravitational acceleration (9.81 m s^{-2})
η_i	overpotential between adjacent anode and cathode layers (V)
σ	electric conductivity (S m^{-1})
σ_k	turbulence Prandtl number for turbulence kinetic energy
σ_ω	turbulence Prandtl number for specific dissipation rate
$\Delta\phi_{SEI}$	is the voltage drop result from the SEI film resistance (V)
ϕ_s	electric potential (V)
ϕ_e	electrolyte potential (V)

ρ	density (kg m^{-3})
Γ_k	effective diffusivity of turbulence kinetic energy
Γ_ω	effective diffusivity of specific dissipation rate
$\bar{\bar{\tau}}$	stress tensor
μ	dynamic viscosity (Pa s)
$\vec{v}$	velocity (m s^{-1})
ω	specific dissipation rate (s^{-1})

Subscripts

a	ambient air
b	battery
cc	connector contact
eff	effective
i	tensor indices
SEI	solid electrolyte interface
x	x-direction
y	y-direction

z	z-direction

Acronyms

ARC	accelerating rate calorimetry
BEV	battery electric vehicle
BM	battery module
BTMS	battery thermal management system
CAD	computer aided-design
CC	constant current
CFM	cubic feet per minute
CPCM	composite phase change material
CV	constant voltage
DAQ	data acquisition device
DC	direct current
EG	expanded graphite
ESC	external short circuit
EV	electric vehicle

EV-ARC	extended volume accelerating rate calorimetry
GcN	graphene coated nickel
GHG	greenhouse gas
HEV	hybrid electric vehicle
HP	heat pipes
ISC	internal short circuit
LCO	lithium cobalt oxide
LFP	lithium iron phosphate
Li-ion	Lithium-ion
LiPo	lithium polymer
LMO	lithium manganese oxide
NI	National Instrument
NiCd	nickel cadmium
NiMH	nickel metal-hydride
NMC	lithium nickel manganese cobalt oxide
PAO	poly-alpha-olefin
PCM	phase change materials

PEM	performance enhancing materials
PHEV	plug-in hybrid electric vehicle
RSD	relative standard deviation
SEI	solid electrolyte interface
SOC	state of charge
SST	shear stress transport
TNT	2, 4, 6 – trinitrotoluene

CHAPTER 1: INTRODUCTION

This chapter provides the background and overview of the thermal management of Lithium-ion (Li-ion) batteries. It is followed by the motivations and the objectives of this thesis. Finally, the structure of the thesis is described. The contents of this chapter have been partially taken from the candidate's published work (Shahid & Agelin-Chaab, 2022).

1.1. Background

Climate change due to greenhouse gas (GHG) emissions is of great concern around the world. Technological advancements have paved the way for cleaner renewable energy conversion processes with increased efficiencies (Goodenough, 2015). The key challenge posed by renewable sources is their intermittency, which requires effective energy storage systems to ensure reliability. This is resulting in the shift in focus of energy storage systems from fossil fuels to electrochemical systems (Shan et al., 2016). These transformations, combined with strict emission regulations, are the driving force in electrifying the transportation industry as it contributes 29% to GHG emissions (EPA, 2021).

There are two types of electric vehicles (EVs), namely, fuel cell electric vehicles (FCEV) and battery electric vehicles (BEV). BEVs are powered by electric battery packs, and their efficiency is directly dependent on the performance of the battery pack. Li-ion batteries are the leading candidate chemistry for the automotive industry due to their high energy and power density, low self-discharge rate, and extended lifecycle (Omar et al., 2014; Sefidan et al., 2017; Saw et al., 2018). Amongst a variety of Li-ion chemical compositions, the most common compositions include $LiMn_2O_4$, $LiCoO_2$, and $LiFePO_4$ (Zhao et al., 2011; Julien et al., 2014; Shan et al., 2014).

However, the issue of range anxiety poses a significant obstacle in the mass adoption of BEVs. Therefore, researchers and BEV companies are developing cathode and anode material combinations to increase the energy density of Li-ion batteries (Feng et al., 2018).

In order to achieve the targets, the cathode should have lithium-based nickel-rich or manganese-rich material, and the anode should be changed from pure carbon to a combination of silicone and carbon. However, such materials with higher energy densities have low thermal stabilities (Noh et al., 2013), which can lead to safety issues such as thermal runaway.

Thermal runaway of Li-ion batteries is the phenomenon of exothermic chain reactions within the battery. These reactions usually cause a sharp increase in the internal battery temperature causing the inner structures of the battery to destabilize and degrade, which can lead to the total failure of the battery. Thermal runaway can occur from various forms of mechanical, electrical, and thermal abuse. All of these lead to an internal short-circuit of the battery as the separator between the anode and the cathode either collapses, tears down, or is pierced. This generates a high amount of heat, which in turn intensifies the degree of electrochemical reactions causing excessive heat generation. This cycle continues, which increases the temperature of the battery sharply and releases large amounts of flammable gases. The release of gases causes an increase in the internal pressure of the battery resulting in the expansion of the outer casing, causing potential explosion and fire to the battery (Finegan et al., 2017; Mao et al., 2018; Chen et al., 2019).

1.2. Motivation

Cylindrical Li-ion cells, when compared to other cell geometries, have the advantage of increased mechanical stability and ease of manufacturing. They can be produced relatively faster, hence, more kWh per cell can be produced in a day resulting in lower manufacturing cost per kWh (Shahid, 2017; Wei, 2018). Furthermore, if a single cell fails then the impact on the overall energy and power availability for the battery pack is low (Shahid, 2017; Wei, 2018). However, cylindrical cells have certain thermal challenges. The ideal operating range for the Li-ion cells is 25 °C to 40 °C (Rao & Wang, 2011; Jaguemont et al., 2016). Below 25 °C the energy output of the cell reduces due to increased internal resistance. Whereas above 40 °C the degradation rate of the cell increases, which decreases its lifespan (Saw et al., 2018). However, the range of -10 °C to 50 °C is considered as a tolerable operating range (He & Ma, 2015). Moreover, temperature non-uniformity in the battery pack reduces its power capacity and causes an imbalance in the discharging and charging rates of the cells (Hoh & Fuhr, 2009). Degradation of 30% to 50% occurs when the variation of the temperature ranges from 10 °C to 15 °C (Saw et al., 2016). Worse still, very high temperatures may result in the thermal instability of the cell due to irreversible chemical reactions with a potential for thermal runaway to occur with the associated safety issues (Yang et al., 2016). Hence, solutions and strategies are required to maintain the operating temperature within the acceptable range.

1.3. Objectives

The main goal of the thesis is to propose, develop and analyze effective thermal management strategies and configurations that can improve thermal management of cylindrical Li-ion batteries. The specific objectives are as follows:

1) Develop effective thermal management strategies for Li-ion batteries to prevent and mitigate thermal runaway through effectively maintaining the cell temperatures within the acceptable operating range and improving temperature non-uniformity. The proposed thermal management strategies should have:
    - low pumping power requirements,
    - modularity for easy upscaling or downscaling of the battery pack.
2) Conduct comprehensive experimental studies to evaluate and analyze the novel strategies.
3) Conduct numerical studies through computational fluid dynamics to:
    - analyze and evaluate multiple developed strategies,
    - compare the thermal performance and effectiveness of the thermal management strategies,
    - investigate the thermal performance with changing operating conditions and system parameters.
4) Perform parametric studies to determine feasible design parameters of the developed strategies.
5) Perform a scalability study to determine the application of the developed strategies in a range of applications.

1.4. Thesis Structure

This thesis is organized into 5 chapters as follows:

Chapter 1 provides the background and overview for the thermal management of Li-ion batteries. This is followed by the motivations and the objectives of this thesis.

Chapter 2 presents the literature review on the thermal management of BEV batteries. It provides a background on the types of BEV batteries followed by the different variants of Li-ion battery chemistries and structures, and the heat generation within the cell. This is followed by a review of the mechanisms through which the thermal runaway occurs and propagates through the battery pack. Additionally, a review on the thermal management strategies for the Li-ion batteries is presented. Followed by techniques and strategies developed to mitigate thermal runaway in case it occurs. Finally, the gaps in the literature are discussed.

Chapter 3 presents the proposed hybrid thermal management strategies followed by various proposed configurations. This is followed by the experimental and numerical techniques. The experimental setups are given that clarify the types of equipment that were employed, followed by the procedures adopted to conduct successful experiments. An uncertainty analysis is conducted to record the errors and uncertainties in the experimental equipment. Finally, the numerical methodology is described that includes the governing equations, mesh generation and the boundary conditions used for all the studies.

Chapter 4 presents the results and discussions that were obtained from the experiments and numerical simulations. It is divided into 16 subsections. The initial sections provide the validation of the numerical model, feasibility of the proposed strategies, comparison on the developed

configurations, and discussion on the experimental results. The intermediate sections provide an analysis of the proposed strategy at different discharge rates obtained through experiments, comparison of multiple proposed strategies, analysis on the impact of changing ambient temperatures, discussion on the effects of adding performance enhancing materials (PEM) to phase change materials (PCM), and comparison on the effect of using nano-fluids to enhance thermal properties. The final sections provide a discussion on the parametric study used to reduce the amount of PCM, fluid, and the airflow Reynolds number, analysis on increasing the heat transfer area within the air duct, and the scalability aspect of the battery module and hybrid strategy.

Chapter 5 presents the summary of results and discussions, novelty and contributions of this thesis, and the limitations and recommendations for future work.

CHAPTER 2: LITERATURE REVIEW

This chapter presents the literature review on the thermal management of BEV batteries. It provides a background on the types of BEV batteries followed by the different variants of Li-ion battery chemistries and structures. The heat generation within the Li-ion cell is then described. This is followed by a review of the mechanisms through which thermal runaway occurs and propagates through the battery pack. Additionally, a review is provided on the thermal management strategies used to regulate the temperature at the cell and pack levels. These thermal management strategies are required to ensure the temperature does not increase substantially, resulting in thermal runaway. This is followed by techniques and strategies developed to mitigate thermal runaway in case it occurs. Finally, the gaps in the literature are presented. The contents of this chapter have been partially taken from the candidate's published paper (Shahid & Agelin-Chaab, 2022).

2.1. Electric Vehicle Battery Background

Initially, the BEVs were developed and powered using lead-acid batteries based on their cost-effectiveness and slow self-discharge rates. Nevertheless, owing to significant developments in the field of batteries, high energy density and low weight ratio chemistries were industrialized (Kalhammer et al., 2007). Recently, the BEV battery candidates in the market include Li-ion, Nickel metal-hydride (NiMH), Nickel-Cadmium (NiCd), Lithium Polymer (LiPo), and lead-acid batteries. Compared to nickel-based batteries Li-ion batteries are the leading candidate in the automotive industry due to their high energy and power density, low self-discharge rate, and extended lifecycle (Omar et al., 2014; Sefidan et al., 2017; Saw et al., 2018). A comparison of the different battery chemistries is provided in Table 2.1.

Table 2.1: Comparison of cell chemistries (Huat, 2014).

Parameters	**Lead-Acid**	**NiCd**	**NiMH**	**Li-ion**
Nominal Voltage (V)	2.0	1.2	1.2	3.6
Energy Efficiency (%)	65	80	85	95
Energy Density (Wh/L)	60	150	200	230
Specific Power (W/kg)	130	200	250	330
Specific Energy (Wh/kg)	30-50	45-80	60-120	100
Self-Discharge (%/month)	5	25-30	30-35	<10
Lifecycle	200-300	500-1000	300-500	1000
Cost	Low	Low	Medium	High

2.2. Li-ion Battery Chemistry and Structure

The Li-ion battery consists of four major components which include electrolyte, anode, cathode, and separator. The naming of the Li-ion battery is based on the material of the cathode. Most common cathodic material include, Lithium Cobalt Oxide (LCO), Lithium Iron Phosphate (LFP), Lithium Nickel Manganese Cobalt Oxide (NMC), and Lithium Manganese Oxide (LMO) (Schalkwijk & Scrosati, 2002; Berini et al., 2014). A comparison of the different cathodic material is provided in Table 2.2.

Table 2.2: Comparison of Li-ion cell cathode material (Ohzuku & Brodd, 2007; Bandhauer et al., 2011; Huat, 2014).

Parameters	**LFP**	**LCO**	**LMO**	**NMC**
Nominal Voltage (V)	3.3	3.6	3.8	3.6/3.7
Upper Voltage Limit (V)	3.6	4.2	4.2	4.2
Specific Energy (Wh/kg)	90-120	150-190	100-135	140-180
Thermal Runaway (°C)	270	150	250	210
Lifecycle	1000-2000	500-1000	500-1000	1000-2000

The anodic materials in the Li-ion batteries include graphite, graphene, meso-carbon, hard carbon, lithium-silicide, lithium titanate oxide, microbeads, and lithium germanium (Schalkwijk & Scrosati, 2002). However, graphite is commonly used due to a high specific capacity of 372 mAh/g and coulombic efficiencies of greater than 95% (Yoshio et al., 2009).

The electrolyte in the Li-ion batteries is used as a medium to allow the ions to shuffle during the anodic and cathodic redox reactions (Dhameja, 2001). It is a blend of the electrolytic salts and organic solvents. The electrolytic salts include lithium trifluoro methane sulfonyl methide, lithium triflate, lithium tetrafluoroborate, and lithium hexafluorophosphate, and the organic solvents include ethyl carbonate, dimethyl carbonate, diethyl carbonate, and propylene carbonate. The most

used electrolyte is 1M Lithium Hexafluorophosphate / Ethyl Carbonate due to its high electrical conductivity (Berini et al., 2014).

The separator in a Li-ion battery is slotted in between the cathode and anode. Its function is to prevent physical contact between the electrodes all the while allowing the Li-ion to flow freely between them. The separator could increase the electrical resistance and the density of the battery which negatively impacts the battery's performance (Zhang, 2007). Therefore, selection of proper separator material is crucial. The commonly used separator materials include polypropylene and polyethylene. Its porosity can vary between 30 – 50% and size of pores can vary from 0.03 – 0.1 μm. Another function of the separator is to act as a thermal fuse by shrinking and restricting the flow of the Li-ions through its pores at high temperatures. The commonly used separators have a melting temperature of 165 °C and are capable of shutting down the reaction at 130 °C (Zhang, 2007).

2.3. Heat Generation within Electric Batteries

The heat is generated in a Li-ion cell through polarization, internal resistance, connection resistance, and reversible heat through chemical reactions (Smith & Wang, 2006; Saw et al., 2013; Yang et al., 2015). The internal resistance is a combination of electrical (active material in electrode and current collector) and ion (electrolyte) conductive resistance, and solid electrolyte interface (SEI) film resistance on the negative electrode. Therefore, the heat source equations are complex (Yang et al., 2015). The general thermal equation for a lumped battery model is stated in the following equation (Smith & Wang, 2006; Saw et al., 2013; Yang et al., 2015):

$$\rho c_P \frac{\partial T}{\partial t} = \nabla \cdot k_T \nabla T + Q_p + Q_{rea} + Q_c + Q_{ohm} \tag{2.1}$$

Where;

ρ is the density,

c_p is the specific heat capacity,

k_T is the effective thermal conductivity of active electrode material,

T is the temperature,

Q_p is the polarization heat generation,

Q_{rea} is the reversible heat generation by chemical reactions,

Q_c is the electrical contact heat generation,

Q_{ohm} is the internal heat generation.

The heat generations terms are specified in the following equations:

$$Q_p = a_i j_i F \eta_i \tag{2.2}$$

$$Q_{rea} = a_i j_i F T \frac{dE_i}{dT} \tag{2.3}$$

$$Q_c = \frac{\left(I_i^2 \frac{R_{cc}}{A_{cc}}\right)}{Vol} \tag{2.4}$$

$$Q_{ohm} = \sigma_{eff,i}\left(\frac{\partial \phi_{s,i}}{\partial x}\right)^2 + k_{eff,i}\left(\frac{\partial \phi_{e,i}}{\partial x}\right)^2 + \frac{2k_{eff,i}RT(1-t_+)}{F}\left(1 + \frac{dlnf}{dlnc_l}\right)\frac{\partial lnc_l}{\partial x}\frac{\partial \phi_{e,i}}{\partial x} + a_i j_i F \Delta\phi_{SEI} \tag{2.5}$$

Where;

a_i is the specific surface area,

j_i is the specific reaction flux,

F is the Faraday constant,

η_i is the overpotential between adjacent anode and cathode layers,

E_i is the equilibrium potential,

I_i is the product of a_i, j_i, F,

R_{cc} is the electrical resistance of connector contact,

A_{cc} is the connector contact area on the terminal,

v is the volume of cylinder cell,

σ_{eff} is the effective electric conductivity,

k_{eff} is the electrochemical reaction rate constant,

ϕ_s is the electric potential,

ϕ_e is the electrolyte potential,

R is the electrical resistance,

t_+ is the transport number,

f is the mean molar activity coefficient of the electrolyte,

c_l is the electrolyte concentration in the solution phase,

$\Delta\phi_{SEI}$ is the voltage drop result from the SEI film resistance.

Commonly a simplified equation for heat generation is used which is expressed as (Abdul-Quadir et al., 2014; Liu et al., 2014):

$$Q_{Total} = I_i(E_i - V) - I_i T \frac{dE_i}{dT} \tag{2.6}$$

Where;

Q_{Total} is the cell's total heat generation,

I is the current applied.

The term $I_i(E_i - V)$ is an integration form of Equation 2.2. It calculates the irreversible heat generated by the over potential of the circuit which captures the polarization and internal resistance heat generation. The term $I_i T \frac{dE_i}{dT}$ is an integral of Equation 2.3 which captures the reversible heat generation due to the chemical reaction of the cell (Abdul-Quadir et al., 2014; Liu et al., 2014).

The heat generated within the Li-ion cells should be removed effectively, as higher temperatures within the cell lead to additional exothermic reactions, which generate more heat, thereby increasing the temperatures further and creating a positive feedback mechanism (Spotnitz & Franklin, 2003; Feng et al., 2015; Feng et al., 2015a; Coman et al., 2016). This sharp increase in temperatures can lead to safety issues within the battery pack, such as thermal runaway and, in some extreme cases, fire and explosion.

2.4. Thermal Runaway Mechanisms

2.4.1. Mechanical abuse

The two common characteristics of mechanical abuse are destructive deformation and destructive displacement due to an applied force. When a vehicle collides or crashes, the battery pack is likely to either be crashed or penetrated by an external object. This causes the separator between the cathode and anode of the battery to tear away, resulting in an internal short circuit (ISC).

The mechanical abuse phenomenon from a structural point of view was investigated by Zhu et al. (2020). An experimental study on quasi-static loads, low-velocity punch penetration, and wedge-cutting tests were carried out. The battery module consisted of 18 sub-assemblies and two cover plates at the top and the bottom of the battery pack. The sub-assemblies included pouch batteries, cooling plates and cushions. It was concluded that the punch penetration test resulted in higher forces and increased absorption of energy due to the higher degree of material densification. Similarly, Hu et al. (2020) conducted an experimental study on 18650 Li-ion batteries to study the effects of the dynamic collision and quasi-static compression. The results showed that cylindrical batteries in a pack behave differently than individual batteries under crushing scenarios. In the battery pack, the failure occurs due to the nonuniformity in the deformation within each battery, creating various susceptible areas in the gaps of the batteries. Under quasi-static compression, the battery pack deforms uniformly, and the failure of the individual batteries is distributed uniformly. Whereas under the dynamic collision, the batteries in the pack are deformed row by row, and the force is concentrated in specific rows, which results in increased damage to the batteries under the same crushing displacement, causing a higher risk of failure. The authors additionally conducted a numerical study to understand the dynamic collision scenario further. The results indicated that

the dominating property in the dynamic collision was the crushing velocity rather than the crushing energy. Once the crushing velocity exceeds 20 m/s, the battery pack failure switches from initial failure at the last row to initial failure at the first row.

In addition to the crushing mechanisms, the penetration mechanisms also cause ISC, which leads to the thermal runaway of the Li-ion batteries. Yamauchi et al. (2004) investigated the penetration mechanism and concluded that the electrical energy of the battery is constantly released during the ISC caused by penetration. The temperature of the battery also continuously increases by the heat generation due to the ISC until the complete discharge of the battery. At the end of this process, if the temperature fails to reach the critical level, then there is no thermal runaway. In another study, Maleki and Howard (2009) examined the discharging of the battery under the ISC caused by the penetration mechanism. The results concluded that within the first minute of ISC, 70% of the energy was released, due to which a sharp temperature increase was noticed. Additionally, the location of the battery penetration also affects the thermal runaway characteristics. For example, in instances where the penetration occurred at low heat dissipation locations, the risk of thermal runaway increased significantly. To understand the flow of current during the penetration mechanism, Zavalis et al. (2012) developed a two-dimensional (2D) numerical model for a prismatic battery and studied the mechanism. The results of the study concluded that the maximum temperature increase during the thermal runaway was restricted by the mass transport of Li-ions in the electrolyte. Moreover, there are two mechanisms through which a short circuit occurs during penetration. In the first mechanism, the current passes through the penetrating object (ISC) and in the second mechanism, the current passes through the electrodes (external short circuit). When the penetration occurs, 75% of the current passes through the electrodes, and 25% passes through the penetrating object. Moreover, Zhao et al. (2016) studied the effects of the capacity of the battery

on the ISC during the nail penetration process. The results concluded that with the increase in the battery capacity, the current flow increased at the nail penetration location. This led to extensive heat generation which subsequently caused thermal runaway.

Zhu et al. (2022) conducted mechanical abuse studies on the Li-ion jelly rolls and prismatic batteries under quasi-static loads. Hemispherical nose, round edge wedge, and flat end indenters were used to apply the loads on both types of batteries. For jelly roll batteries, the hemispherical nose and flat end indenters showed a penetration type commonly seen in porous media with a hole at the contact point followed by a tunnel. With the round edge wedge indenter, a "/" and "V" crack appeared on each layer of the jelly rolls. Similar results were seen by using the hemispherical nose and flat end indenters on the prismatic batteries. However, with the wedge indenter, the enclosure of the prismatic battery was not penetrated when the same force was applied. The results from the experiments also showed that once the ISC occurs on the first layer of the jelly roll, the entire battery fails.

2.4.2. Electrical abuse

The external short circuit (ESC) of the batteries is considered one of the causes of electrical abuse. It occurs either due to exposure to water, conductor contamination, electric shock, or the deformation of the battery during mechanical abuse. The ESC was investigated by Leising et al. (2001), where the current was increased to its peak value and then rapidly decreased to a plateau before reducing to zero to complete the discharge process of the battery. The temperature increased sharply with the increase in current. Once the plateau current was reached, there was no further increase in temperature; hence, the thermal runaway did not occur. In order to trigger thermal runaway due to an ESC, either the mass transfer coefficient for Li-ion at the anode or the surface

area of the anode had to be increased. Both cases cause a higher current flow and subsequently rapid heat generation (Spotnitz & Franklin, 2003). On the contrary, overcharging the Li-ion battery can lead to worse thermal runaway consequences due to the excessive energy in the battery. Once the battery is overcharged, the heat generation increases, and large amounts of joule heating and side reaction heating at the anode and the cathode occurs, resulting in a sharp increase in the battery temperature (Zeng et al., 2006; Ye et al., 2016).

Ohsaki et al. (2005) studied the LCO prismatic batteries with a graphite anode. Several gases, including CO_2, CO, C_2H_6, C_2H_4, and H_2 were released during the overcharge of the batteries. The volume of gases increased with the increase in the temperature of the battery. The results also showed that once the temperature of the battery increased beyond 60 °C the exothermic oxidation reaction at the electrolyte increased quickly, causing the overall battery temperature to increase sharply. The authors concluded that the thermal runaway occurred due to the violent reaction between the overcharged anode (lithium deposition) and the electrolyte solvent at a high temperature which occurs due to the exothermic reaction between the cathode and electrolyte.

Yuan et al. (2015) studied the behavior of the prismatic battery under overcharge conditions. The internal and external temperatures of the battery were monitored. The results showed that when the battery is overcharged to the maximum voltage of 5.10 V, the internal temperature of the battery goes up to 50 °C, and electrolyte oxidation occurs. With further overcharge (> 180% State of Charge), the interface between the cathode and electrolyte becomes highly reactive, and the internal temperature of the battery increases above 200 °C. The thermal runaway occurs due to the lithium plating on the anode during the overcharge of the battery. Ye et al. (2016) conducted an experimental study on prismatic batteries. The results indicated that the side reactions result in an

80% heat generation during overcharge. Furthermore, if the charging current is more than 1 C, then effective cooling methods should be employed within 2 minutes once the inflection point voltage is surpassed to prevent thermal runaway. The maximum internal temperature during thermal runaway exceeds 660 °C. Mao et al. (2019) conducted an experimental study to analyze the changes in the internal composition of the batteries. The results showed that thermal runaway is more likely to be triggered under adiabatic conditions rather than under ambient environmental conditions. It was also concluded that the cathode is prone to get highly reactive when the battery is overcharged to 150% state of charge (SOC), and the heat generated and released was 1026.4 J/g.

To supplement the studies of overcharge effects on the Li-ion batteries, Hamisi et al. (2022) developed a 2D electrothermal model for 18650 cylindrical batteries. Through the numerical studies, it was found that the heat distribution within the battery tends to stay uniform. The total heat generation rate increases with increasing the overcharge current due to an increase in the joule heating of the battery. Finally, with a 5 C charging current, the battery surface temperature increases sharply compared to lower C-rate charging currents.

Yeh et al. (2022) further studied the overcharge mechanism and its effects on the separator of the Li-ion batteries. The separators are usually manufactured using thermoplastic materials. The composite material consists of polypropylene/polyethylene/polypropylene layers. During overcharge, once the temperature rises, the irregular crystalline structure of the polyethylene layer melts, resulting in interface disturbance and partially blocking the Li-ion channel. This causes the Li-ion to follow through alternate channels, which results in a sharp increase in the voltage.

2.4.3. Thermal abuse

The causes of thermal abuse within Li-ion batteries and battery packs include overheating due to mechanical and/or electrical abuse and overheating due to improper connections and contacts of batteries. The thermal abuse causes an increase in the battery's internal and external temperatures, which can melt the separator between the anode and the cathode, resulting in ISC. This increases the temperature quickly, risking a potential thermal runaway.

Feng et al. (2014) conducted extended volume-accelerating rate colorimetry (EV-ARC) tests on large format prismatic batteries. The results indicated that the thermal runaway occurs approximately at 520 °C. The instantaneous temperature rise occurs about 15 - 40 s from the sharp drop in voltage. Additionally, before thermal runaway, the internal resistance of the battery increases from 20 - 60 mΩ. Once thermal runaway occurs, the internal resistance rises to 370 mΩ. which indicates the melting of the separator and the swelling of the battery.

Wu et al. (2018) conducted an accelerated rate colorimetry (ARC) test to compare the thermal runaway of prismatic batteries under internal and external heating modes. The results indicated that the duration of the thermal runaway reduces as the operating current increases in the internal heating mode. On the contrary, the duration decreases as the SOC increases during external heating mode. However, in both heating modes, the voltage drops sharply a few minutes before the rapid temperature rise. The onset and critical temperature are higher in the external heating mode compared to the internal heating mode.

Zhao et al. (2020) conducted EV-ARC test of cylindrical batteries by using different SOC and cycling times to study the thermal runaway hazards. The battery was subjected to a ramp heating method to depict thermal abuse conditions. The results showed that the internal pressure and the

maximum surface temperature of the battery increased with the SOC increase when thermal runaway occurred. The authors calculated the energy release of the completely charged fresh battery to be 61.72 kJ. This energy release is equivalent to a 5.57 g, 2,4,6-trinitrotoluene (TNT) explosive. Additionally, aged batteries, when compared to fresh batteries, are more prone to trigger thermal runaway.

Chandra et al. (2022) also conducted thermal abuse EV-ARC experimental tests on high energy density cylindrical Li-ion batteries. To facilitate the increase in the driving range, higher energy density batteries are required. The authors measured heat release values, internal pressure, and temperatures. The mean peak values extracted from the experiment were 753 °C for the surface temperature, 1080 °C for the internal battery temperature, 3.6 kW of heat, and 4.56 bar of internal pressure during the thermal runaway.

In addition to heating the batteries, thermal abuse also occurs due to lose contact with battery connectors. For example, Beauregard (2008) reported an investigation into the thermal runaway accident of a Toyota Prius battery pack. It was discovered that the batteries in the pack were connected using metal connectors. Due to vehicle vibrations, the connector became loose for one of the batteries. This resulted in increased current passing through the loose connector, causing excessive heat generation, and subsequently triggering thermal runaway.

2.4.4. Thermal Runaway Propagation

Once the thermal runaway is triggered at the battery level by one of the mechanisms stated in the previous section, it is then propagated throughout the BEV battery pack. To prevent thermal runaway, it is essential to study, characterize and understand the propagation behavior for all types of Li-ion batteries, including cylindrical, prismatic and pouch batteries. One of the initial studies

was conducted by Feng et al. (2015b). The first battery in the battery pack was penetrated, and the effects on the neighboring batteries were examined. The results showed a temperature variation of up to 791.8 °C within a battery. Additionally, 12% of the heat generated by the first battery is required to trigger a thermal runaway in the adjacent battery. It was also observed that 90% of the heat is expelled through the shell of the battery, and only 10% is transferred through the pole connector.

Chen et al. (2019) conducted an experimental study to analyze thermal runaway propagation mechanisms. Two battery packs were developed using cylindrical batteries. The first battery pack consisted of 35 batteries and one heater to trigger thermal runaway in a 6 × 6 configuration. The second battery pack consisted of 99 batteries and one heater in a 10 × 10 configuration. Once thermal runaway occurred, it was observed that a maximum of 6 batteries ignited at the same time in the first battery pack and 32 batteries in the second battery pack. The battery pack with a higher number of batteries resulted in a greater average mass loss rate.

Li et al. (2019) conducted an experimental study on large format prismatic batteries to analyze the thermal runaway propagation behavior in a battery pack consisting of 5 batteries. The results showed that the thermal runaway was initially triggered on the front surface layer of the battery. The average propagation time in a single battery with 100% SOC was 10 s, whereas for a battery with 50% SOC was 39 s. As expected, the battery with 100% SOC showed a more intense combustion behavior. Moreover, the propagation time between adjacent batteries in the battery pack was 87 s for 100% SOC and 307 s for 50% SOC batteries.

Zhong et al. (2018) performed a series of experiments to investigate thermal runaway propagation using cylindrical batteries. A heater was used to trigger the thermal runaway. It was observed that

it took 240 to 280 s for thermal runaway to propagate between the battery layers within the battery pack. Additionally, batteries with 50% SOC released greater amounts of inflammable gases rather than violent flames. However, once the gases were on fire, the combustion went on for longer due to increased amounts of gases.

Huang et al. (2016) conducted an experimental study on battery packs containing large format Li-ion batteries. The batteries were arranged in rhombus and parallel layouts. It was observed that the fire-impingement caused the temperature of the batteries to increase between the range of 200 °C and 900 °C. This temperature increases in the batteries resulted in a rapid temperature rise within the battery module and caused thermal runaway. The results also indicated that the critical temperature to trigger thermal runaway was between 126.1 °C and 139.2 °C. This critical temperature range was calculated using the Semenov and Frank-Kamenetskii models.

Weng et al. (2021) conducted an experimental study on the effects of the concentration level of oxygen and nitrogen, and argon gases in efforts to mitigate thermal runaway. The study showed that by reducing the concentration of oxygen from 21 to 12%, the thermal runaway propagation rate was reduced by 44%. Moreover, through the application of inert gases, it was found that the thermal runaway propagation was delayed.

2.5. Battery Thermal Management Systems (BTMS)

Battery thermal management systems (BTMS) are developed to extract the heat away from the battery during its operation and to prevent thermal runaway. The principle for BTMS is to maintain the temperature of the battery between the optimum operating ranges of 25 °C to 40 °C (Rao & Wang, 2011; Jaguemont et al., 2016) and to keep the variation between the maximum and minimum temperature at battery and pack level to less than 5 °C (Hoh & Fuhr, 2009).

2.5.1. Air Cooled BTMS

Air is one of the traditional cooling mediums used in BTMS, mainly due to its lightweight structure and low development and maintenance costs. The limited use of air-cooled BTMS in the current BEVs in the market is due to its limited heat removal from the batteries, as it has a low thermal conductivity and heat capacity (Wei & Agelin-Chaab, 2019). To enhance its effectiveness and efficiency, the battery arrangement and the placement of the air inlet and exhaust are to be carefully designed.

Yang et al. (2015) performed a numerical study by developing a thermal model to investigate the different arrangements of cylindrical batteries in the battery pack. The configuration of the battery packs investigated is 10 × 6. The results concluded that batteries in the aligned structure exhibit better thermal performance compared to the batteries in the staggered structure. This was also concluded by the study conducted by Fan et al. (2019). Zhao et al. (2015) conducted a detailed parametric study on cylindrical batteries to understand the various ventilation types, inlet velocities, spacing between adjacent batteries, and the effect of ambient temperature. The results concluded that when the airflow is reversing, the flow of air between adjacent battery rows is not

effective compared to unidirectional airflow. It is to be noted that airflow between adjacent battery rows is different from the reciprocating airflow systems.

Wang et al. (2014) studied the thermal performance of cylindrical batteries under various arrangements within the battery pack. The arrangements investigated were 5 × 5, 3 × 8, and 1 × 24 arrays, 19 batteries in a hexagonal arrangement, and 28 batteries in a circular arrangement. In addition to this, various air inlet and exhaust locations were studied. The results concluded that the optimum cooling performance is when the inlet is placed at the top of the battery pack, and the exhaust is placed at the bottom of the battery pack. In terms of battery arrangements, the hexagonal structure offers the optimum space utilization in the battery pack, however, the cubic structure (5 × 5 array) provides the best cooling within the battery pack.

Unidirectional airflow normally has low-temperature uniformity at the battery and pack level. Within the battery pack, the batteries near the air inlet have low temperatures, and the batteries near the exhaust have high temperatures. This is due to the air's heat extracting capacity gradually reducing as it extracts heat from the batteries one by one. At the battery level, the surface area at the windward side of the airflow interacts with a greater volume of air as compared to the surface area at the leeward side. This results in a temperature non-uniformity between the windward side and the leeward side of the battery. To counter this, and increase temperature uniformity, reciprocating airflow was developed and investigated by Mahamud and Park (2011). The results showed that 120 s is the optimum reciprocating interval to achieve 4 °C of the temperature difference between the minimum and maximum temperatures. Liu et al. (2015) also conducted a parametric study on the reciprocating airflow, and the results concluded that the air velocity should be 6 m/s, the reciprocation period 67.5 s, and the inlet temperature 10 °C to achieve a temperature

variation of 3.76 °C. However, the issue with reciprocating airflow is that it is an active system, and timing valves are incorporated into the BTMS, which increases the complexity of the system resulting in low reliability and high cost (Tong et al., 2016).

Shahid and Agelin-Chaab (2018a) conducted numerical and experimental studies to develop a passive air-cooled BTMS to achieve the desired thermal performance. The results showed that the highest cooling and temperature uniformity is achieved when the inlet is placed at the top of the battery pack and the exhaust at the bottom of the battery pack. This conclusion also falls in line with studies in the open literature (Wang et al., 2014; Wang et al. 2015; Saw et al., 2017). A parametric study was then conducted to obtain the optimum dimension of the inlet plenum and to analyze the impact of increasing Reynolds number on thermal performance. The results concluded that the most effective Reynolds number was 7,440 (2018b). Additional passive techniques were developed that included vortex generators and jet inlets. These were incorporated into the battery pack to improve the airflow at the leeward side of the battery, and significant improvements were observed (2017). Furthermore, a numerical study was conducted to eliminate the secondary inlet, as it was observed to increase the volume of the battery pack. In order to achieve the desired cooling and temperature uniformity, the configuration of the jet inlet array and multiple vortex generators was enhanced. Through this, a temperature distribution of less than 5 °C was achieved (2019).

Zhao et al. (2019) developed an air-cooling system by adding air tubes around every cylindrical battery and providing air to each of the tubes through an inlet orifice. This ensured that fresh air was available to each battery, thereby eliminating the issues of unidirectional flow. The results showed that with an inlet pressure of 100 Pa, orifice diameter of 1.5 mm, and discharge rate of 3

C, the maximum temperature reduced from 325.9 K to 305.7 K when compared with the no cooling condition. The temperature difference was also maintained within 3 K.

2.5.2. Liquid Cooled BTMS

Liquids generally have higher heat capacities and thermal conductivities when compared with air. Liquid cooling is categorized into direct and indirect BTMS. In direct BTMS, an electrically insulating liquid is used in direct contact with the batteries, and thermal management is very effective (Park & Jung, 2013; Patil et al., 2020; Dubey et al., 2021). However, the pumping power is greatly increased due to the increased viscosity of liquids relative to air. Moreover, a risk factor linked to the leakage of the liquid is high, especially in large battery packs. To counter these issues, the indirect BTMS was developed in which the liquid is constrained within cold plates. These cold plates are then placed in direct contact with the batteries (Panchal et al., 2017). Currently, cold plate usage is applicable to prismatic and pouch batteries as it easily embodies the rectangular shape of these batteries (Panchal et al., 2015, 2017). Furthermore, cold plates for cylindrical batteries were studied by Zhao et al. (2015), however, the complexity of the structure increased greatly due to the difficulty of manufacturing cylindrical cold plates.

Rao et al. (2017) developed a liquid-cooled BTMS for cylindrical batteries using a variable-length aluminum block for each of the batteries. The liquid tubes ran through the entire length of the battery row, passing within the aluminum blocks. The results showed that when compared with uniform length aluminum block, the temperature uniformity increased by 6% for 1 mm length increment, 14% for 2 mm length increment, and 28% for 3 mm length increment.

Zhao et al. (2019) developed various liquid cooling configurations for cylindrical batteries. Amongst them, two approaches showed considerable improvements in the temperature uniformity

of the battery pack and batteries. The first approach was shortening the liquid flow path by using multiple serpentine flow channels, and the second approach was increasing the contact surface area between the serpentine channel and the batteries along the streamwise direction. The temperature uniformity was maintained at less than 2.2 K by using the first approach and to less than 0.7 K by using the second approach.

Li et al. (2021) developed a novel "fork" type mini-channel cold plate for prismatic batteries. The authors conducted a numerical study and compared the parallel flow and cross flow plates. The results were further optimized using multi-objective optimization, and it was found that cross flow plate achieved a better thermal performance by reducing the thermal resistance by 20.23% and the power requirements and pressure drop by 39.44%. This enhancement in the cooling ability is due to the formation of the eddies in the shunt channel and thereby increasing the mixing in the flow channel. The authors also concluded that to maintain the temperature uniformity within the 5 °C limit, a flowrate of 48 mL/s is required per cold plate.

The mixing in the fluid flow is also studied numerically by Monika et al. (2021) using Tesla valves in a cold plate. The Tesla valve introduces reverse flow in a single channel that increases the mixing of the fluid flow and introduces turbulence in the flow. The results showed that a maximum temperature of 35.1 °C and a temperature difference of 0.35 °C can be achieved by varying the Reynolds number from 2500 to 5500.

In addition to conventional fluids being used for liquid cooling, researchers have also used nano-fluids to enhance the thermal properties of the working fluids. Sefidan et al. (2017) used water-Al_2O_3 nano-fluid as the liquid medium, and various battery pack structures were examined. The results showed that the maximum temperature in the battery pack increased by 8 K above the inlet

temperature. The authors also reported that for the system to work effectively, certain measures need to be considered. A wired connection, if placed under the nano-fluid could be easily damaged and must be protected by using mini-channels. The nanoparticles can stick to each other and cause clustering, which significantly reduces the thermal performance of the nano-fluid. Finally, the boiling point of the nano-fluid and its container should be considered during the design process.

The issue with liquid cooling is that it increases the weight of the system and the operating power of the system. The flow requirement of liquid cooled BTMS can go as high as 10 L/min (He et al., 2017). The energy requirement to pump the liquid subsequently reduces the state of charge (He et al., 2017).

2.5.3. Phase Change Material (PCM) Based BTMS

The use of PCM as a cooling medium is a relatively recent development in BTMS compared to air and liquid. It extracts the heat from the batteries using the latent heat of the PCM. It was initially proposed by Al-Hallaj and Selman (2000). Javani et al. (2015) investigated the effects of PCM on square batteries. The results showed that by using PCM, temperature uniformity was achieved over the battery submodule. The PCM also kept the temperature of the batteries within the safe operating temperature. Rao et al. (2011) used the PCM to reduce the temperature of rapidly degrading batteries. It was found that the thermal conductivity increases as the melting temperature of the PCM decreases, resulting in a lower maximum temperature of the battery. Jiang et al. (2017) developed a tube-shell battery pack consisting of expanded graphite (EG) / paraffin composite PCM (CPCM). The results showed that the CPCM maintained the temperature within the range of 41 to 44 °C during a 5 C discharge process. In comparison, for a forced air cooling with an air inlet velocity of 1 m/s, the battery temperatures reached 72 °C. The temperature uniformity was also

kept within the range of 1 to 2 °C with the CPCM. He et al. (2018) performed experimental studies, and the results showed that 7% of EG in a paraffin based CPCM was the optimum proportion. Additionally, the temperature difference using the CPCM was 2.82 °C compared to 14.49 °C of air-cooled BTMS. Hussain et al. (2018) developed a novel PCM, graphene coated nickel (GcN) foam saturated with paraffin. The thermal conductivity was enhanced by 23 times compared to pure paraffin. The temperature rise of the battery was reduced by 17% using GcN foam saturated with paraffin when compared to nickel foam at 1.7 A discharge current.

Al-Zareer et al. (2017b) developed a thermal management system using propane (fossil fuel) as the PCM medium. This was developed specifically for hybrid electric vehicle (HEV) as the propane available to generate power for the HEV can be used as PCM during its storage stage. In this system, the cylindrical batteries are partially submerged in propane, which extracts heat from the batteries. This results in the boiling of the propane liquid. The vapors then extract heat from the rest of the top part of the batteries. The results from the study showed that at 8.5 bar pressure, 5% of the battery needs to be submerged to maintain the battery temperatures below 39 °C for a discharge rate of 7.5 C for 600 s. Moreover, by submerging 30% of the battery in propane, the temperature is maintained below 34 °C. The results also showed that by increasing the pressure from 8.5 bar to 10 bar, the temperature uniformity of the battery increases; however, the maximum temperature also increases. Propane was also used for prismatic batteries by Al-Zareer et al. (2018a). The results concluded that with 5% submerged area and 8.5 bar pressure, the maximum temperature was maintained below 35 °C. This study was further developed by incorporating electrochemical modeling and performance evaluation of a new ammonia-based BTMS for electric and hybrid electric vehicles using ammonia instead of propane for ammonia-powered HEV. The results concluded that to maintain the temperature below 40 °C, the pressure must be set at 9 bar,

and the submerged area will be 5% (2017a). The challenge with this approach is that once the liquid evaporates and extracts heat from the top portion of the batteries, its heat extracting capability reduces. If another BTMS is not employed to extract heat away from the evaporated liquid, then this approach will subsequently fail after several charging/discharging cycles. Later, this method was developed for prismatic batteries in which the ammonia was placed under cooling tubes of the cold plate. The results of the study concluded that at 4 C discharging rate, the temperature was maintained below 28 °C with one tube within the cold plate. By increasing the number of tubes to 10, the maximum temperature was maintained below 25 °C, and the temperature variation was maintained within 3 °C (2018c). Another variation was developed by changing the fluid to R134a in order to be used by BEVs. The results showed that by submerging the battery 20% into the fluid, the temperature uniformity of 7 °C was achieved (2018b). The BTMS for prismatic batteries was further developed by using hydrogen as the cooling medium in a cold plate. The results concluded that by keeping the inlet temperature of hydrogen at 10 °C and inlet velocity of 0.01 m/s, the temperature was maintained under 30.5 °C. Additionally, the temperature uniformity was maintained below 7 °C (2018d).

Zhao et al. (2017) coupled the PCM with heat pipes (HP) rather than using air or liquid to cool the PCM. The results showed that the maximum temperature was maintained below 50 °C for longer times. It was reduced by 33.6% by only adding the PCM to the battery pack. An additional reduction of 28.9% was achieved by coupling the PCM with HP. Additionally, the temperature uniformity was also maintained below 5 °C for longer in the PCM/HP BTMS. Jilte and Kumar (2018) also studied the flow of refrigerants to cool cylindrical batteries. The refrigeration cycle was employed, and the results showed that the systems maintained the maximum temperature

below 35 °C at an extreme ambient temperature of 40 °C. However, for this system to work, the refrigerant should be monitored closely to not reach its superheated state in its flow path through the battery pack. Panahi et al. (2021) also worked on heat pipes by developing micro heat pipe arrays. The study showed that the orientation of the heat pipe array plays a vital role in the thermal performance of the system. With the condenser placed at a lower position (also known as the positive angle), the temperature rises to unacceptable levels. At the same time, the performance of the system improves with negative angles and when the capillary forces are aligned with gravity.

PCM is still not widely used within the industry due to its limitations in the overall heat transfer coefficients. This issue arises when a secondary cooling system is required to extract the heat from the PCM itself once its latent heat absorption capacity is utilized.

2.5.4. Hybrid BTMS

To overcome the restrictions imposed by pure air cooling or liquid cooling BTMS, a hybrid system is introduced and developed by researchers. Saw et al. (2018) conducted a study to introduce mist cooling into the battery pack. The results showed that to keep the battery surface temperature below 40 °C, 3% mist and 5 g/s mass flowrate is required. Wang et al. (2017) placed cold plates at the base of the cylindrical batteries. The air is recycled in the battery pack case using a fan for recirculation. The structure with the fan placed under the cold plate resulted in a fully developed flow field. Compared with traditional battery pack cooling methods, the maximum temperature was reduced by 3.45 K, and the temperature uniformity coefficient increased by 2.42 times.

Ling et al. (2015) developed a hybrid system by combining EG/paraffin PCM with forced-air cooling. An optimization study was conducted through which the mass of the PCM was reduced by 94.1% and the volume by 55.6%. The results also showed that for a battery pack with 20 Li-

ion cylindrical batteries, the maximum temperature was limited to 37 °C and the temperature uniformity to less than 3 °C. Wei and Agelin-Chaab (2018, 2019) conducted an experimental study by combining water evaporation, convective, and conductive effects. The water flows through capillary action within channel strips placed between the batteries. Airflows axially and is cooled by flowing over the channel strips. This allows the air to regain its heat extracting capacity from the batteries towards the exhaust of the battery pack. The developed hybrid BTMS showed an improvement of 56% in temperature uniformity and 20% in battery pack cooling.

Shahid and Agelin-Chaab (2021) conducted a study in which a hybrid technique was developed by adding liquid jackets to each of the batteries. The liquid within the jacket was in direct contact with the batteries. A numerical study was conducted with the inclusion of vortex generators, and jet inlet arrays developed earlier (Shahid & Agelin-Chaab, 2017, 2018a, 2018b, 2019) to distribute the airflow. The results showed a substantial increase in temperature uniformity. The temperature difference was reduced at the pack level to 1.26 °C and at the battery level to 0.36 °C. Zhang et al. (2019) developed a hybrid BTMS by combining PCM and liquid cooling. A cold plate was placed at the base of the cylindrical batteries, and the liquid was passed axially through the cold plate. The results showed that under cyclic working conditions, the maximum temperature of the battery was maintained below 50 °C and the temperature uniformity was within 3.4 °C. Additionally, Chen et al. (2021) conducted experimental studies on prismatic batteries by combining liquid cooling with PCM cooling. A reasonable agreement is required between the flowrate of the liquid and the thickness of the PCM is required to achieve an optimum thermal performance of the system. Based on the results of their study, this was achieved by setting the liquid flowrate as 54 mL/min and the thickness of PCM as 0.65 mm. Using these values, the maximum temperature reached by the batteries was 34.8 °C and the temperature uniformity was within 1 °C.

Table 2.3: Summary of research on BTMS.

Cooling Medium	Battery Shape	Type of Study	Major Findings	References
Air	Cylindrical	Numerical	Batteries arranged in aligned structure are better compared to staggered structure.	(Fan et al., 2019; Yang et al., 2015)
Air	Cylindrical	Numerical & Experimental	Cubic structure of cells provides optimum cooling.	(Wang et al., 2014)
Air	Cylindrical	Numerical	~4 °C of temperature uniformity is achieved using reciprocating airflow.	(Mahamud & Park, 2011; Liu et al., 2015)
Air	Cylindrical	Numerical & Experimental	Highest cooling is achieved with inlet placed at the top and exhaust at the bottom.	(Wang et al., 2014, 2015; Saw et al., 2017; Shahid & Agelin-Chaab, 2018a;)
Air	Cylindrical	Numerical & Experimental	Temperature uniformity of <5 °C is achieved by adding vortex generators and jet inlets in the unidirectional airflow.	(Shahid & Agelin-Chaab, 2017, 2019)
Air	Cylindrical	Numerical & Experimental	Temperature uniformity of 3 °C is achieved by adding air tubes around every battery.	(Zhou et al., 2019)
Liquid	Cylindrical	Numerical	Temperature uniformity of < 5 °C is achieved by using a variable aluminum block with a 3 mm gradient of linear relationship.	(Rao et al., 2017)
Liquid	Cylindrical	Numerical	Temperature uniformity of 0.7 °C is achieved by increasing the contact surface area of batteries.	(Zhao et al., 2019)
Liquid	Prismatic	Numerical	"Fork" type cold plate is developed. It requires flowrate of 48 mL/s to achieve < 5 °C temperature uniformity.	(Li et al., 2021)

Liquid	Prismatic	Numerical	Mixing the liquid using Tesla valves improves cooling and temperature uniformity.	(Monika et al., 2021)
Liquid	Cylindrical	Numerical	To use nano-fluids the clustering should be avoided, wires should be protected, and boiling point of the nano-fluid should be considered.	(Sefidan et al., 2017)
PCM	Cylindrical	Experimental	7% of EG in a paraffin-based CPCM is the optimum proportion.	(He et al., 2018)
PCM	Cylindrical	Experimental	Novel PCM, graphene coated nickel (GcN) foam saturated with paraffin is developed, which has a 23 times greater thermal conductivity compared to pure paraffin.	(Hussain et al., 2018)
PCM	Cylindrical & Prismatic	Numerical	Novel strategy is developed using liquid PCM including propane, ammonia, R134a, and hydrogen. Various combinations of pressure, temperature, and volume of liquid are required to maintain the optimum operating temperatures.	(Al-Zareer et al., 2017a, 2017b, 2018a, 2018b, 2018c, 2018d)
PCM	Cylindrical	Numerical	To use refrigerants for cooling the superheated state should be avoided.	(Jilte & Kumar, 2018)
Hybrid (Mist Cooling)	Cylindrical	Numerical	3% mist and 5 g/s mass flowrate is required to maintain temperature < 40 °C.	(Saw et al., 2018)
Hybrid (Air & Liquid)	Cylindrical	Experimental	Novel strategy is developed by combining water evaporation, convective, and conductive effects.	(Wei & Agelin-Chaab, 2018, 2019)

Hybrid (Air & Liquid)	Cylindrical	Numerical	Liquids jackets were added to each battery and passive air-cooling techniques were used to achieve 1.3 °C temperature uniformity.	(Shahid & Agelin-Chaab, 2021)
Hybrid (Liquid & PCM)	Prismatic	Experimental	Temperature uniformity of 1 °C is achieved by setting the liquid flowrate to 54 mL/min and PCM thickness to 0.65 mm.	(Chen et al., 2021)

2.6. Thermal Runaway Mitigation

There have been various research and developments for the Li-ion BTMS designs to prevent thermal runaway. However, there are still chances of thermal runaway occurrences (Hallaj & Selman, 2000; He et al., 2017; Saw et al., 2018). Therefore, mitigation strategies are required to contain and reduce the damage when thermal runaway occurs.

2.6.1. Thermal Runaway Mitigation Mechanism

Thermal runaway in a battery pack can lead to fire hazards. The fire occurs when the mixture of battery fuel and oxidizer is exposed to high heat sources. The combustion can be halted through the following mechanisms:

- shielding the fuel mixture from the oxygen,
- interrupting the reactions causes combustion,
- segregating the fuel mixture from the ignition area,
- reducing the temperature of the fuel mixture below the flash point of the mixture,
- removing the thermal runaway gases from the high temperature areas.

There are five types of basic extinguishants used to extinguish battery fires. These include water, foam, carbon dioxide, powder/dry powder, and halon based extinguishants. The most cost-effective method is the use of water based extinguishants (Farrington, 2001; Reif et al., 2010). The latent heat of evaporation and the high heat capacity of water is advantageous in eliminating battery pack fires. There are four different types of water based extinguishants; water jet, water spray or sprinkler, water with added surfactants, and water mist. The water jet applies a jet stream of water to the battery directly. Water spray or sprinkler forms water droplets. Each droplet is surrounded

by air which reduces the risk of short circuits when applied to electrical components. The droplets should have enough momentum so that they can penetrate the fire plume and interact with the burning surface. Water mist consists of water droplets that are smaller than that from the spray. These smaller droplets have a larger ratio of surface area to volume, which result in increased heat absorption. Finally, surfactants in the water reduce the surface tension of water, increasing the efficacy of the extinguisher by coating the burning materials and cooling them. However, water is an electrical conductor and can cause ESC in the battery, which can result in the propagation of thermal runaway (Ghiji et al., 2020).

Foam-based extinguishants use foam to place a battier between the high temperature surface and flammable vapors/gases. However, to be effective, the foam must completely cover the surface of the battery and eliminate any air to pass through the foam barrier and ignite. Powder-based extinguishers chemically alter the reactions causing the fire. This method does not provide any form of cooling, and therefore, it has a high risk of re-ignition of the fuel. Carbon dioxide based extinguishers replace oxygen with carbon dioxide and are safe to use in electrical components. However, due to its low cooling capacity, it is not considered the ideal extinguishant. Additionally, if used in closed enclosures, it can cause breathing issues for the occupants of the enclosure. Halon based extinguishers also chemically interrupt the fire reactions and do not leave residuals behind. However, similar to powder-based extinguishers halon-based extinguishers do not provide any form of cooling. Moreover, halons, when exposed to the environment, cause global warming, and deplete the ozone layer (Ghiji et al., 2020).

2.6.2. Thermal Runaway Mitigation Strategies

One of the important mitigation strategies is to develop fire extinguishing methods to suppress the Li-ion battery fires. Recently, gas extinguishing agents have been used to suppress battery fires. These extinguishing agents include dodeca-fluoro-2-methylpenttan-3-one ($C_6F_{12}O$), hepta-fluoropropane (HFC-227ea), and carbon dioxide (CO_2) (Rao et al., 2015; Wang et al., 2015, 2018; Liu et al., 2018). These agents can rapidly extinguish the flames without initiating electrical fire. Wang et al. (2015) examined the effect of HFC-227ea. It was found that the agent was able to quickly extinguish the fire, however, the temperature did not decrease as the exothermic reactions were still in progress. This resulted in re-ignition of the batteries. Liu et al. (2018) examined the effects of $C_6F_{12}O$ extinguishing agent, and the results showed that the fire was extinguished quickly without re-ignition of the battery. However, the cooling was insufficient, and the temperature was very high. This high temperature could cause thermal runaway propagation to neighboring batteries as well.

Some studies have found that water and aqueous agents have the potential to extinguish fires and improve the cooling effect on Li-ion batteries (Larsson et al., 2014; Blum & Long, 2015; Zhu et al., 2018; Liu et al., 2020; Xu et al., 2020; Zhang et al., 2021). Zhang et al. (2021) examined the effects of water spray (mist cooling) on the thermal runaway of Li-ion batteries. The results concluded that it could effectively extinguish the fire and reduce the surface temperature of the batteries as well. To prevent the propagation of the thermal runaway 20.8 g W/h consumption was required. Similarly, a study by Liu et al. (2020) found that to prevent thermal runaway propagation in 18650 cylindrical batteries, water consumption of 0.195 g W/h is required. Xu et al. (2020) conducted a study on mist cooling as well. It was found that the water spray can reduce the maximum temperature of the battery by 133 °C. This was a superior agent in terms of cooling

when compared with the CO_2 and HFC-227ea extinguishing agents. Zhu et al. (2018) also conducted a similar study and found that by adding a ratio of surface-active agents to the water spray, the temperature can reduce rapidly, and the fire extinguishing time can be greatly reduced. Liu et al. (2019) conducted an experimental study on water mist cooling of Li-ion batteries at various SOC. The results concluded that the thermal runaway could be controlled and contained if the water spray was released before the battery temperature reached the critical temperature. The critical cooling rate of water mist is 1.87 times the critical heating rate at 25% SOC, whereas, at 100% SOC, this rate goes up to 4.98 times. However, once the critical temperature is reached, the results show that thermal runaway is unstoppable.

Mist cooling can be effective in containing thermal runaway fires; however, its drawbacks were outlined in the study conducted by Larrson et al. (2014). It was reported for prismatic Li-ion batteries that when the power of the fire is small, then water mist is very effective in reducing the maximum temperature of the battery and extinguishing the fire. But when the power of the fire is large, then due to the generation of a thermal plume, it is difficult for the water mist particles to penetrate the smoke and reach the fire base. To counter this problem, Zhang et al. (2020) combined the gas extinguishing agent, $C_6F_{12}O$, CO_2, and HFC-227ea, with water mist to contain thermal runaway. The results showed that the combination of $C_6F_{12}O$ and water mist provided the optimum cooling of the battery and extinguishing of the fire. Additionally, when considering the economic benefits, then CO_2 combined with water mist was the best choice.

Various research has also been conducted on the application of PCM to contain thermal runaway (Wu et al., 2017; Zhi & Jian, 2020; Zhang et al., 2021). Weng et al. (2019) used PCM with aerogel to contain thermal runaway in battery packs. Multiple experiments were performed by the authors to investigate the dissipation capacity of heat and thermal insulation capacity. The results

concluded that PCM with EG extinguished the flame effectively and reduced the maximum temperature of the battery; however, the thermal runaway propagation accelerated. Implementing the aerogel felt results in better thermal performance as it delays the thermal runaway propagation. Moreover, the aerogel felt is better at thermal insulation when compared to aerogel powder. The drawback is that it marginally reduces the maximum temperature of the battery. A combination of the PCM and aerogel provides better mitigation of thermal runaway by delaying the propagation by 173 s.

Wilke et al. (2017) used PCM to mitigate thermal runaway during nail penetration. In scenarios where the short circuit between parallel batteries was not induced by nail penetration, a gap of 2 mm was sufficient between the batteries. In this case, the temperature of the neighboring battery reached 189 °C, which is still at dangerous levels. By using the PCM, the temperature of the neighboring battery was reduced to 109 °C. Even with a short circuit, by using the PCM, the temperature of the neighboring battery was maintained below 120 °C, thereby containing thermal runaway propagation. Kshetrimayum et al. (2019) integrated PCM with cold plates for cylindrical cell battery packs to mitigate thermal runaway. The results concluded that to prevent heat propagation to the neighboring batteries, a 3.9 L/min flowrate of water and counter-current flow between the cold plates was required.

Weng et al. (2022) developed and experimentally studied CPCM with flame retardant additives, as majority of the PCM currently used are flammable and can burn in thermal runaway scenarios where fire occurs. Due to a higher mass fraction of flame-retardant additives in the PCM, the cooling performance is reduced. However, the flame-retardant additives are capable of reducing the heat release rate of the batteries and delaying the ignition once thermal runaway occurs.

Mohammed et al. (2019) designed a cooling plate for prismatic batteries with a staggered pin arrangement to disperse the coolant over the surface of the cooling plate. The coolant used in the cooling plate is 60% ethylene glycol mixed in water. With an inlet temperature of 20 °C, the surface temperature of the battery can be maintained below 25 °C with a flowrate of 0.2 L/min. However, during thermal runaway, the flowrate needs to be increased to 30 L/min to contain it.

2.7. Gaps in the Literature

Extensive research has been conducted in developing advanced battery thermal management strategies for preventing and mitigating thermal runaway. In industry, currently, liquid cooling is being used in BEVs with cylindrical cells. The power requirements for pumping liquid through the battery pack are high. This power requirement is fulfilled by the battery pack, thereby reducing the range of the BEV. Additionally, the cooling pipes usually run in series through the cells in the battery pack. This can result in temperature non-uniformity in the battery pack as the cells near the inlet of the cooling pipe are cooler compared to cells near the outlet of the battery pack. Moreover, a secondary cooling system is required to remove heat from the liquid coolant. On the contrary, PCM cooling is effective at improving the temperature uniformity of the battery pack by using the latent heat, however, a secondary liquid cooling system is required to remove the heat from the PCM once the latent heat is completely used up. This increases the weight as well as the power requirements of the system. Finally, air cooling has the lowest weight and power requirements, however, it has limitations due to low thermal capacity and low heat transfer rates. To overcome these challenges with individual cooling systems, research is being conducted into hybrid cooling systems. Evaporative cooling systems that introduce water vapors in the airflow have shown promising results during the normal operations of the batteries (Wei & Agelin-Chaab, 2018, 2019). Even though these systems reduce the power requirements of the system, the temperature non-uniformity is not significantly reduced when applied to a large number of cells as these are series systems. Therefore, research needs to be conducted on hybrid cooling strategies that are capable of reducing the power requirements of the cooling system and simultaneously maintaining the temperature of the cells within the optimum operating range to improve temperature uniformity both at the cell and pack levels.

CHAPTER 3: METHODOLOGY

This chapter presents the proposed hybrid thermal management strategies followed by various proposed configurations based on the hybrid strategies. This is followed by the experimental and numerical techniques. The experimental setups are given that clarify the types of equipment that were utilized, followed by the procedures adopted to conduct successful experiments. Two different types of experiments were undertaken. In the first experiment, a single Li-ion cell was used to measure the heat flux at the surface of the cell. In the second experiment, the battery module was manufactured, and the temperature measurements were obtained. An uncertainty analysis is conducted to record the errors and uncertainties in the experimental equipment. Finally, the numerical methodology is described that includes the governing equations, mesh generation and the boundary conditions used for all the studies. The contents of this chapter have been partially taken from the candidate's published work (Shahid & Agelin-Chaab, 2023a, 2023b, 2023c, 2023d).

3.1. Proposed Hybrid Thermal Management Strategies

Based on the objectives set in Section 1.3, novel hybrid thermal management strategies are designed and developed. The strategies consist of a combination of air cooling, liquid cooling, and PCM cooling systems. PCM is considered as the primary coolant whereas liquid and air are considered as the secondary coolants. The strategies are described in the following sub-sections. In order to develop the strategies, the following design considerations and assumptions are considered:

- The battery module should have a high temperature uniformity.
- The fluid pumping power should be eliminated.
- It should have modularity for scalability.
- Airflow through the duct is incompressible and the temperature of air at battery module inlet is at ambient temperature.
- The fluid in liquid cooling is incompressible and the temperature of the fluid at the start of the discharge process is at ambient temperature.
- There is no leakage of fluid from liquid cooling components.
- The battery module is kept at atmospheric pressure.

3.1.1. Strategy 1: Liquid Channels

Strategy 1 is designed as shown in Figure 3.1. The fluid is placed in a reservoir that sits at the base of the module. Liquid channels are connected to this reservoir. The cells are placed above the liquid reservoir. The PCM is filled into the empty cavity surrounding the cells and liquid channels. Finally, an air duct is placed on top of the cells and PCM through which the airflows.

Strategy 1 will work in three stages. In the first stage, the heat generated from the cells is absorbed by the PCM material using latent heat during the phase change process. In the second stage, the heat from the PCM is extracted by the fluid within the liquid channels. In the third stage, the airflow within the air duct then removes any vapors from the battery module into the environment and cools the fluid in the liquid channels. The fluid in the channel will also be topped up through capillary action if required.

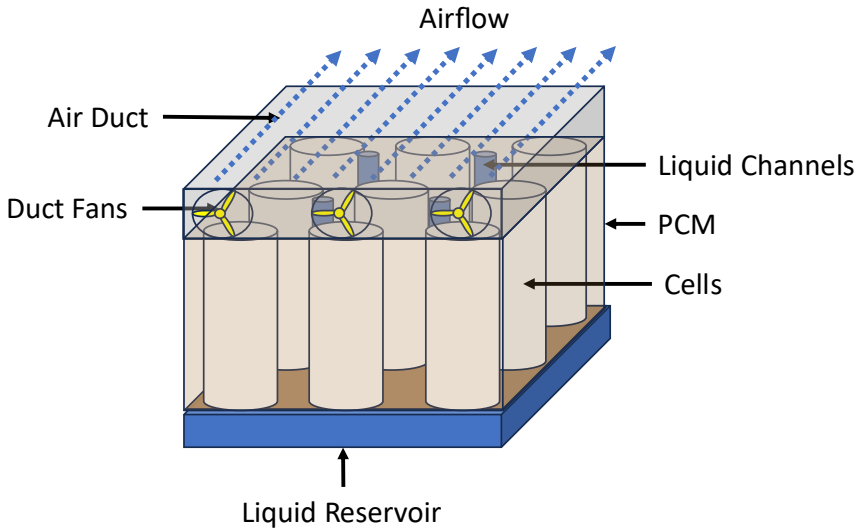

Figure 3.1: Three-dimensional (3D) schematic of proposed hybrid thermal management strategy 1.

3.1.2. Strategy 2: Cold Plates

Strategy 2 is designed by modifying Strategy 1 as shown in Figure 3.2. The liquid reservoir and channels are replaced with a cold plate. The fluid is enclosed and sealed within the cold plate. The PCM is filled into the empty cavity surrounding the cells and the cold plates. Finally, the placement of the air duct is the same as in Strategy 1. However, in Strategy 2 the cold plate protrudes into the air duct.

Strategy 2 will also work in three stages. In the first stage, the heat generated from the cells is absorbed by the PCM material using latent heat during the phase change process. In the second stage, the heat from the PCM is extracted by the fluid within the cold plate. In the third stage, the heat within the fluid is extracted through air cooling within the air duct. Since the fluid is enclosed within the cold plate therefore, the fluid selection is not limited to environmentally friendly fluids. Moreover, there is no consumption of the fluid in this strategy, which eliminates the requirement of the reservoir and the pump.

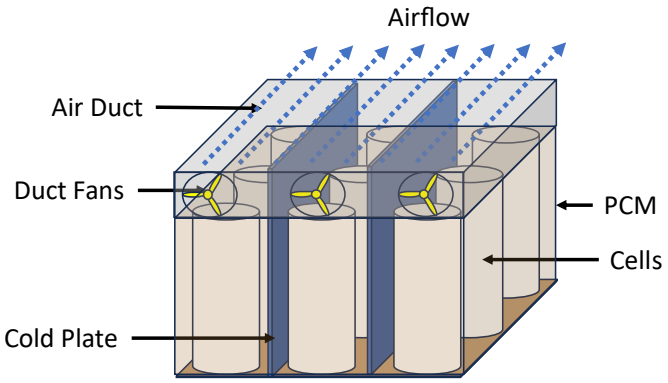

Figure 3.2: 3D Schematic of proposed hybrid thermal management strategy 2.

3.2. Battery Module Configurations

The proposed strategies in Section 3.1 are utilized to develop the configurations for the battery module. Each battery module consists of nine commercial cylindrical 18650 Li-ion cells. The specification of the cell is provided in Table 3.1. The primary PCM is paraffin as its phase change temperature is suitable for Li-ion cells, it is non-toxic and non-corrosive, and it has a high latent heat capacity and chemical stability (Mishra et al., 2022). The configurations are developed according to the specific studies and are provided in the sub-sections below.

Table 3.1: Samsung INR18650-25R cell specifications (SSDICo., 2014).

Parameters	**Specifications**
Nominal discharge capacity (mAh)	2,500
Nominal voltage (V)	3.6
Standard charge (A)	1.25 A, (0.125 A cut-off)
Maximum continuous discharge (A)	20
Discharge cut-off voltage (V)	2.5
Cell weight (g)	45
Cell height (mm)	65
Cell diameter (mm)	18
Cathode material	$LiNiMnCoO_2$
Anode material	Graphite

3.2.1. Feasibility Study of Strategy 1

In order to establish the feasibility of the proposed Strategy 1 three types of configurations are developed and investigated. The baseline battery module configuration (BM1) is a passive configuration and consists of cylindrical cells that are surrounded by paraffin (PCM), as shown in Figure 3.3. The material properties of air, water, and paraffin are shown in Table 3.2. This

configuration is purely based on PCM cooling with no additional form of liquid and air cooling to take the heat away from the PCM.

Table 3.2: Material properties of air, water, and paraffin (Peng et al., 2022).

Material Properties	**Air**	**Water**	**Paraffin**
Density (kg/m^3)	1.225	998.2	880
Specific Heat (J/kg.K)	1,006	4,182	2,150
Thermal Conductivity (W/m.K)	0.0242	0.6	0.21
Viscosity (kg/m.s)	0.000018	0.001003	0.00312
Latent heat (J/kg)	-	334,000	245,000
Solidus Temperature (K)	58	273.15	303.15
Liquidus Temperature (K)	61	273.15	305.15

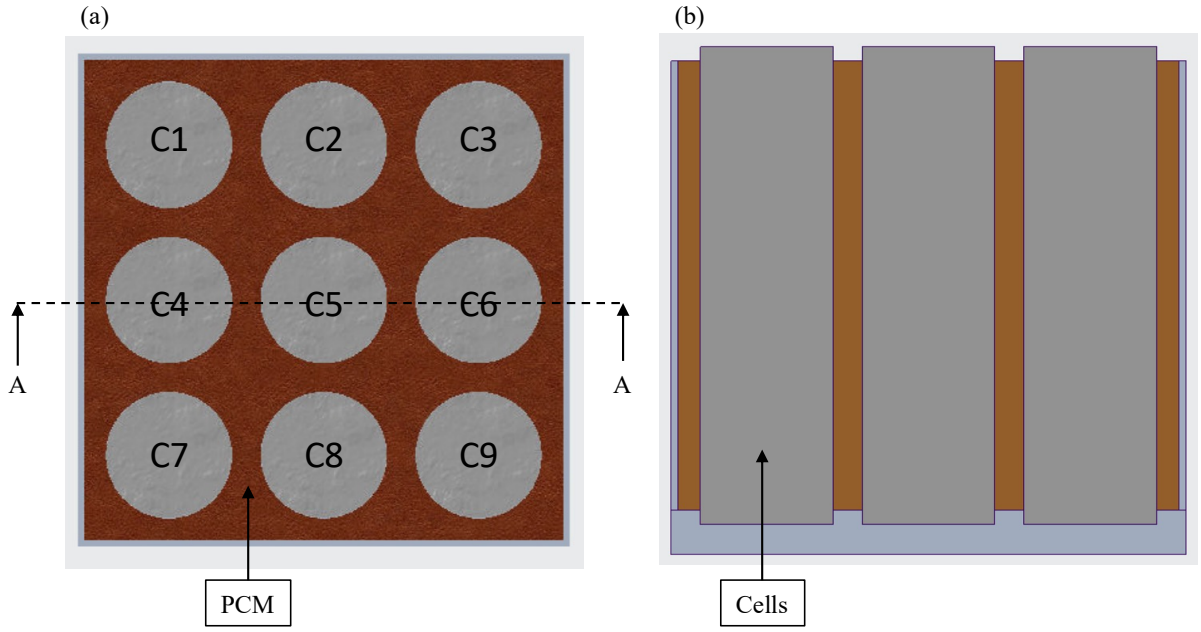

Figure 3.3: (a) Top view and (b) A-A section view of BM1 computer aided-design (CAD) model.

For configuration BM2, BM1 has been modified to a hybrid BTMS by introducing liquid channels in between the cell columns and rows, as shown in Figure 3.4. The liquid used in these channels is water, and the physical properties of the water are provided in Table 3.2. In BM2, the liquid within these channels is stationary.

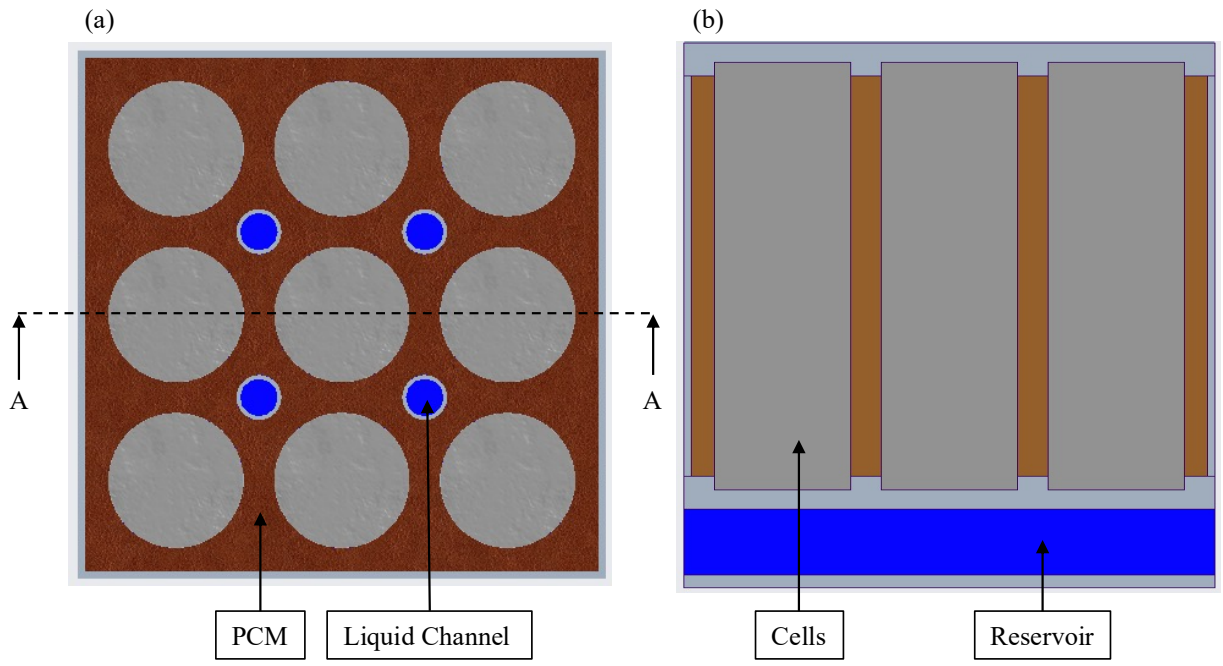

Figure 3.4: (a) Top view and (b) A-A section view of BM2 CAD model.

For configuration BM3, BM2 has been modified, and an air duct is added at the top of the battery pack as shown in Figure 3.5. The properties of air are provided in Table 3.2. BM3 is the true representation of Strategy 1 described in Section 3.1.1.

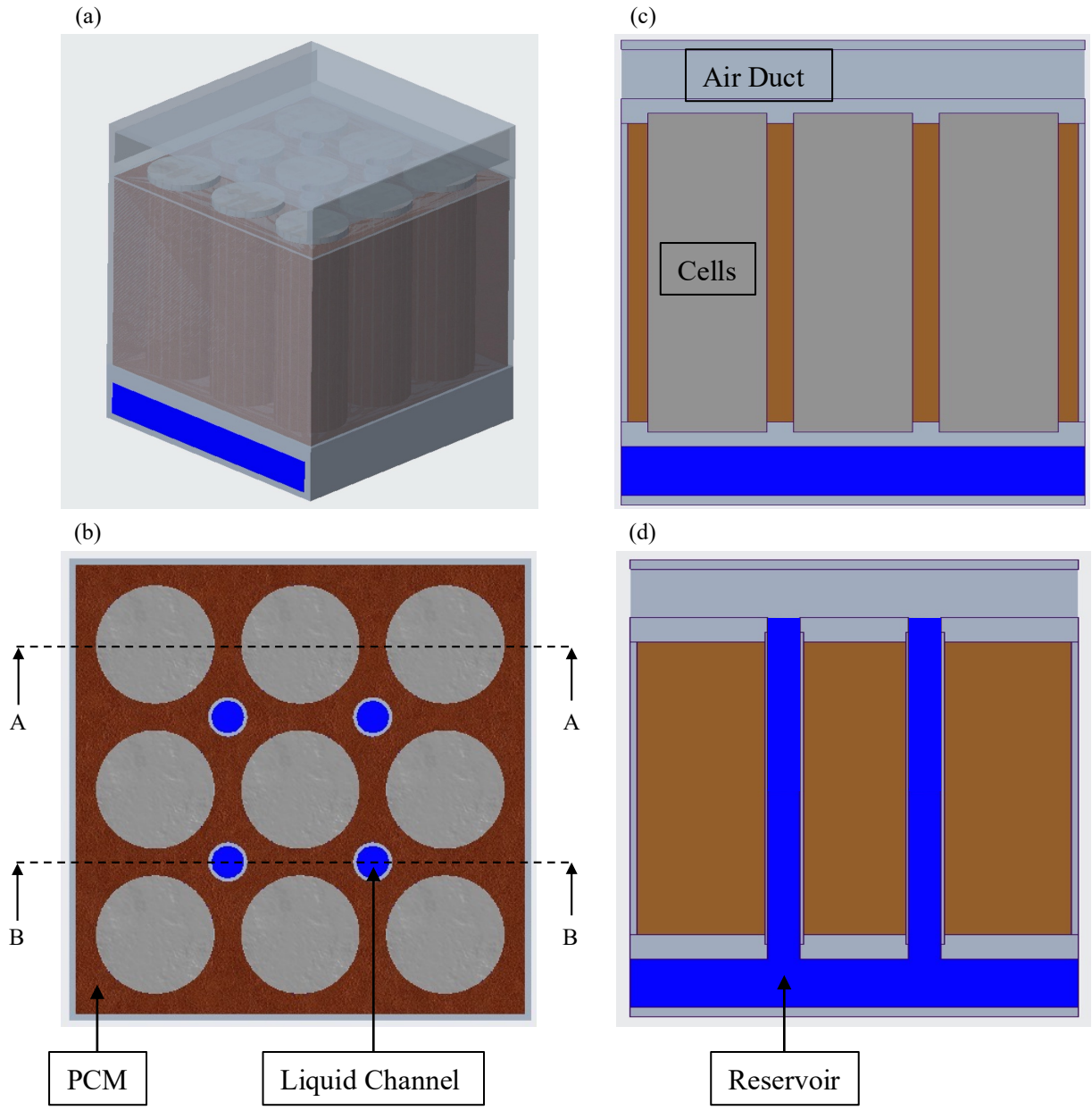

Figure 3.5: (a) Isometric view, (b) top cross-section view, (c) A-A section view, and (d) B-B section view of BM3 CAD model.

3.2.2. Comparison Study of Configurations of Strategy 1

In order to further evaluate the proposed Strategy 1, three distinct battery module configurations of configuration BM3 are developed. In all three configurations, the PCM surrounds the cells and is in direct contact with the surface of the cells. An outer case of the battery pack ensures that the

PCM stays within the bounds of the battery pack. An air duct is placed at the top of the cells, and a liquid reservoir is placed at the bottom of the cells. The first configuration (BM3-C1) is shown in Figure 3.5 and is described in Section 3.2.1 The liquid channels in this configuration are placed in between the PCM material and run vertically from the liquid reservoir to the air duct.

The second configuration (BM3-C2) is shown in Figure 3.6. In this configuration, the location of the liquid channel is modified. A portion of the liquid is connected directly to the cells. The rest of the portions are connected to the PCM. This configuration allows the liquid to extract heat from the cell and the PCM simultaneously.

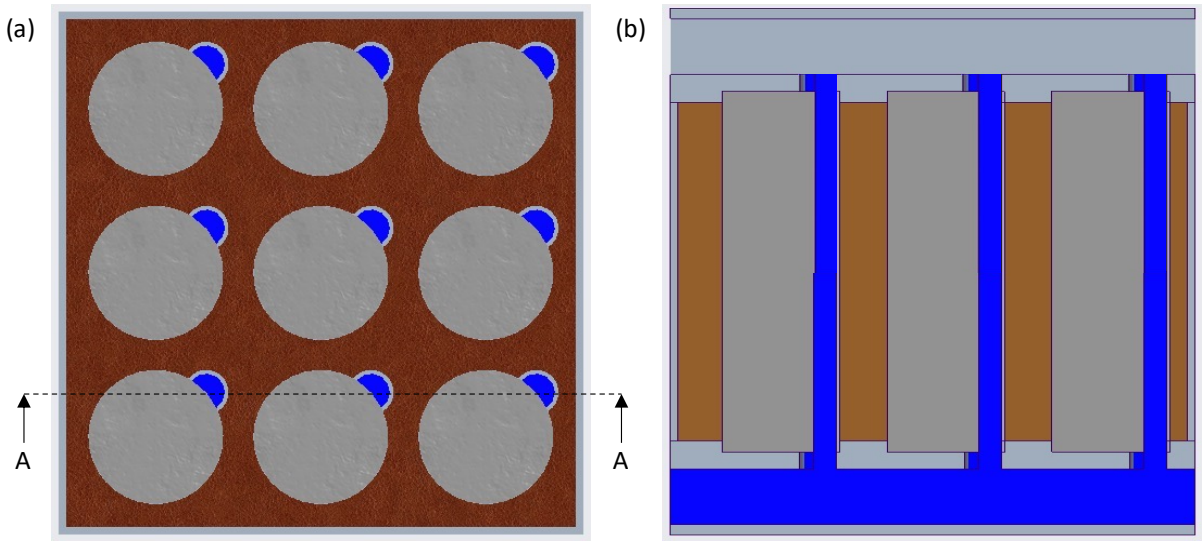

Figure 3.6: CAD model for BM3-C2: (a) top view, (b) A-A section view.

The third configuration (BM3-C3) is shown in Figure 3.7. The liquid channels are simplified by connecting them from one cell to the subsequent cell. This is a simpler form of BM3-C2 and should allow enhanced heat transfer from the cell to the liquid and the PCM as well. For comparison, the volume of liquid used in all three instances was kept the same by modifying the dimensions of the liquid channels.

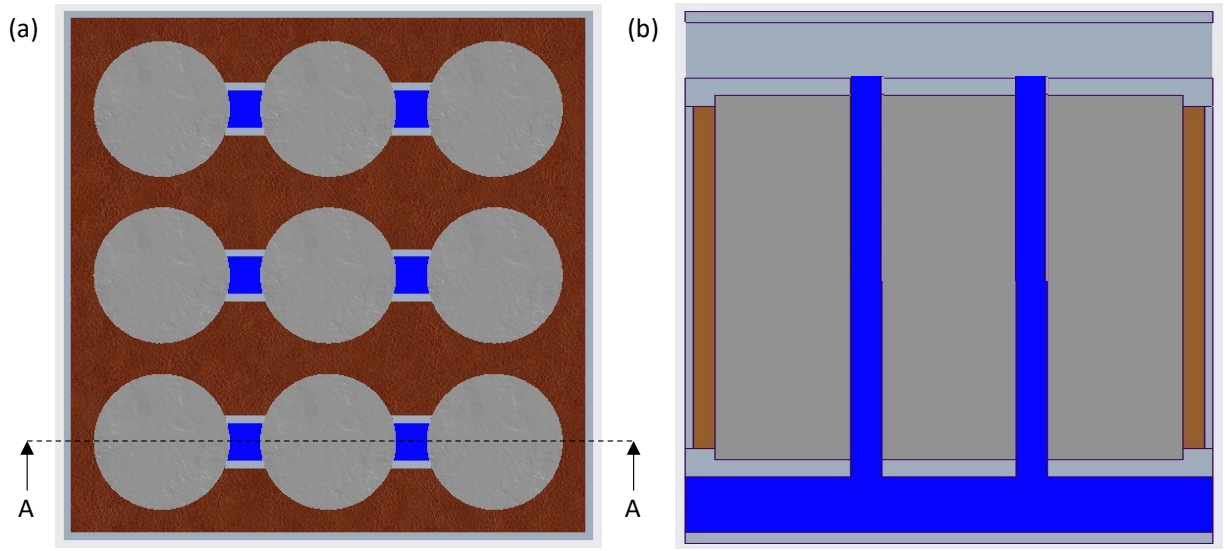

Figure 3.7: CAD model for BM3-C3: (a) top view, (b) A-A section view.

3.2.3. Comparison Study of Primary Cooling Mediums in Strategy 1

This study is conducted to compare the impact on the thermal performance of the battery module by considering different primary cooling mediums. Three different configurations were developed for this study to compare the PCM and liquid cooling mediums. The primary cooling medium in BM3-C1 is the PCM as described previously and the properties of the PCM are provided in Table 3.2. Since the phase change temperature of PCM used in BM3-C1 is low and at higher ambient temperatures it will easily melt therefore, for BM3-C4, a different PCM was used with a higher phase change temperature. The properties of this PCM are provided in Table 3.3. In the final configuration (BM3-C5), the primary cooling medium used is Poly-Alpha-Olefin (PAO), which is an electrically insulating fluid. Since the primary cooling medium is in direct contact with the surface of the cells, therefore, an electrically insulating fluid is required. Additionally, PAO has a low density and high thermal conductivity and specific heat compared to other electrically insulating fluids available in the market (Roe et al., 2022). It is to be noted that in all configurations, the secondary cooling mediums were water and air.

Table 3.3: Material properties of Paraffin (BM3-C4) and PAO (BM3-C5) (Roe et al., 2022).

Material Properties	Paraffin (BM3-C4)	Poly-Alpha-Olefin (BM3-C5)
Density (kg/m^3)	880	800
Specific Heat (J/kg.K)	2,150	2,241
Thermal Conductivity (W/m.K)	0.21	0.14
Viscosity (kg/m.s)	0.00312	0.0051
Latent heat (J/kg)	245,000	-
Solidus Temperature (K)	315.15	204
Liquidus Temperature (K)	317.15	204

3.2.4. Development of Strategy 2 and Comparison with Strategy 1

Strategy 2 (BM4-C1) was developed by modifying Strategy 1 (BM3-C1) and is shown in Figure 3.8 (a) and (b). The circular liquid channel in between the PCM was changed to the rectangular cold plate, which is completely filled with fluid and protrudes in the air duct. This cold plate is sealed and closed from all sides so that there is no leakage of fluid. Two of these cold plates are placed in between each cell row in the longitudinal direction such that the larger surface area of the protrusion in the air duct is in line with airflow. The working principle behind this strategy is similar to Strategy 1, with a few key differences. The initial stage is the same as the PCM will extract heat from the surface of the cells. In the intermediary stage, the fluid within the cold plates will extract heat from the PCM. In the final stage, rather than removing fluid vapors from the system, the air will pass over the protruded cold plate and will be used to cool the fluid within it. For comparison purposes, the volume of fluid within the liquid channels in Strategy 1 (BM3-C1) and cold plates in Strategy 2 (BM4-C1) was kept the same. Since the fluid in this strategy is sealed, therefore, no pumping power is required to top up the fluid, which eliminates the requirement for a fluid pump and reservoir.

BM4-C1 was further modified to develop an alternate configuration of Strategy 2 (BM4-C2) and is shown in Figure 3.8 (c) and (d). The geometry of the cold plate was changed so that it could be placed in between each cell column as well. As shown in Figure 3.8 (d), the cold plates are all connected to each other, and the fluid within this is considered a single body of fluid. The protrusion of the cold plate within the air duct is, however, the same as Strategy 2, as shown in Figure 3.8 (c). Due to a single fluid body, the same protrusion geometry will allow the fluid in between the columns to cool as well. The working principle for BM4-C2 is identical to BM4-C1. Since BM4-C2 is an improvement of BM4-C1 therefore, the volume of fluid was increased at the expense of PCM volume.

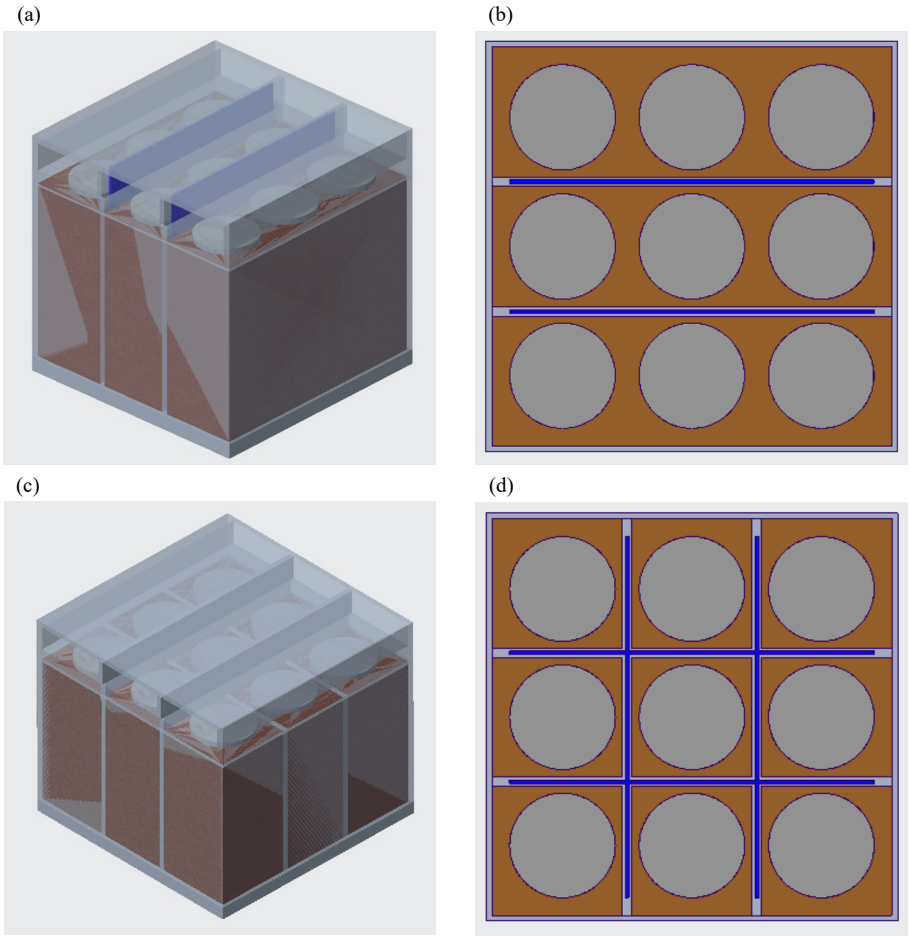

Figure 3.8: (a) Isometric view and (b) top cross-section view of BM4-C1; (c) isometric view and (d) top cross-section view of BM4-C2.

3.2.5. Addition of Property Enhancing Materials to Paraffin based PCM in Strategy 2

Pure paraffin usually has a low thermal conductivity, as can be seen in Table 3.2 and Table 3.3. In order to improve the cooling of the Li-ion batteries, researchers have worked on increasing the various properties of paraffin, including thermal conductivity, using different types of property enhancing materials (PEM). These PEM include expanded vermiculite, graphene oxide, carbon foam, copper foam, porous graphite foam, and expanded graphite. A review study by Mishra et al. (2022) has reviewed paraffin based PCM equipped with various PEM for the past 17 years that were developed by researchers. For this study, different types of CPCM were selected that could be applied to the developed strategies based on their thermal conductivity and solid to liquid phase change temperature. The thermal conductivity of the selected CPCM ranges from low to high, as provided in Table 3.4.

Table 3.4: Thermal properties of CPCM with a paraffin base and different types of PEM (Mishra et al., 2022).

PEM (Composition%)	Thermal Conductivity (W/m.K)	Latent heat (J/kg)	Phase Change Temperature (°C)
CPCM-1 - Expanded Vermiculite (33)	0.545	135,500	48.00
CPCM-2 - Graphene Oxide (51.7)	0.985	63,760	53.57
CPCM-3 - Carbon Foam (-)	1.198	164,980	52.10
CPCM-4 - Copper Foam (2.7)	3.11	170,400	42.24
CPCM-5 - Porous Graphite Foam (20)	4.98	142,000	51.40
CPCM-6 - Expanded Graphite (25)	14.7	168,100	43.00

It can be seen from Table 3.4 that by adding different types of PEM to paraffin the thermal conductivity, latent heat, and phase change temperature changes simultaneously. Therefore, actual CPCM was considered for this study rather than artificially changing a thermal property and

examining the effects of it. Additionally, it can be seen that by adding PEM to paraffin the latent heat reduces as the latent heat of pure paraffin is 245 kJ/kg (Table 3.2) whereas, the highest latent heat is of CPCM-4 with 170.4 kJ/kg.

3.2.6. Increasing the Thermal Conductivity of Water through Nanoparticles

The fluid within the cold plate is required to remove heat from the PCM. Hence, thermal conductivity is one of the defining factors for the amount of heat removal. A high thermal conductivity will result in increased heat removal from the PCM. To study this, two configurations are devised. BM4-C3 is developed by modifying BM4-C2. In this, the PCM material has been changed to CPCM-4 (paraffin base combined with copper foam) and water is still used as the fluid. For the second configuration BM4-C3 is modified to BM4-C4 by changing the fluid to water combined with nanoparticles. In order to select the nanoparticle recent studies in open literature were reviewed (Corasaniti et al., 2021; Ghasemi et al., 2021; Jabbari et al., 2021; Pourrajab et al., 2021; Bioucas et al., 2022; Amburi et al., 2023) and it was found that 0.04% of silver and 0.16% multi-walled carbon nano-tubes combined with water base (H_2O-AG-MWCNT) provided the highest thermal conductivity of 0.92 W/m.K at 42.24 °C (Pourrajab et al., 2021). 42.24 °C was selected as it is the phase change temperature of CPCM with copper foam.

3.2.7. Parametric Study on the Volume of Paraffin based CPCM Combined with Copper Foam

This parametric study is conducted with the objective of reducing the amount of the CPCM-4 in the battery module as this will assist in reducing the volume of the CPCM-4 resulting in a feasible size of the battery module. For this study, BM4-C3 was used to develop six test configurations. The parameter under investigation is the volume of CPCM-4. The details are provided in Table 3.5 and Figure 3.9. The first five configurations were developed by reducing the amount of CPCM-

4 that is in between the cells and the module housing as shown in Figure 3.9 (a) to (e). For the sixth configuration the amount of CPCM-4 between the cell and the cold plate was reduced as shown in Figure 3.9 (f).

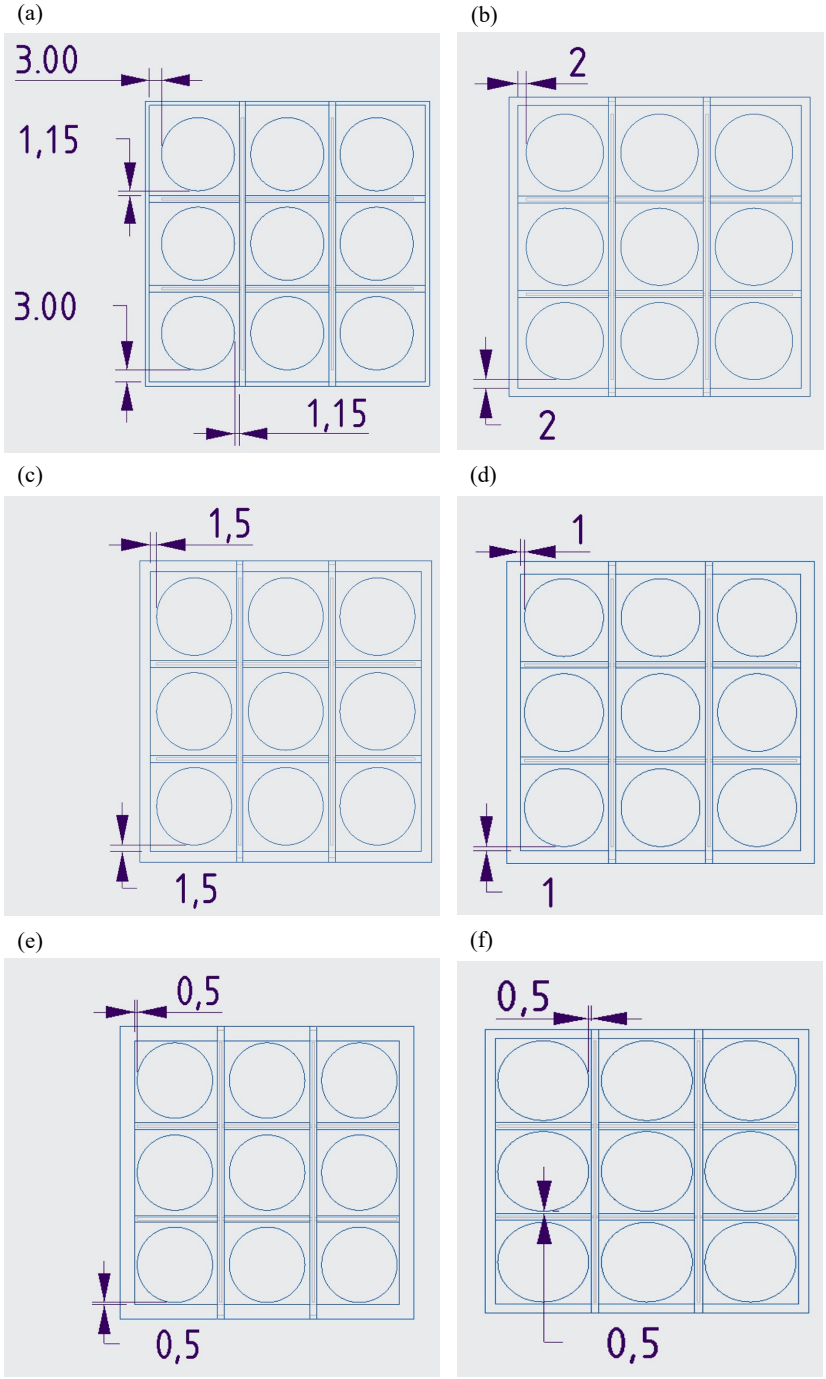

Figure 3.9: Schematic of Test Configuration No. (a) 1, (b) 2, (c) 3, (d) 4, (e) 5, and (f) 6 (Note: All dimensions are in mm).

Table 3.5: Total volume of CPCM-4 in developed test configurations.

Test Configuration No.	CPCM-4 Volume (mm^3)	Volume Difference (%)
1	116,438.00	-
2	100,871.00	13.4
3	93,270.20	7.5
4	85,791.60	8.0
5	78,435.00	8.6
6	58,485.51	25.4

3.2.8. Parametric Study on the Inlet Size of Battery Module

The objective of this parametric study is to find the feasible inlet size of the air duct in the battery module. The inlet width is dependent on the volume of the CPCM-4. Based on the dimensions of test configuration 6 the inlet width is 60 mm, and the height is 10 mm. Since the width is fixed, therefore, to reduce the size of the air duct the parameter under investigation in this study is the height of the air duct. It was varied as shown in Table 3.6. With the reduction in the cross-section area of the inlet, the velocity increased in order to keep the same Reynolds number of 1950.

Table 3.6: Variation of the air duct inlet height in developed test configurations.

Test Configuration No.	Height of Air Duct Inlet (mm)	Inlet Velocity (m/s)
6	10	2.17
7	8	2.53
8	6	3.12
9	4	4.31
10	2	7.87

3.2.9. Parametric Study on the Airflow Reynolds Number

In addition to determining the feasible size of the battery module, there is a need to determine the feasible Reynolds number which is obtained through this parametric study. The general intuition is that as the airflow Reynolds number increases, the cooling and temperature uniformity will increase. However, a compromise is needed as one of the objectives of this research is to reduce the amount of fan power which is directly dependent on the airflow Reynolds number. Therefore, this parametric study is conducted, and the parameter under investigation is the Reynolds number for this study. The details of the developed test configuration are provided in Table 3.7. The initial test configuration 8 was selected from the previous parametric study of inlet size. This test configuration was then modified with varying Reynolds number from 0 to 31,200.

Table 3.7: Variation of Reynolds number in developed test configurations.

Test Configuration No.	Reynolds Number	Inlet Velocity (m/s)
8	1,950	3.12
11	0	0
12	243.75	0.39
13	487.5	0.78
14	975	1.56
15	3,900	6.25
16	7,800	12.5
17	15,600	24.99
18	31,200	49.97

3.2.10. Study on Adding Fins to Improve the Heat Transfer

In this study an attempt is made to further improve cooling by increasing the heat transfer from the fluid in the cold plate to the airflow. This is done through the addition of fins to the cold plate within the air duct. Configuration BM4-C3 with 6 mm of inlet air duct height was modified to BM5-C1 by adding one fin of thickness 0.5 mm parallel to the airflow in the middle of the air duct as shown in Figure 3.10 (a). For comparison, BM5-C1 was modified to BM5-C2 by adding two fins parallel to the airflow as shown in Figure 3.10 (b). In order to keep the same Reynolds number of 1,950 the velocity increased at the inlet and the details for the three configurations are provided in Table 3.8.

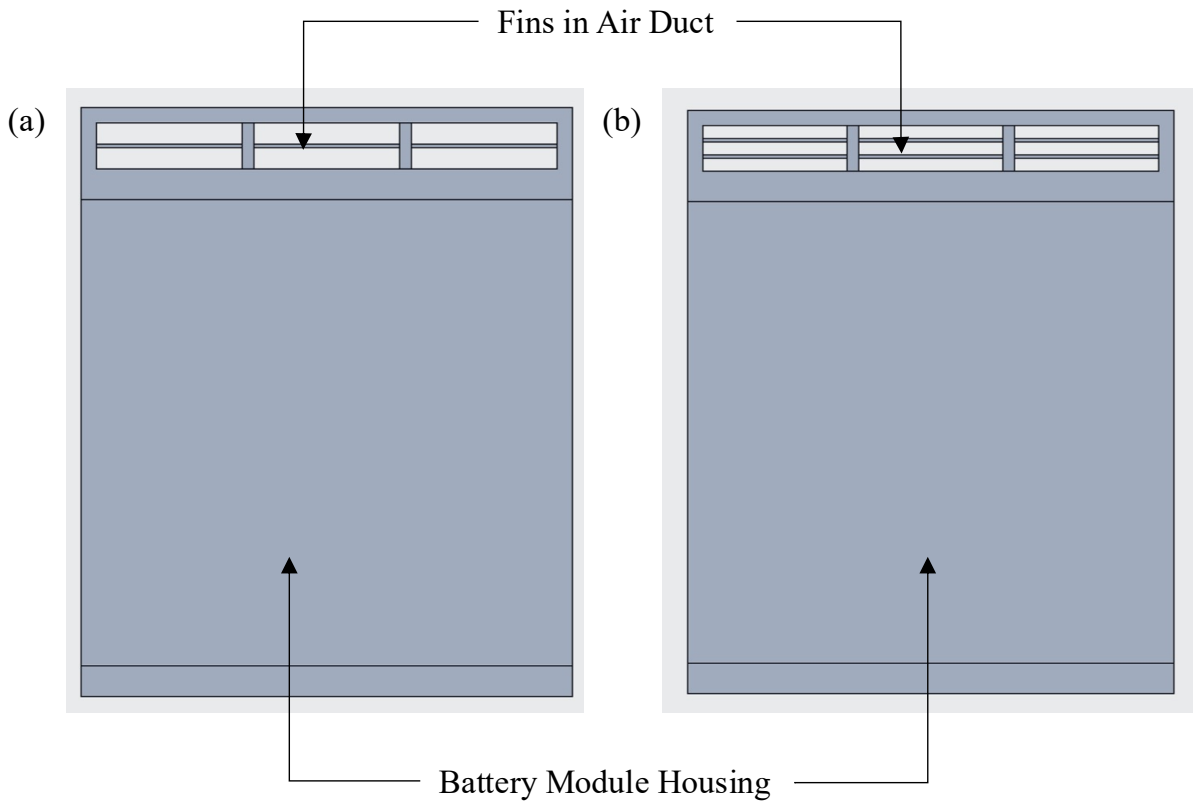

Figure 3.10: Schematic of front view of (a) BM5-C1 and (b) BM5-C2.

Table 3.8: Number of fins and corresponding inlet velocity for the developed configurations.

Battery Module Configuration	Number of Fins	Inlet Velocity (m/s)
BM4-C3	0	3.12
BM5-C1	1	5.93
BM5-C2	2	9.28

3.2.11. Scalability Study of Battery Module

For this study BM4-C3 module was used to scale the battery module to the entire battery pack. For reference a Tesla 75 kWh battery pack was used (*Tesla Model S/X Pack - 75kWh / 214Ah / 350V*, n.d.). The physical dimensions of the Tesla battery pack include a length of ~1660 mm, width of ~964 mm, and height of 174 mm. The total number of cylindrical cells is 5,880. In order to accommodate the BM4-C3 within the same dimensions 25 modules were connected in series (in terms of airflow) which amounts to 1600 mm of length as shown in Figure 3.11 (a). Each series setup of modules (BMA) was connected 15 times in parallel (in terms of airflow) which amounts to a width of 960 mm as shown in Figure 3.11 (b).

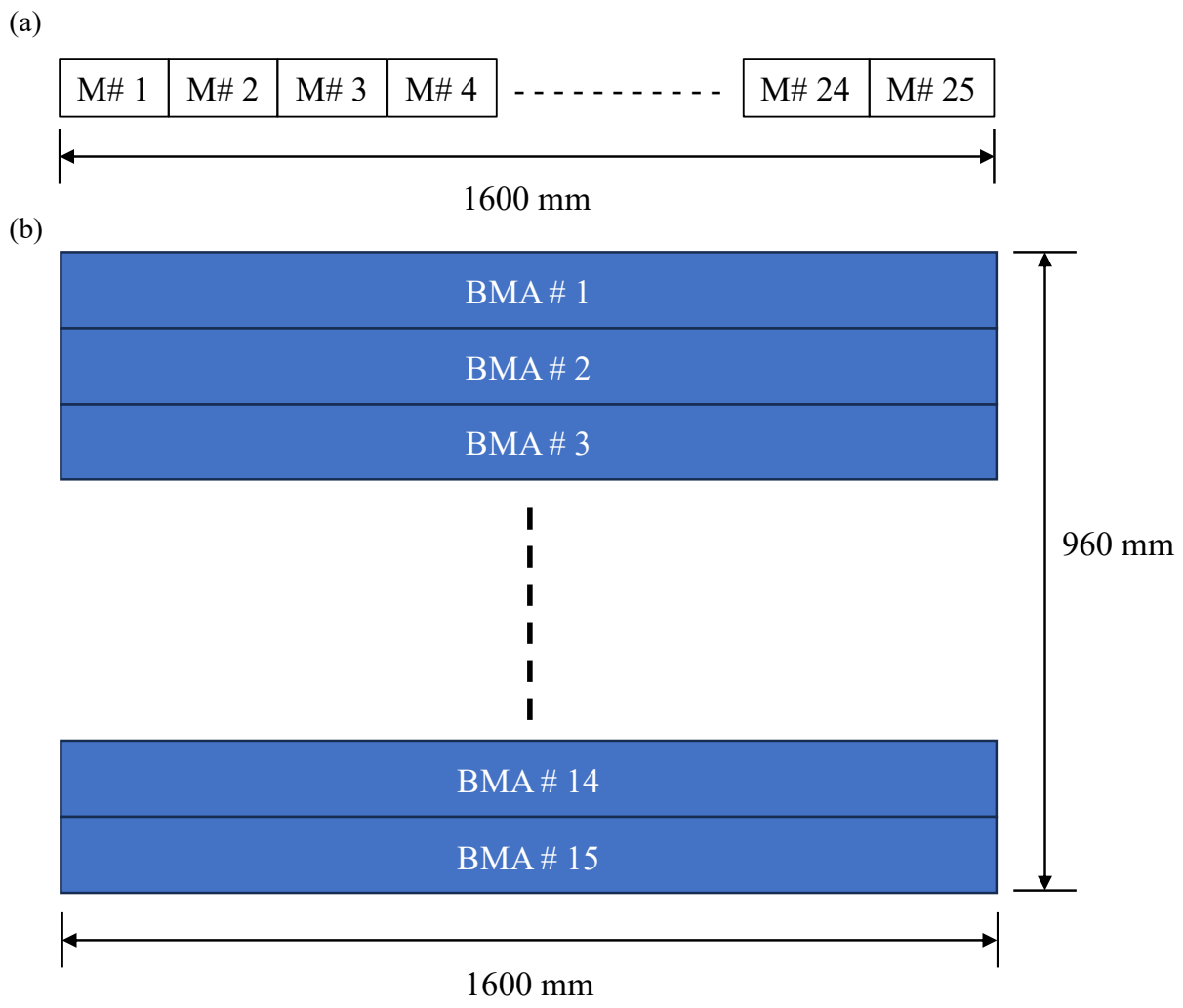

Figure 3.11: (a) Schematic of battery module assembly (BMA) in series; (b) schematic of BMA connections in parallel.

Finally, two arrays of series and parallel modules were placed vertically to amount for a height of 154 mm. Therefore, the total number of BM4-C3 modules in the battery pack is 750 which contains a total of 6,750 cylindrical cells. Since the modules in width and the height directions are in parallel airflow therefore, 1 series configuration of 25 modules, as shown in Figure 3.11 (a), was used for the evaluation of the scalability of the module. As shown in Figure 3.9 (f) the spacing in between the cells and cold plate is tight with 0.5 mm so it was not feasible to conduct the simulation for all 25 modules at once due to high computational requirements. Therefore, results were obtained for

2, 3, and 4 modules in series and the pressure drop, and maximum temperature of airflow and the cells was extrapolated. Moreover, a simulation was conducted for airflow only across the 25 battery modules to verify the pressure drop through the air duct. The schematic for the airflow domain is shown in Figure 3.12. The domain is based on a single channel of airflow within the air duct.

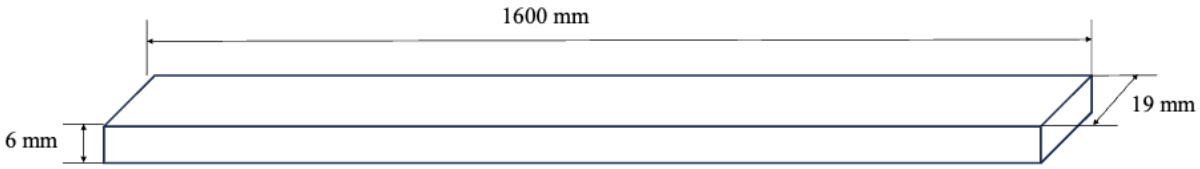

Figure 3.12: Airflow domain for a single series air duct channel of battery pack.

3.3. Experimental Setup and Procedures

In this study, two separate experiments were performed. In the first experiment, a single Samsung INR18650-25R cell was used to measure the heat flux at the surface of the cell. The heat flux was obtained to be used as a boundary condition in the numerical modeling. In the second stage, the battery module was manufactured, as shown in Figure 3.5, with nine Samsung INR18650-25R cells and the temperature measurements were obtained. The detailed experimental setup and procedure are described in the following sub-sections.

3.3.1. Experiment 1 - Heat Flux Measurement

Experiment 1 was conducted to obtain the heat flux measurements at the surface of the cell. This heat flux measurement will then be used as the boundary condition in the numerical modeling. The setup of this experiment is shown in Figure 3.13 (a), and the schematics are shown in Figure 3.13 (b). The Samsung INR18650-25R Li-ion cell with Aluminum tabs attached to positive and negative terminals was used to measure the heat flux. The properties of the cell are provided in Table 3.1. The electrical insulation was removed from the surface of the cell to get accurate measurements, as the non-insulated cells are used in the battery module. To charge the lithium-ion batteries, a Turnigy Reaktor Quadkore charger is used. This is capable of charging 4 cell groups simultaneously up to 300W and 20A. This has a high power, high current, and high-performance power conversion circuit. A direct current (DC) power supply (Jesverty SPS-3010N) was used to power the Turnigy Reaktor. To discharge the batteries a multi-functional load discharger (TDI RBL488) is used. It has high power draining load capacities of up to 800W and 120A. It incorporates variable speed forced air cooling to ensure a quiet environment. An Omega HFS-5 sensor was used for the heat flux measurements. To measure the readings from the HFS-5 sensor,

a National Instrument (NI) data acquisition device (DAQ) NI-9211 combined with NI cDAQ-9174 chassis was used. Finally, LabView software was used to capture the reading from the DAQ module.

As shown in Figure 3.13 (a), alligator clips were connected to the positive and negative tabs of the Li-ion cell. The cell was charged in two stages. The first stage of the charging process consisted of a constant current (CC) charge at 1 A charging current. During this stage, the voltage of the cell increased gradually. Once the voltage reached 4.2 V then the second stage of the charging process started. In the second stage, the cell was charged at constant voltage (CV). The voltage was maintained at 4.2 V, and the charging current was reduced from 1 A to 0 A. Once the cell was completely charged, then the cell was kept at room temperature of 25 °C for 1 hour. Then the discharge process started, and the cell was discharged at 2.5 A CC discharging rate (which corresponds to 1 C discharge rate) until the voltage dropped to the cut-off voltage of 2.5 V. During the discharge process, the data was recorded using the LabView software. For the charging and discharging the IEC 62133 and IEC 61960 were employed, respectively.

(a)

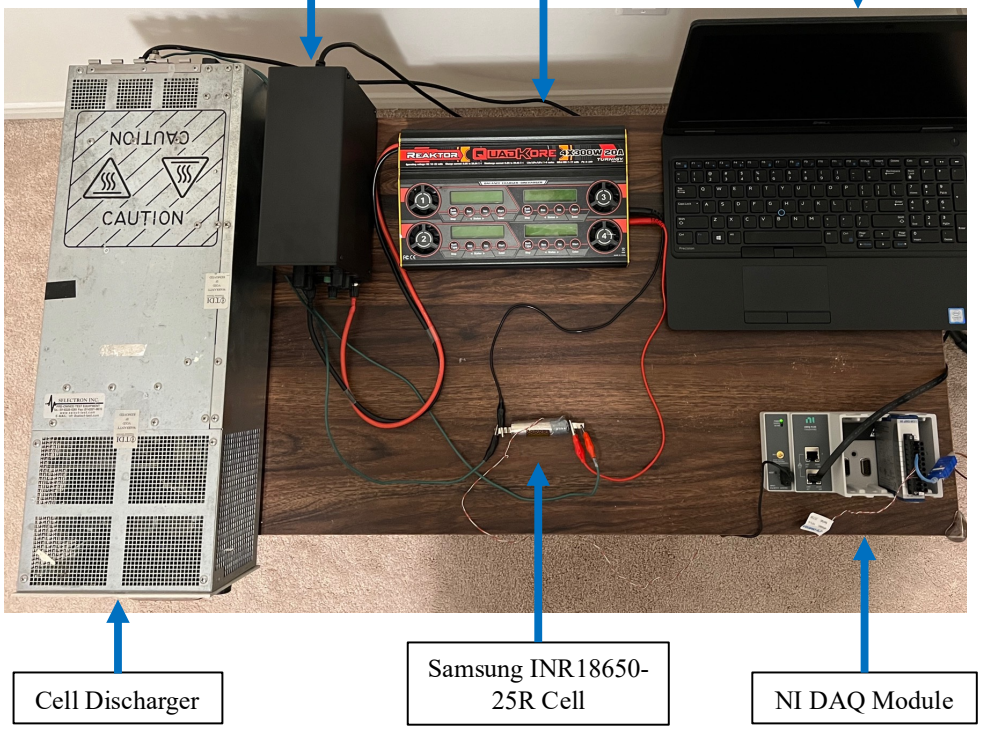

(b)

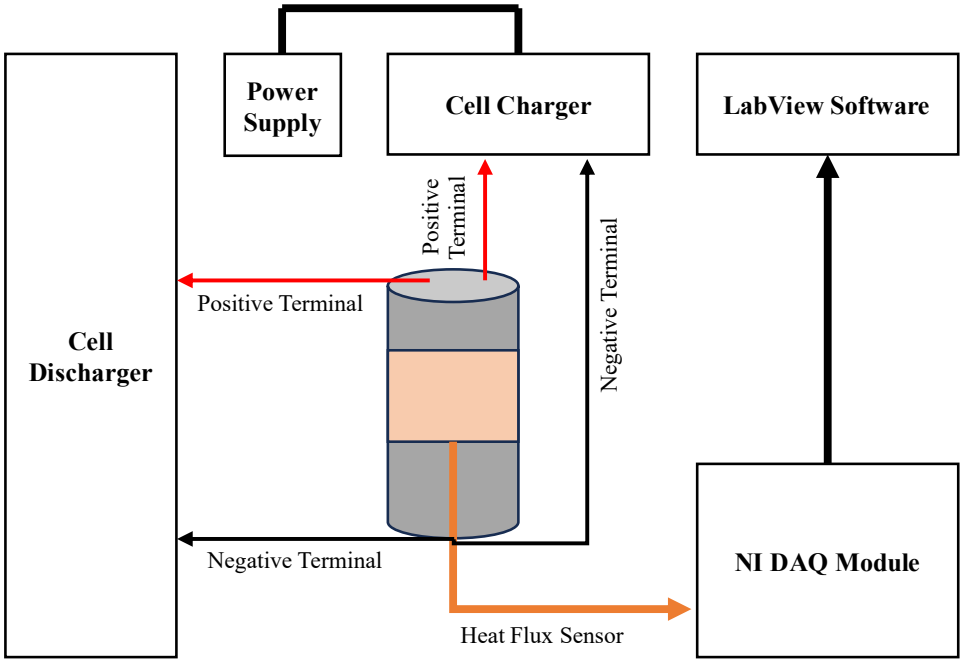

Figure 3.13: Experiment 1 - (a) top view and (b) schematic of the experimental setup.

3.3.2. Experiment 2 – Temperature Measurement

Experiment 2 was conducted to measure the temperature of all the cells within the battery module. The setup of this experiment is shown in Figure 3.14 (a), and the schematics are shown in Figure 3.14 (b). The details of the cell charger and discharger, NI DAQ module, power supply and LabView software are already provided in the previous section. For this experiment, a battery module was manufactured identical to the CAD design shown in Figure 3.5. The outer casing of the battery module was made from wood. Nine cylindrical Samsung INR18650-25R cells were placed within the module and connected in series. Aluminum liquid channels were filled with water and placed in between the PCM material. An axial fan (GDSTIME AXIAL Fan 12038) was used to force air through the air duct in the battery module, and the velocity of the airflow was measured using the Proster Anemometer. Finally, the temperature of the cells was measured using nine T-type thermocouples attached to each cell.

To manufacture the battery module, the panels of the wooden housing were laser cut, including the holes in the bottom and the top plates to hold the cells and liquid channels in place. The wooden panels were then glued together. All nine cells were then placed inside the housing. Four aluminum liquid channels were placed inside the housing and filled with water. Thermocouples were then attached to each cell using adhesive tapes. Then the PCM blocks (paraffin wax) were melted using a wax melt warmer, and the melted PCM was then poured into the battery pack. The melted PCM was poured to ensure that the complete surface area of the cell was in direct contact with the PCM once it solidified. The wires were then connected to the tabs of the cells to connect them all in series. Finally, the air duct was placed on top of the battery module.

(a)

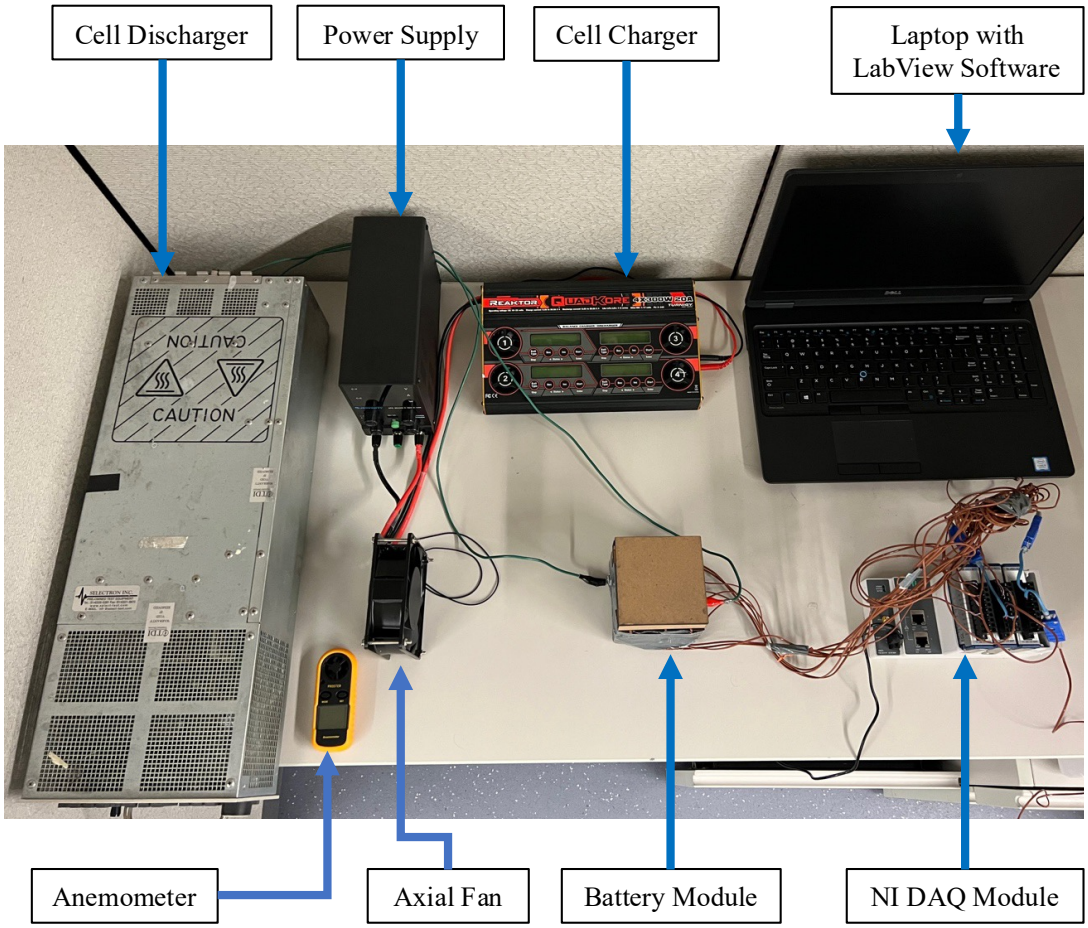

(b)

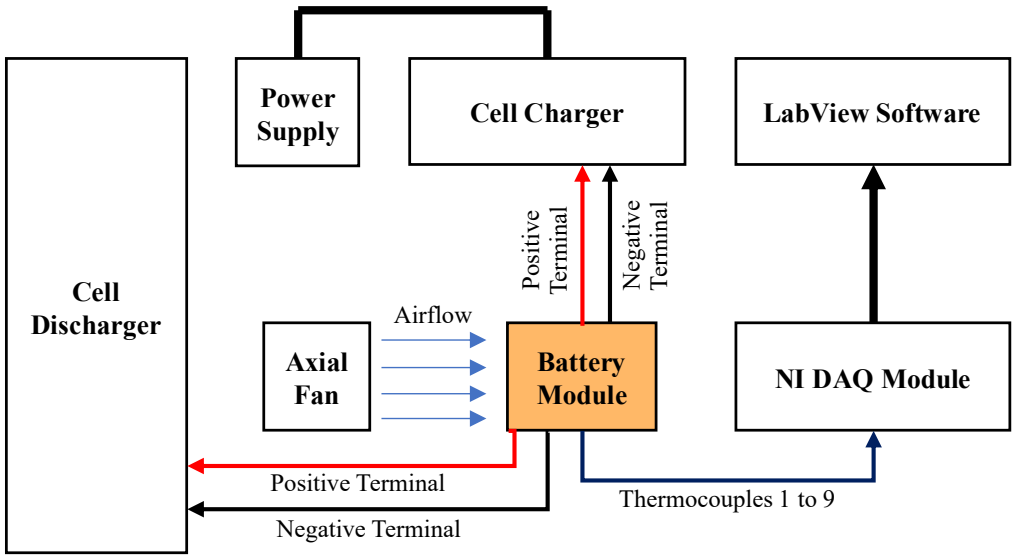

Figure 3.14: Experiment 2 - (a) top view and (b) schematic of the experimental setup.

The procedure for Experiment 2 consisted of charging all the cells in the battery module using the Turnigy Reaktor charger. The cells were charged with CC-CV process as described in Section 3.1. Since all the cells are connected in series, therefore, the total voltage of the battery module at the end of the charging cycle was 37.8 V (the voltage of each cell was 4.2 V). The battery module was then kept at a room temperature of 25 °C. The fan was then turned on, and the velocity was measured at the inlet of the battery module using a Proster anemometer. Once the readings from the thermocouples were measured to be 25 °C, then the discharge process was started. The cell was discharged at CC discharging rate, and the temperatures from the thermocouples were recorded using the LabView software. The discharge process was terminated when the voltage of the battery module reached 22.5 V. Note that for the charging and discharging the IEC 62133 and IEC 61960 were employed, respectively. The properties of the different materials used for this experiment are shown in Table 3.2.

Table 3.9: Physical properties of materials used for Experiment 2.

Material Properties	**Aluminum**	**Wood**	**Air**	**Water**	**Paraffin**
Density (kg/m^3)	2,719	700	1.225	998.2	880
Specific Heat (J/kg.K)	871	2,310	1,006	4,182	2,150
Thermal Conductivity (W/m.K)	202.4	0.173	0.0242	0.6	0.21
Viscosity (kg/m.s)	-	-	0.000018	0.001003	0.00312
Pure Solvent Melting Heat (J/kg)	-	-	-	334,000	245,000
Solidus Temperature (K)	-	-	58	273.15	315.15
Liquidus Temperature (K)	-	-	61	273.15	317.15

3.4. Uncertainty/Error Analysis

An uncertainty/error analysis was performed for the experimental measurements and is described in this section. The method described by Moffat (Moffat, 1988) is used to calculate the uncertainties. Based on this method, the result, R, of the experiment is calculated as:

$$R = R(X_1, X_2, X_3, \dots, X_N) \tag{3.1}$$

Each separate measurement is denoted by $X_i \pm \delta X_i$ where δX_i is the uncertainty. The effect of the δX_i term on each measurement is analyzed using:

$$\delta R = \frac{\delta R}{\delta X_i}\delta X_i \tag{3.2}$$

Therefore, the overall uncertainty of the results is:

$$\delta R = \left\{\sum_{i=1}^{N}\left(\frac{\delta R}{\delta X_i}\delta X_i\right)^2\right\}^{1/2} \tag{3.3}$$

If R is described by an equation in the form of

$$R = X_1^a X_2^b X_3^c \dots\dots X_N^m \tag{3.4}$$

then the overall uncertainty of the result can be determined using the set individual measurement uncertainties directly using the following equation:

$$\frac{\delta R}{R} = \left\{\left(a\frac{\delta X_1}{X_1}\right)^2 + \left(b\frac{\delta X_2}{X_1}\right)^2 + \cdots + \left(m\frac{\delta X_N}{X_1}\right)^2\right\}^{1/2} \tag{3.5}$$

Since random errors also known as “precision” errors occur during the course of the experiment, therefore, a relative standard deviation (RSD) term is used to account for these precision errors. This is calculated the standard deviation, s, and the following equation:

$$RSD = \frac{s}{\bar{x}}\ 100\% \tag{3.6}$$

Finally, the bias error and precision error, are combined using the root mean square method.

The uncertainties in the heat flux and temperature measurements are calculated using the method described above. The details are tabulated in Table 3.10. The average percentage uncertainty in the heat flux and temperature measurements is ± 3.59%.

Table 3.10: Calculated values of relative bias and precision errors and total uncertainty.

Parameters	**Reference Value**	**Absolute Bias Error**	**Relative Bias Error (%)**	**Relative Precision Error (%)**	**Total Uncertainty (%)**
Min. Temp.	25.00 ºC	1.00 ºC	4.00	2.22	4.57
Max. Temp.	47.00 ºC	1.00 ºC	2.13	1.49	2.60
Min. Heat Flux	18.99 W/m^2	1.27 W/m^2	6.69	1.90	6.95
Max. Heat Flux	584.16 W/m^2	1.27 W/m^2	0.22	0.05	0.22

3.5. Numerical Modeling Methodology

3.5.1. Governing Equations

The numerical model was developed using ANSYS Fluent by replicating the battery module and experimental conditions of Experiment 1 as described in Section 3.1. Three different models were coupled to develop the numerical model. These models include the flow model, energy, and solidification/melting model. The turbulence model was only used and coupled with the three models when the airflow velocity was in turbulent flow range. It should be noted that the governing equations were not changed for CPCM and nano-materials. Rather, their effective properties (such as the thermal conductivity and latent heat) were obtained from the open literature and were used for the numerical modeling.

3.5.1.1. Flow and Energy Modeling

The governing equations for the flow and energy models are provided below (ANSYS, 2020).

Continuity Equation

$$\frac{\partial \rho}{\partial t} + \nabla \cdot (\rho \vec{v}) = S_m \tag{3.7}$$

Where;

S_m represents any user defined sources.

Momentum Conservation Equation

$$\frac{\partial}{\partial t}(\rho \vec{v}) + \nabla \cdot (\rho \vec{v} \vec{v}) = -\nabla P + \nabla \cdot \bar{\bar{\tau}} + \rho \vec{g} + \vec{F} \tag{3.8}$$

Where;

$\vec{F}$ consists of external body forces and user defined sources.

$\bar{\bar{\tau}}$ is the stress tensor and is represented by Equation (17).

$$\bar{\bar{\tau}} = \mu\left[(\nabla\vec{v} + \nabla\vec{v}^{T}) - \frac{2}{3}\nabla\cdot\vec{v}U\right] \quad (3.9)$$

Where;

U is the unit tensors which represent the molecular viscosity.

Energy Equation

$$\frac{\partial}{\partial t}(\rho E) + \nabla\cdot\left(\vec{v}(\rho E + P)\right) = \nabla\cdot\left(k_T\nabla T - \sum_j h_j\vec{J}_j + \left(\bar{\bar{\tau}}_{eff}\cdot\vec{v}\right)\right) + S_h \quad (3.10)$$

Where;

k_T is the effective thermal conductivity,

$h_{j,q}$ is the enthalpy of species in the specified phase.

S_h represents the volumetric heat sources.

3.5.1.2. PCM Solidification/Melting Modeling

The solidification/melting model was only applied to the PCM region. The enthalpy-porosity technique is used to model the phase change process. In this technique, the interfaces where the solid melts are not explicitly tracked. Instead, a liquid fraction (β) quantity is introduced, which provides the fraction of each cell volume that is in liquid form. This liquid fraction is based on the enthalpy balance (ANSYS, 2020). The enthalpy of the PCM is based on the latent heat and sensible enthalpy, as shown below (ANSYS, 2020).

$$H = h + \Delta H \quad (3.11)$$

where;

$$h = h_{ref} + \int_{T_{ref}}^{T} c_p dT \quad (3.12)$$

The liquid fraction is 0 if the temperature (T) is less than the solidification temperature ($T_{solidus}$) of the PCM. Additionally, the liquid fraction is 1 if the temperature (T) is more than the melting

temperature ($T_{liquidus}$) of the PCM. The equation for the liquid fraction during the change of phase is provided below (ANSYS, 2020).

$$\beta = \frac{T - T_{solidus}}{T_{liquidus} - T_{solidus}} \tag{3.13}$$

The latent heat equation in terms of the liquid fraction and latent heat of material (L) is shown below (ANSYS, 2020).

$$\Delta H = \beta L_H \tag{3.14}$$

Therefore, the energy equation is as follows (ANSYS, 2020).

$$\frac{\partial}{\partial T}(\rho H) + \nabla \cdot (\rho \vec{v} H) = \nabla \cdot (k \nabla T) + S \tag{3.15}$$

3.5.1.3. Turbulence Modeling

The governing equations for the turbulence modeling was only activated where turbulent flows occurred. The turbulence model used for the numerical simulations is the k-ω Shear Stress Transport (SST) model. Menter (1994) introduced the k-ω SST model, where a blended function alternates between k-ω model and k-ϵ model. The k-ω model is better for solving the freestream flow whereas, the k-ϵ model is better for solving flow near the wall. Therefore, the combination of both these models result in a more accurate and reliable model that is capable of being utilized for a wide range of flows (ANSYS, 2020). The transport equations are shown in below equations (ANSYS, 2020):

$$\frac{\partial}{\partial t}(\rho k) + \frac{\partial}{\partial x_i}(\rho k \vec{v}_i) = \frac{\partial}{\partial x_j}\left(\Gamma_{\mathrm{k}} \frac{\partial k}{\partial x_j}\right) + G_k - Y_k + S_k + G_b \tag{3.16}$$

$$\frac{\partial}{\partial t}(\rho \omega) + \frac{\partial}{\partial x_i}(\rho \omega \vec{v}_i) = \frac{\partial}{\partial x_j}\left(\Gamma_{\omega} \frac{\partial \omega}{\partial x_j}\right) + G_\omega - Y_\omega + S_\omega + G_{\omega b} \tag{3.17}$$

The production of turbulent kinetic energy and specific dissipation rate are represented by G_k and G_ω, respectively. Furthermore, the dissipation of turbulent kinetic energy and specific dissipation

rate are represented by Y_k and Y_ω, respectively. Γ_k and Γ_ω, represent the effective diffusivities which can be obtained through following equations (ANSYS, 2020).

$$\Gamma_k = \mu + \frac{\mu_t}{\sigma_k} \tag{3.18}$$

$$\Gamma_\omega = \mu + \frac{\mu_t}{\sigma_\omega} \tag{3.19}$$

Where the turbulent Prandtl numbers, σ_k and σ_ω for k and ω, respectively, are characterized by following equations (ANSYS, 2020).

$$\sigma_k = \frac{1}{\frac{F_1}{\sigma_{k,1}} + \frac{1+F_1}{\sigma_{k,2}}} \tag{3.20}$$

$$\sigma_\omega = \frac{1}{\frac{F_1}{\sigma_{\omega,1}} + \frac{1+F_1}{\sigma_{\omega,2}}} \tag{3.21}$$

Where the blending function, F_1, is given in Equation (3.22), and ϕ_1 is characterized by Equation (3.23) (ANSYS, 2020).

$$F_1 = \tanh(\phi_1^4) \tag{3.22}$$

$$\phi_1 = \min\left[\max\left(\frac{\sqrt{k}}{0.09\omega y}, \frac{500\mu}{\rho y^2 \omega}\right), \frac{4\rho k}{\sigma_{\omega,2} D_\omega^+ y^2}\right] \tag{3.23}$$

Where the value of y is defined as the nearest wall distance. The positive portion of the cross-diffusion term, D_ω^+, can be obtained through following equation (ANSYS, 2020).

$$D_\omega^+ = \max\left[2\rho \frac{1}{\sigma_{\omega,2}} \frac{1}{\omega} \frac{\partial k}{\partial x_j} \frac{\partial \omega}{\partial x_j}, 10^{-10}\right] \tag{3.24}$$

Equation (3.25) defines the turbulent viscosity (μ_T), a term used in the k-ω SST model (ANSYS, 2020).

$$\mu_t = \frac{\rho k}{\omega} \frac{1}{\max\left[\frac{1}{\alpha^*}, \frac{S_r F_2}{a_1 \omega}\right]} \tag{3.25}$$

Where;

S_r is the strain rate magnitude,

α^* is the turbulent viscosity damping coefficient.

Where F_2 can be determined through Equation (3.26) and ϕ_2 can be determined through Equation (3.27) (ANSYS, 2020).

$$F_2 = \tanh(\phi_2^2) \tag{3.26}$$

$$\phi_2 = \max\left[2\frac{\sqrt{k}}{0.09\omega y}, \frac{500\mu}{\rho y^2 \omega}\right] \tag{3.27}$$

3.5.2. Mesh Independence and Time Independence Studies

The developed mesh is shown in Figure 3.15. A combination of tetrahedral and hexahedral mesh was used. Inflation layers were added to the air duct walls so that the boundary layer within the airflow could be captured.

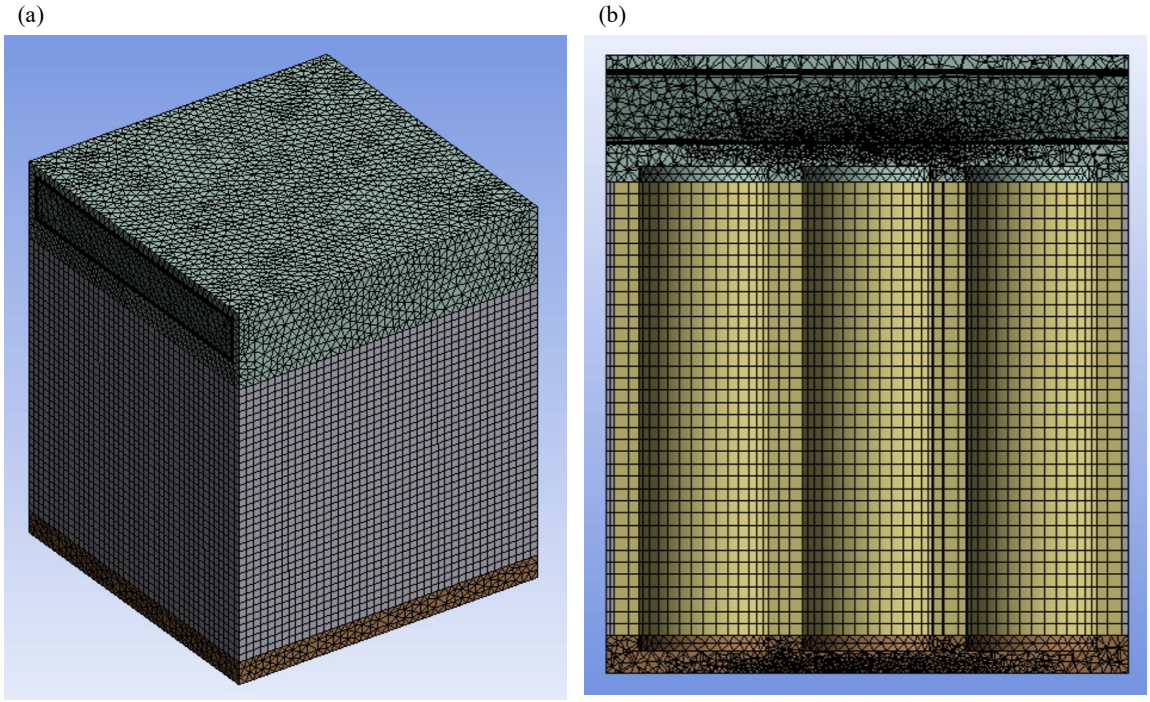

Figure 3.15: (a) Isometric view and (b)cross-section view at the center of the battery module mesh.

A mesh independence study was conducted to ensure that the results of the numerical model were independent of the size of the developed mesh. For this study, four meshes were developed. Each

subsequent mesh had an increment of approximately 50% elements. The velocity profile at the middle of the air duct was obtained and compared, as shown in Figure 3.16 (a). An average velocity was also calculated and plotted against the number of elements, as shown in Figure 3.16 (b). Based on the results, there is no significant difference beyond the mesh size of 614,024 elements; therefore, the medium mesh was selected.

Furthermore, a time independence study was performed to ensure that the results of the numerical model were independent of the size of the time step. This is required to reduce the computation power while maintaining the accuracy of the results. The result of this study is shown in Figure 3.16 (c). Based on the results, the time step size of 0.5 s was selected.

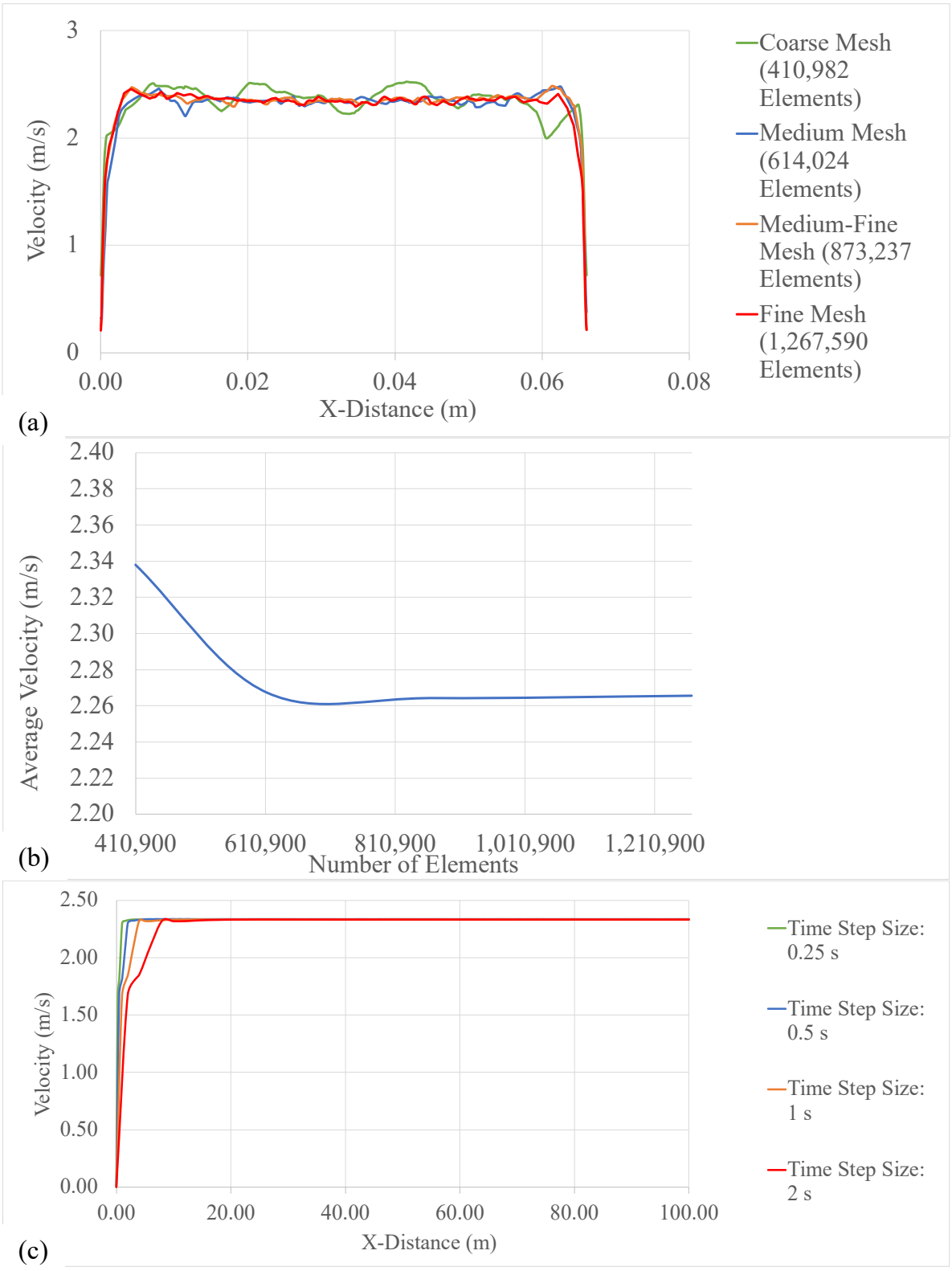

Figure 3.16: (a) Velocity profiles at the center of the air duct for the different mesh sizes; (b) Comparison of the average velocity for the different mesh sizes; (c) Temporal velocities at the center of the air duct for the different time step sizes.

3.5.3. Boundary Conditions

3.5.3.1. Feasibility Study, Comparison Study of Configurations, and Comparison Study of Primary Cooling Mediums of Strategy 1

The phase change phenomenon is based on time dependent conditions; therefore, transient simulations were performed. These studies were initially performed to establish the feasibility of Strategy 1. Thus, the heat generation of the cell already obtained through the experimental study conducted in the authors' previous research (Shahid & Agelin-Chaab, 2017) was used. The transient heat generation rate was obtained at the surface of the single insulated cell. The details of the experimental study along with the uncertainty analysis are provided in the authors' previous research (Shahid & Agelin-Chaab, 2017); therefore, it will not be repeated here. The average percentage uncertainty was calculated to be ±6.2%.

The heat generation source term was used as the boundary condition at the surface of the cells. A third order polynomial trendline was fitted to the transient heat generation results, and the equation obtained for the trendline is shown below. It is vital to include all the decimal places when defining the boundary condition to ensure that the trendline follows the experimental curve precisely.

$$Heat\ Generation\ Rate = 0.0003536908574066 08(t^3) - 0.900549870961498(t^2) + 716.501371877188(t) + 9309.34367960598 \quad (3.28)$$

Moreover, the ambient conditions for all configurations were set to 20 °C at atmospheric pressure. The airflow occurs in Strategy 1 (BM3-C1 to BM3-C5); hence, the inlet airflow velocity was set to 1.65 m/s based on the Reynolds number of 1,950. The characteristic length considered for the Reynolds number calculation was the hydraulic diameter of the air duct.

3.5.3.2. Validation of Numerical Model and Multiple Discharge Cycles

For this study, the heat flux at 1 C discharge rate was used as the boundary condition at the surface of the cells. This heat flux profile was obtained from Experiment 1. The ambient condition was set to 25 °C at atmospheric pressure. The inlet airflow velocity was set to 1.6 m/s based on the velocity obtained from the anemometer in Experiment 2 (Section 3.3.2). The material properties were applied to respective materials, as shown in Table 3.9.

Furthermore, six additional discharge cycles were run for a total of 7 discharge cycles. The results and conditions at the end of the preceding discharge cycle were used as the initial starting point for the start of the subsequent discharge cycle.

3.5.3.3. Analysis of Strategy 1 at Different Battery Module Discharge Rates

In this analysis, BM3-C1 configuration was considered, and the validated numerical model was used. The transient heat flux at the surface of the cell was changed based on the 1 C, 2 C, 3 C, 5 C, and 7 C discharge rates that were obtained through Experiment 1. The ambient condition was set to 25 °C at atmospheric pressure. The inlet airflow velocity was set to 1.6 m/s based on the velocity obtained from the anemometer in Experiment 2 (Section 3.3.2).

3.5.3.4. Development of Strategy 2 and Comparison with Strategy 1

In this study, all the simulations were conducted at atmospheric pressure with 25 °C ambient temperature. The inlet velocity of airflow for Strategy 1 (BM3-C1) was set to 1.6 m/s, which was obtained through Experiment 2. For Strategy 2 (BM4-C1 and BM4-C2), the velocity was set to 2.17 m/s. The Reynold number was kept the same for all the configurations at 1,950 and was based on the hydraulic diameter of the air duct. Since the cross-section area in BM4-C1 and BM4-C2

was reduced due to the cold plate protrusion, therefore, the velocity of airflow was increased to maintain the same Reynolds number. Finally, the heat flux boundary condition for 7 C discharge rate was used at the surface of the cells, which was obtained through Experiment 1.

3.5.3.5. Analysis on the Impact of Ambient Temperature on Strategy 2

In this study, the simulations were conducted at atmospheric pressure. The inlet velocity of airflow was set to 2.17 m/s. The heat flux boundary condition at 7 C discharge rate was considered as the worst-case scenario with the highest heat flux and was applied at the surface of the cells, which was obtained through Experiment 1. In order to investigate the effect of ambient temperature on Strategy 2, it was varied from 25 °C to 40 °C in increments of 5 °C.

3.5.3.6. Addition of Property Enhancing Materials to Paraffin based PCM in Strategy 2

In this analysis, the simulations were conducted at atmospheric pressure with 25 °C ambient temperature. The inlet velocity of airflow was set to 2.17 m/s. The heat flux boundary condition at 7 C discharge rate was applied at the surface of the cells, which was obtained through Experiment 1. Moreover, to evaluate the impact of the latent heat of the CPCM, the ambient temperature was set to the phase change temperature of the respective CPCM provided in Table 3.4. The CPCM was solid at the beginning of the discharge cycle and once the discharge process started the PCM started to melt due heat absorption from the cells.

3.5.3.7. Increasing the Thermal Conductivity of Water through Nanoparticles

For this analysis the ambient temperature was set to 42.24 °C to evaluate and compare the phase change of CPCM-4 with different fluid thermal conductivities. This is the temperature at which the CPCM-4 will start to change its phase. The CPCM-4 was solid at the beginning of the discharge

cycle and once the discharge process started the CPCM-4 started to melt due heat absorption from the cells. The inlet velocity of airflow was set to 2.17 m/s. The heat flux boundary condition at 7 C discharge rate was applied at the surface of the cells. Additionally, the configurations were also simulated at ambient temperature of 25 °C to evaluate the reduction in maximum temperature by the two configurations.

3.5.3.8. Parametric Study on the Volume of Paraffin based CPCM Combined with Copper Foam

For this parametric study the ambient temperature was set to 42.24 °C to evaluate and compare the phase change of CPCM-4 with different CPCM-4 volumes. The inlet velocity of airflow was set to 2.17 m/s. The heat flux boundary condition at 7 C discharge rate was applied at the surface of the cells.

3.5.3.9. Parametric Study on the Inlet Size of Battery Module

For this parametric study the ambient temperature was set to 42.24 °C. The heat flux boundary condition at 7 C discharge rate was applied at the surface of the cells. The inlet velocity was changed for test configurations as per Table 3.6.

3.5.3.10. Parametric Study on the Airflow Reynolds Number

For this parametric study the ambient temperature was set to 25 °C. The heat flux boundary condition at 7 C discharge rate was applied at the surface of the cells. The inlet velocity was changed for test configurations as per Table 3.7.

3.5.3.11. Study on Adding Fins to Improve the Heat Transfer

For this study the ambient temperature was set to 25 °C. The heat flux boundary condition at 7 C discharge rate was applied at the surface of the cells. The inlet velocity was changed for the three configurations as per Table 3.8.

3.5.3.12. Scalability Study of Battery Module

For this study the inlet air velocity was set to 3.12 m/s which is based on the Reynolds number of 1950. The heat flux boundary condition at 7 C discharge rate was applied at the surface of the cells. The ambient temperature was set to 25 °C. Moreover, For the airflow simulation only the inlet velocity was set to 3.12 m/s at an ambient temperature of 25 °C.

CHAPTER 4: RESULTS AND DISCUSSIONS

This chapter presents the results and discussions that were obtained from the experiments and numerical simulations. It is divided into 16 subsections. Subsection 1 provides the numerical model validation. Subsection 2 provides the discussion on the feasibility of Strategy 1 through thermal analysis, PCM melting analysis, and airflow analysis. Subsection 3 compares the different types of configurations developed for Strategy 1. Subsection 4 provides a comparison on the different types of primary coolants. Subsection 5 provides the experimental results. Subsection 6 provides an analysis of Strategy 1 and different discharge rates obtained through experiments. Subsection 7 discusses the results of Strategy 2 and its comparison with Strategy 1. Subsection 8 provides an analysis on the impact of changing ambient temperatures on Strategy 2. Subsection 9 provides the effect of adding performance enhancing materials (PEM) to PCM. Subsection 10 compares the effect of changing the fluid in the cold plates with nano-fluids to enhance thermal properties. Subsections 11, 12, and 13 provides the results of the parametric study used to reduce the amount of CPCM, fluid, and the airflow Reynolds number. Subsection 14 provides an analysis on increasing the heat transfer area of the cold plate within the air duct. Subsection 15 discusses the scalability aspect of the battery module and developed hybrid strategy. Finally, Subsection 16 provides a comparison of the developed strategy with results in open literature. The contents of this chapter have been partially taken from the candidate's published work (Shahid & Agelin-Chaab, 2023a, 2023b, 2023c, 2023d).

4.1. Numerical Model Validation

4.1.1. Heat Flux Profile

The heat flux profile for 18650 Li-ion cell at 1 C charge rate is shown in Figure 4.1. At 1 C discharge rate, a 2,500 mAh cell discharges at 2.5 A for 3,600 s (or 1 h). Therefore, the discharge cycle in Figure 4.1 ends at 3,600 s. It can be seen that the heat flux initially increases gradually up to ~83 W/m^2 until ~1,240 s, and then it decreases slightly to ~70 W/m^2 at 2,000 s. It increases again, and then the curve plateaus at approximately 3,000 s. In the final discharge stages, from 3,400 to 3,600 s, the heat flux increases sharply to the highest point of 170 W/m^2. This heat flux profile was used as the boundary condition at the surface of the cells for the numerical modeling. A sixth order polynomial trendline was fitted to the transient results, as shown by the dotted line in Figure 4.1. The R^2 – value of the fitted trendline was 0.9889, which confirms that the trendline follows closely to the actual heat flux measurements.

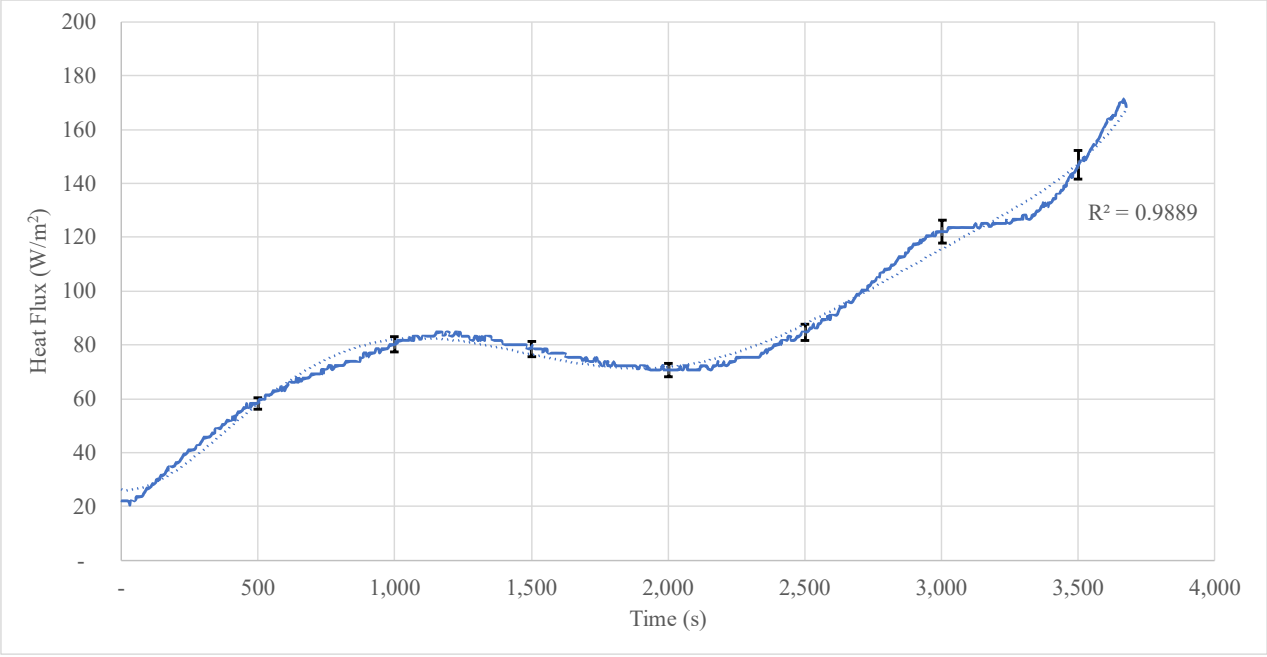

Figure 4.1: Transient heat flux at 1 C discharge rate.

4.1.2. Numerical Model Validation

Since the numerical model is based on the battery module developed for Experiment 2, therefore, the results of Experiment 2 were used for validation. The validation results are shown in Figure 4.2. Between the range of 1,400 – 2,400 seconds the numerical model slightly over-predicts the temperature of the cells. It can be seen in Figure 4.1 that the heat flux reduces and then increases slightly between this range. Since the experimental values for the heat flux were measured through Experiment 1 and temperature values were measured in Experiment 2. Therefore, the reduction in heat flux is a bit higher in Experiment 2 than the values obtained through Experiment 1 due to the experimentation error. Since the numerical model is based on the heat flux measurements from Experiment 1 therefore, it slightly over-predicts during this range. Moreover, towards the end of the experiment the temperature increased at higher rate compared to the numerical results. This is because there may be slight differences in the state of charge of cells due to multiple charging and discharging cycles as there was no battery management system which results in slightly early termination of the discharge cycle and marginally higher temperatures. However, the numerical results follow the experimental results closely and stays within ± 2% which is below the experimental error of ± 3.59%. Therefore, the results of the numerical model agree with the experimental results and the model is considered to be validated.

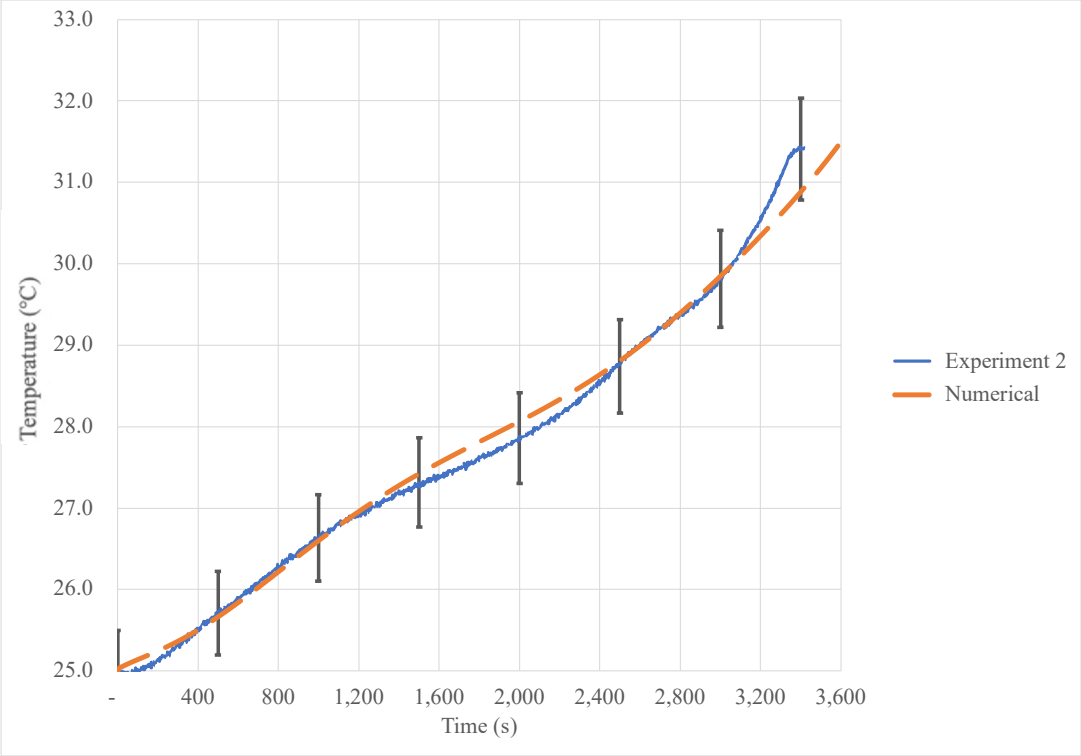

Figure 4.2: Comparison of numerical and experimental results for model validation.

4.2. Feasibility Study of Strategy 1

4.2.1. Thermal Analysis of Battery Module 1, 2, and 3

The thermal requirements for the Li-ion cells to perform effectively are to keep the maximum temperatures within the optimum operating temperature range of 25 – 40 °C and to keep the temperature uniformity below 5 °C. The temperature uniformity in terms of BTMS is the difference between the maximum and minimum temperature experienced by the cells within the battery pack. The temperature uniformity increases when the temperature difference decreases and vice-versa. Maintaining the temperature uniformity is essential for the proper regulation of the electrical balance within the battery pack and to prolong the life of the cells. The maximum and minimum temperatures of a cell and the battery module takes precedence over the average temperature. For example, a cell or the battery module may have a lower average temperature however, its temperature uniformity could be lower with a higher maximum temperature. Therefore, average temperature is not an effective parameter to analyze the cooling and the temperature uniformity of the cell and battery module.

A summary of the thermal performance of all three configurations is shown in Table 4.1. It provides the maximum and average temperature increase within the battery pack along with the temperature uniformity at the end of the discharge cycle. It can be seen that the maximum temperature increase in all three configurations stays within a difference of 0.1 °C. Similarly, the average temperature increase stays within a slight difference of 0.2 °C. This is primarily due to the latent heat of the PCM. Any heat generated that can increase the temperature of the cells beyond the limit of ~11.5 °C gets transformed into latent heat and is used to melt the PCM. Additionally, it can be seen that the temperature uniformity in BM1 and BM2 are very close, with a minute

difference of 0.03 °C. Whereas, the temperature uniformity of BM3 is approximately half of that of those at BM1 and BM2. This factor will be explained in the subsequent thermal analyses.

Table 4.1: Summary of thermal performance of BM1, BM2, and BM3.

Parameters	**BM1**	**BM2**	**BM3**
Maximum Increase in Temperature (°C)	11.56	11.53	11.46
Average Increase in Temperature (°C)	11.15	11.14	10.94
Temperature Uniformity (°C)	0.85	0.82	1.75

The maximum and minimum temperatures experienced by the three configurations over time are shown in Figure 4.3. The effect and impact of the PCM can be clearly seen in all three graphs as the temperature of the cells increases at a high rate. However, once the melting temperature of the PCM is attained, it starts to change its phase from solid to liquid, and the rate of temperature increase drops down significantly as the additional heat generated is used for the latent heat of phase change. Considering the maximum temperature trend, it can be seen that in BM1 (Figure 4.3 (a)), the phase change of the PCM starts at approximately 500 s; in BM2 (Figure 4.3 (b)), it starts at approximately 530 s, and in BM3 (Figure 4.3 (c)) starts at approximately 550 s. Moreover, at 600 s the maximum temperature reaches approximately 30.5 °C in all the three configurations. Since the primary coolant is PCM material therefore, once the melting of the PCM starts the temperature stabilizes at ~30.5 °C and then it increases slightly to maximum temperature towards the end of the discharge cycle. Additionally, it can be seen that the temperature difference between the maximum and minimum temperature towards the end of the discharge is low, hence the high temperature uniformity, as shown in Table 4.1. However, considering the temperature uniformity over time, it can be seen that in all three cases, the temperature uniformity is initially low (or poor uniformity), and when the temperature approaches the liquefication temperature of the PCM (30

°C) then the temperature uniformity begins to improve. A comparison of transient temperature uniformity is shown in Figure 4.4.

It can be seen from Figure 4.4 that the temperature difference increases in the first ~500 s, which reduces the temperature uniformity. At the peak of the curves in Figure 4.4, the phase change of the PCM starts and then the temperature difference begins to reduce. This is because the PCM restricts the maximum temperature to its melting temperature whereas, the minimum temperature within the battery pack keeps on increasing. This results in an increase in the temperature uniformity and the temperature difference reduces below the threshold of 5 °C.

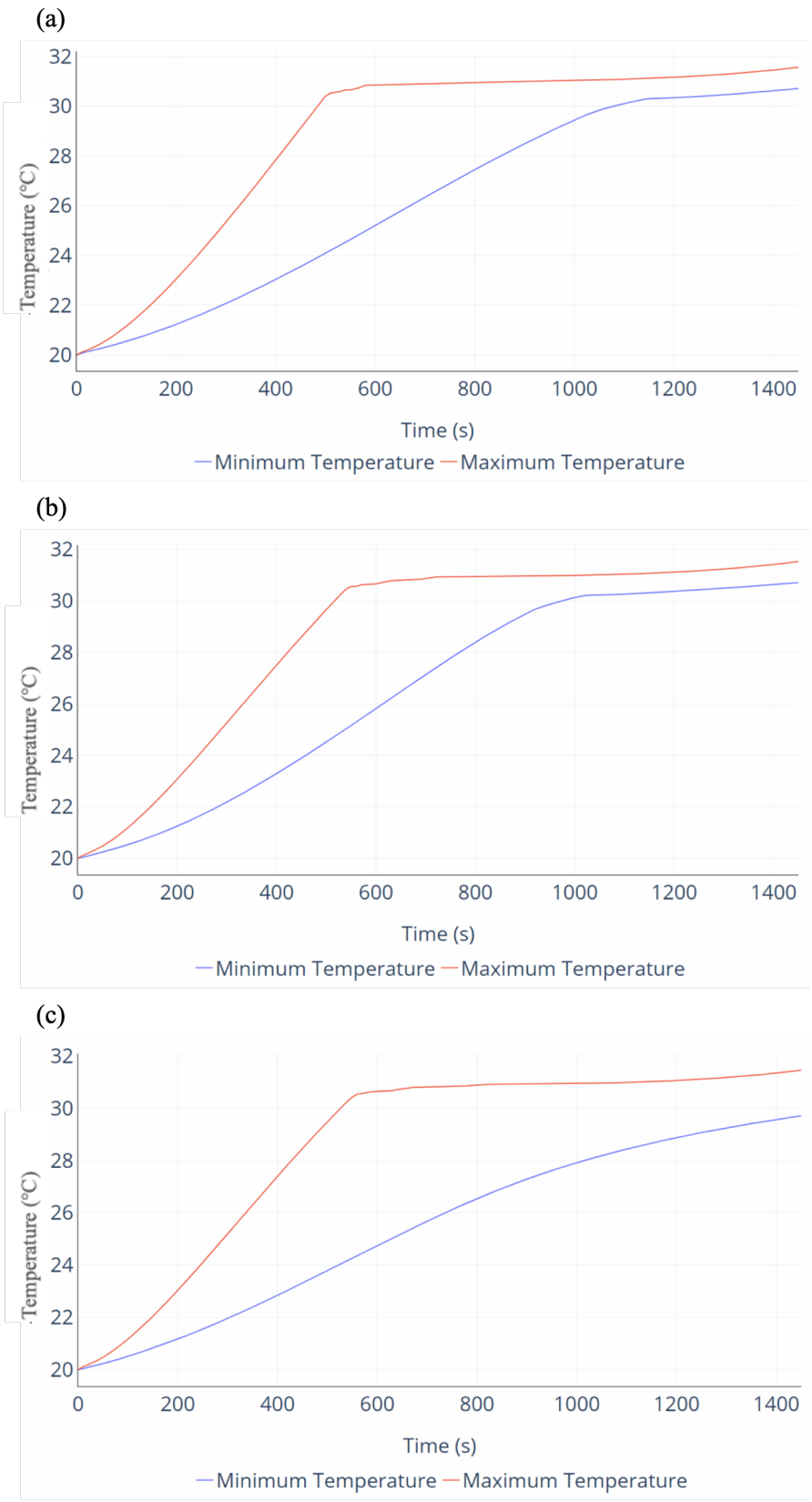

Figure 4.3: Transient maximum and minimum temperatures for (a) BM1, (b) BM2, and (c) BM3.

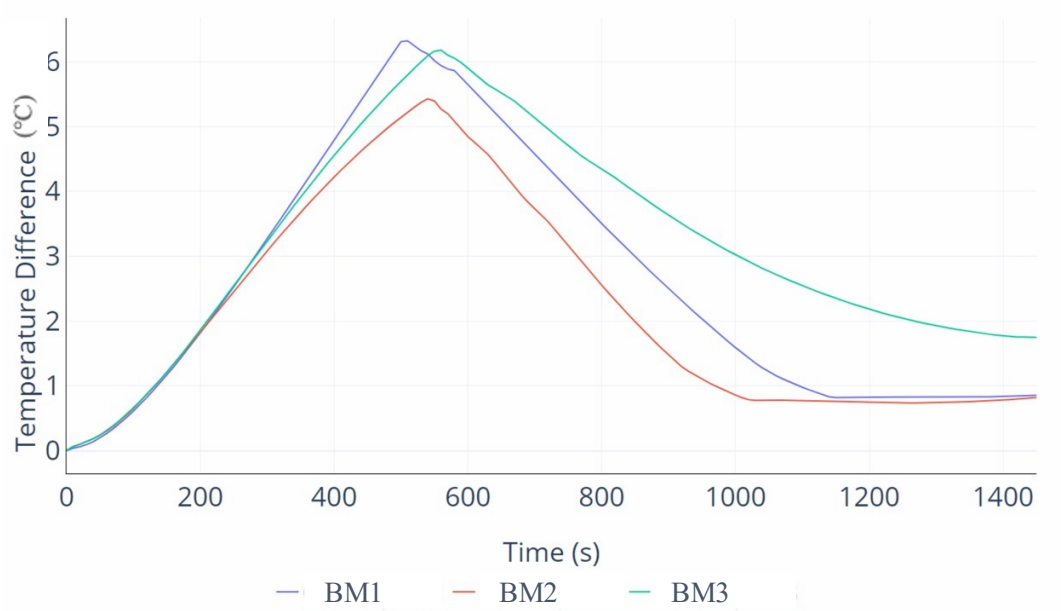

Figure 4.4: Comparison of transient temperature uniformity between BM1, BM2, and BM3.

In order to compare the three configurations, the temperature contours were extracted for all the configurations at the vertical planes, as shown in Figure 4.5 and Figure 4.6. There were two vertical planes created; one at the center of the battery module and the other in between the cells (at the center of the liquid channels). From Figure 4.4, it can be seen that the lowest temperature uniformity in all three configurations occur around 500 s; therefore, the temperature contours at 500 s are shown in Figure 4.5, and the temperature contours at the end of the discharge cycle are shown in Figure 4.6. Comparing BM1 (Figure 4.5 (a) and (b)) and BM2 (Figure 4.5 (c) and (d)), it can be seen that the PCM in BM1 exhibits higher temperatures compared to the PCM in BM2. This is because in BM2, there are liquid channels that extract some of the heat from the PCM, therefore, the temperature of the PCM is slightly lower. A similar result can also be observed in Figure 4.6.

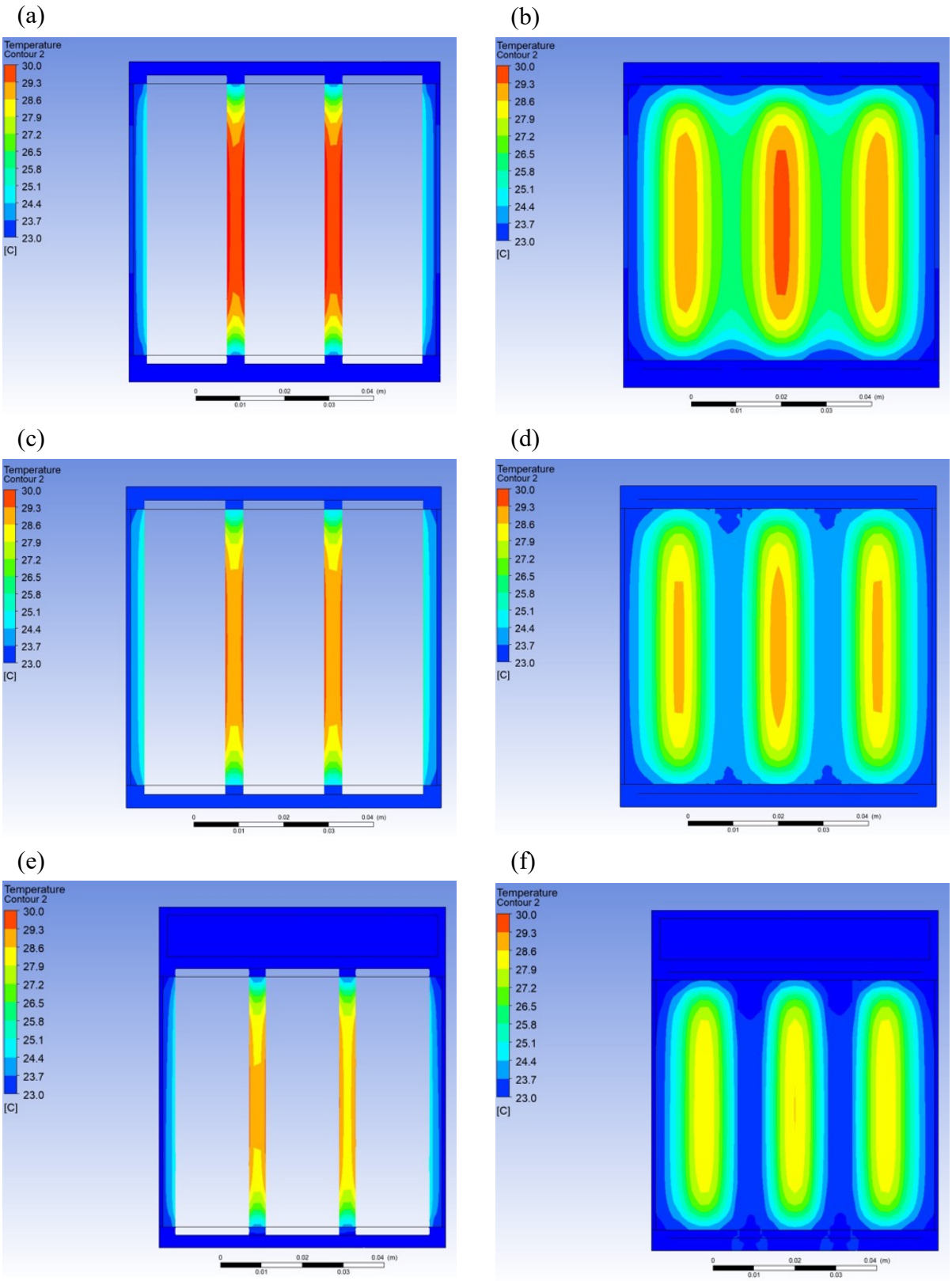

Figure 4.5: Temperature contours at the (a) center of BM1, (b) between the cells of BM1, (c) center of BM2, (d) between the cells of BM2, (e) center of BM3, (f) between the cells of BM3 at 500 s.

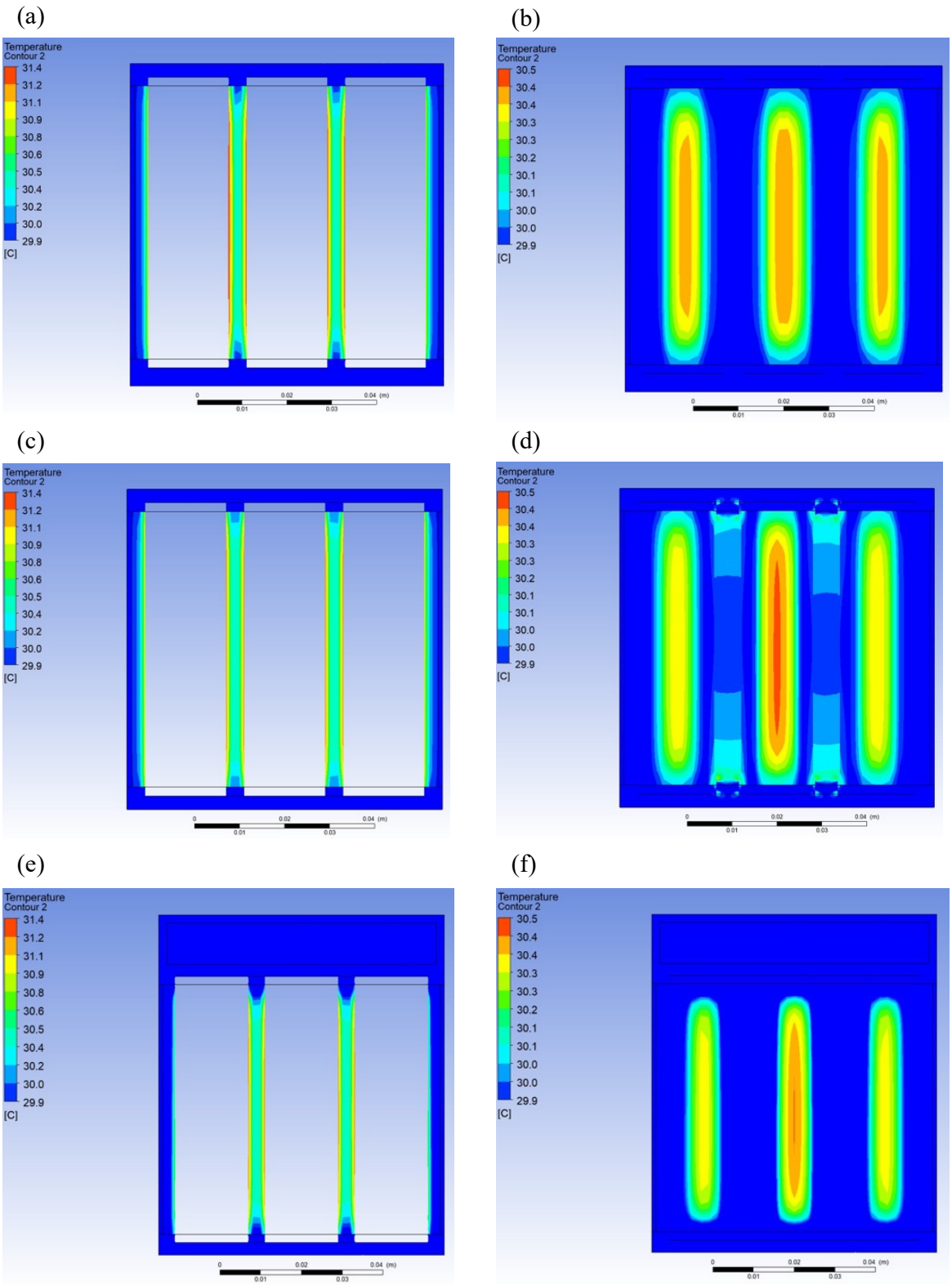

Figure 4.6: Temperature contours at the (a) center of BM1, (b) between the cells of BM1, (c) center of BM2, (d) between the cells of BM2, (e) center of BM3, (f) between the cells of BM3 at the end of discharge.

Although the fluid in the liquid channels extracts some heat from the PCM, an additional system is required to take the heat away from the fluid because the fluid is stationary and not moving. This is why BM3 was developed, which allows continuous moving airflow to extract heat away from the fluids. Comparing the contours of BM2 and BM3 from Figure 4.5 and Figure 4.6, it can be seen that the temperature of the PCM further reduces in BM3 as the red zones are eliminated, and the orange zones in the contours are reduced. In BM3, the fluid extracts heat from the PCM, similar to BM2; however, the airflow extracts heat from the fluid, which renews the heat extraction capacity of the fluid. Therefore, the fluid extracts additional heat from the PCM and reduces its temperature. This then allows the PCM to extract more heat from the surface of the cells. From Figure 4.5 (d) and (f) and Figure 4.6 (d) and (f), it can be seen that the temperature of the fluid is lower, indicating the effective heat extraction from the fluid through airflow. A similar deduction can also be made from the results shown in Figure 4.7. The difference in this is that the plane selected for the contour is a horizontal plane placed at the center of the battery pack. It can be seen that BM1 has the most contours of the red zone and BM3 has the least, which confirms that BM3 provides the most effective cooling compared to BM1 and BM2.

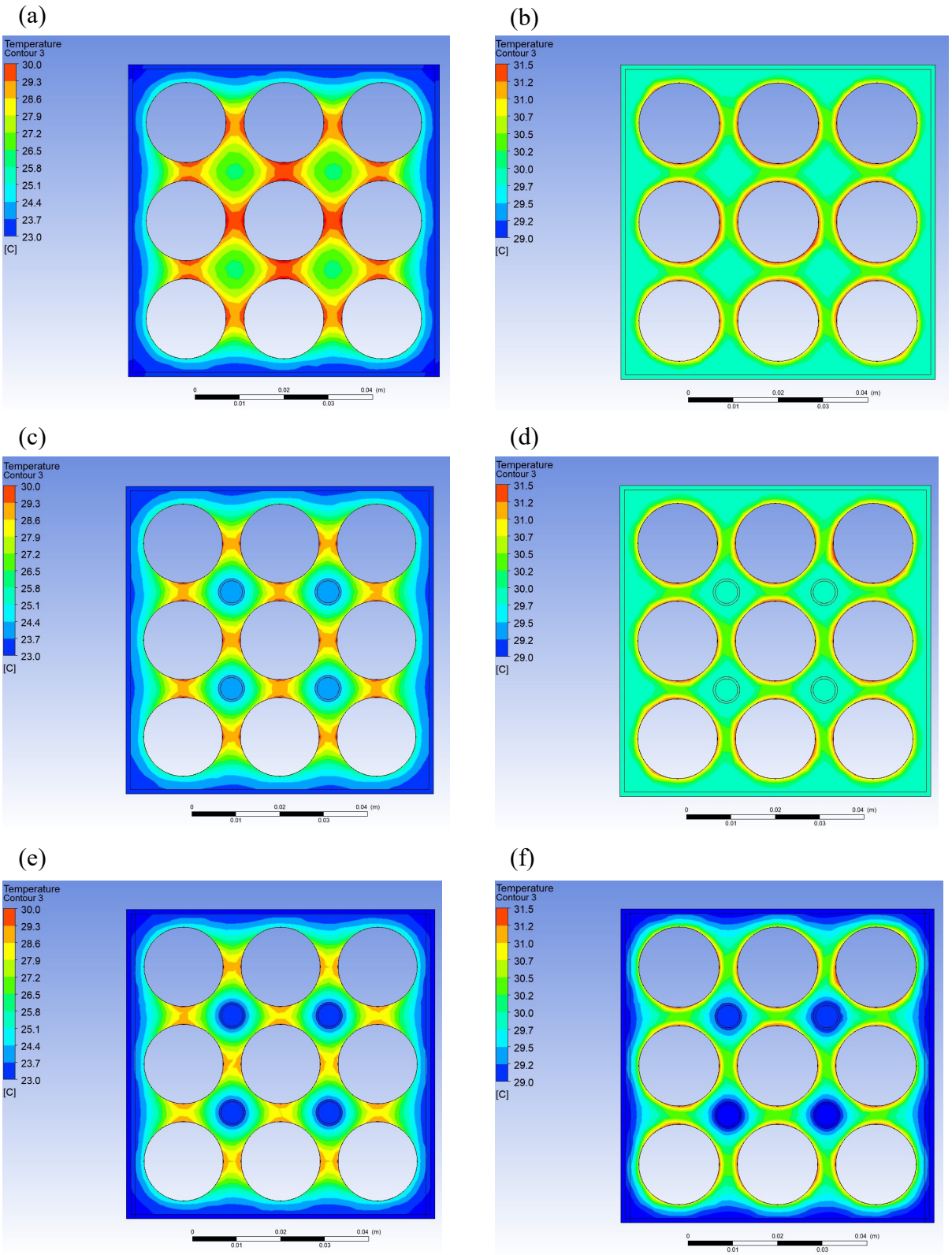

Figure 4.7: Temperature contours at the center of the battery pack; (a) BM1 at 500 s, (b) BM1 at the end of discharge, (c) BM2 at 500 s, (d) BM2 at the end of discharge, (e) BM3 and 500 s, (f) BM3 at the end of discharge.

Finally, the contours at the surface of all the cells in an isometric projection are shown in Figure 4.8. This is required to understand the temperature uniformity within the cells. In all three configurations, the minimum temperature occurs at the top and bottom cell regions that are in direct contact with the aluminum battery pack enclosure. These have low temperatures because the heat generated from these surfaces is transferred to the aluminum enclosure. Therefore, in Figure 4.3, we have a region where the heat is directly transferred to the PCM (maximum temperature lines) and a region where the heat is transferred to the aluminum enclosure and then to the PCM from that enclosure (minimum temperature line).

Since BM1 and BM2 have no airflow; therefore, all the heat is subsequently extracted through the PCM. This is also evident in Figure 4.3 where the PCM at the minimum temperature area also starts to change phase. However, in BM3, a portion of the heat in the aluminum enclosure is also transferred to the airflow that flows through the duct, which is an extension of the aluminum enclosure. This further reduces the temperature of the enclosure, and the enclosure extracts extra heat from the top and bottom surfaces of the cells. This causes a reduction in the temperature uniformity of the battery pack compared to BM1 and BM2, which can be seen in Figure 4.8.

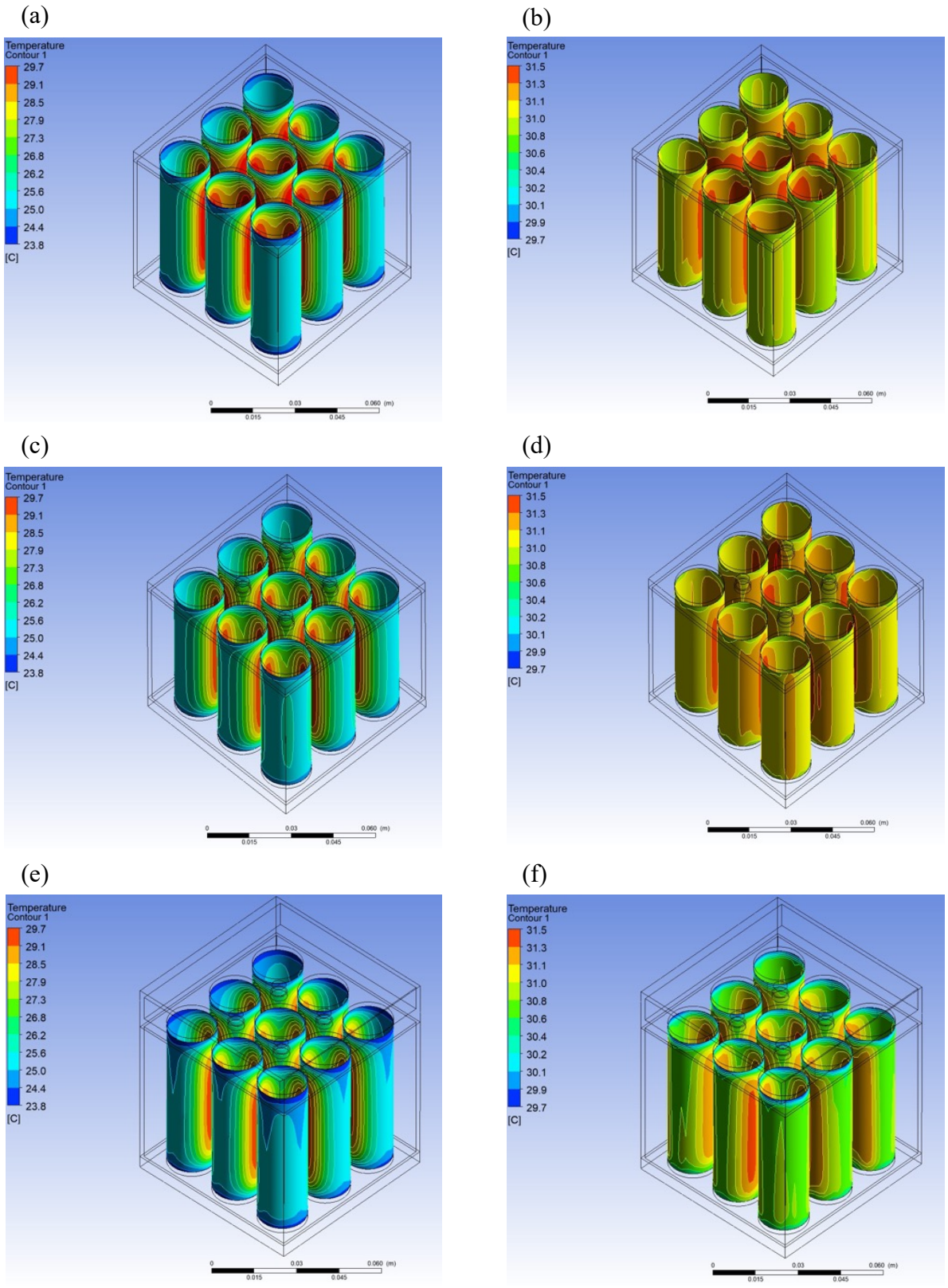

Figure 4.8: Temperature contours of the cells in (a) BM1 at 500 s, (b) BM1 at the end of discharge, (c) BM2 at 500 s, (d) BM2 at the end of discharge, (e) BM3 and 500 s, (f) BM3 at the end of discharge.

4.2.2. PCM Melting Analysis of Battery Module 1, 2, and 3

The improvement in the BTMS through the development of the configurations is examined by studying the amount of PCM that transforms in the liquid phase. The less the PCM gets used up and changes its phase, the more effectively the configuration performs. Also, a lower PCM utilization allows multiple charge-discharge cycles. Whereas a high PCM utilization in a single discharge cycle would result in less PCM availability for the subsequent charge-discharge cycles. Moreover, once the PCM changes phase then the latent heat is no longer effective, and the heat extraction reduces resulting in an increase in the cell temperature. Hence, the target is to utilize the least amount of PCM using the secondary coolants.

The result of this study is shown in Table 4.2. It can be seen that BM1 has the highest percentage that transforms into liquid phase with 10.33%. This is followed very closely by BM2 with 10.27%, a difference of 0.06%. This negligible difference in BM1 and BM2 is because the heat is not expelled into the environment in these two BTMS but trapped within the system. Finally, BM3 has the lowest percentage, 6.13%. This shows that approximately 69% less PCM was used by adding an air duct and allowing the airflow to extract heat from the fluid. Therefore, BM3 is the most effective strategy based on the phase change analysis.

Table 4.2: Comparison of liquid fraction present at the end of the discharge cycle.

Parameters	**BM1**	**BM2**	**BM3**
Liquid Phase Volume (mm^3)	13,987.26	13,991.84	8,303.97
Liquid Fraction Percentage (%)	10.33	10.27	6.13

4.2.3. Airflow Analysis of Battery Module 3

A final analysis is done for the airflow. Since BM3 is the only configuration in which airflow is introduced, therefore, for this analysis, only BM3 is considered. Figure 4.9 provides the velocity and temperature of the airflow within the air duct. It can be seen that flow develops as it passes through the air duct. The flow near the wall is stationary, and the boundary layer develops at the top surface and the bottom surface of the air duct. Additionally, it can be seen from Figure 4.9 (b) that the airflow extracts heat from the aluminum enclosure and fluid in liquid channels, as discussed previously. However, there is a large portion of airflow in between the lowest temperatures. This portion of the airflow is completely unused as it is not extracting any form of heat.

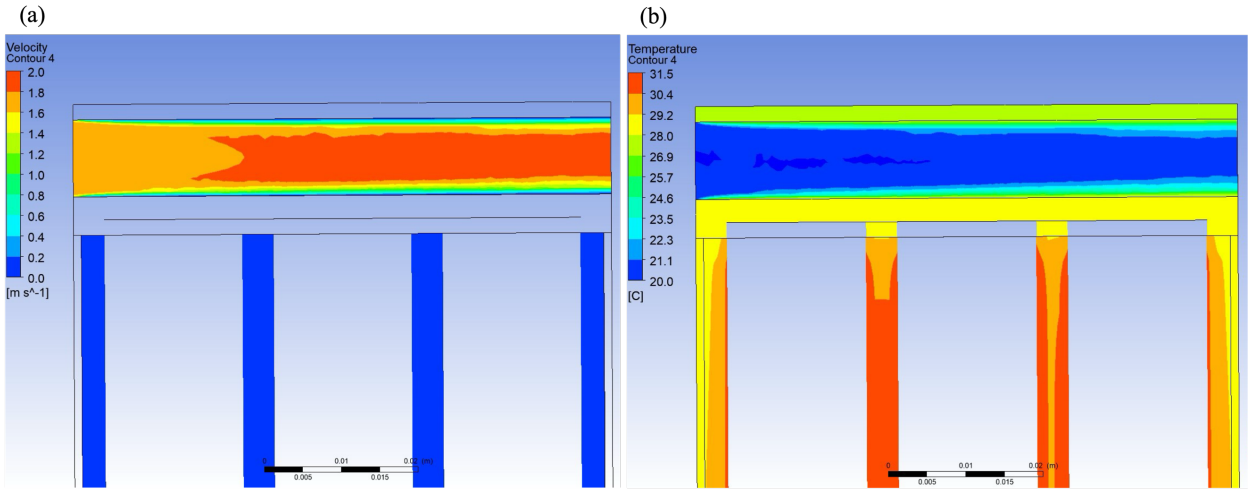

Figure 4.9: (a) Airflow velocity contour and (b) temperature contour of BM3 at the end of the discharge cycle.

4.3. Comparison Study of Configurations of Strategy 1

The maximum and minimum temperatures with respect to time for all the configurations are provided in Figure 4.10 (a), (b), and (c). Additionally, the temperature contours at the end of the discharge cycle for all the configurations are provided in Figure 4.10 (d), (e), and (f).

As shown in Figure 4.10, in all the configurations the maximum temperature of the cells is limited by the phase change temperature of the PCM material, therefore, the temporal curve of maximum temperature is almost identical. Once the phase change temperature of the PCM is reached at ~500 s, then the maximum temperature curve flattens out, and the temperature is maintained. The minimum temperature in BM3-C1 is higher than the minimum temperatures in BM3-C2 and BM3-C3. This is because, in BM3-C2 and BM3-C3, the minimum temperature occurs in the region where the cell is in contact with water. Due to the higher thermal conductivity and specific heat capacity of water low temperatures are observed. The airflow with the duct allows the air to extract some of the heat from water as well, which increases the heat extraction capacity of water, allowing more heat transfer from the surface of the cell that is in contact with water. The reduced minimum temperature in BM3-C2 and BM3-C3 results in a decrease in the temperature uniformity, as shown in Figure 4.11.

Additionally, from Figure 4.10 it can be seen that in BM3-C1 the surface of the cells in facing the neighbouring cells have higher temperatures, whereas the surface of the cell facing the battery pack housing and liquid channels have slightly lower temperatures. Moreover, in BM3-C2 and BM3-C3 it can be seen that the surface of the cell in contact with water has the lowest temperatures as discussed earlier.

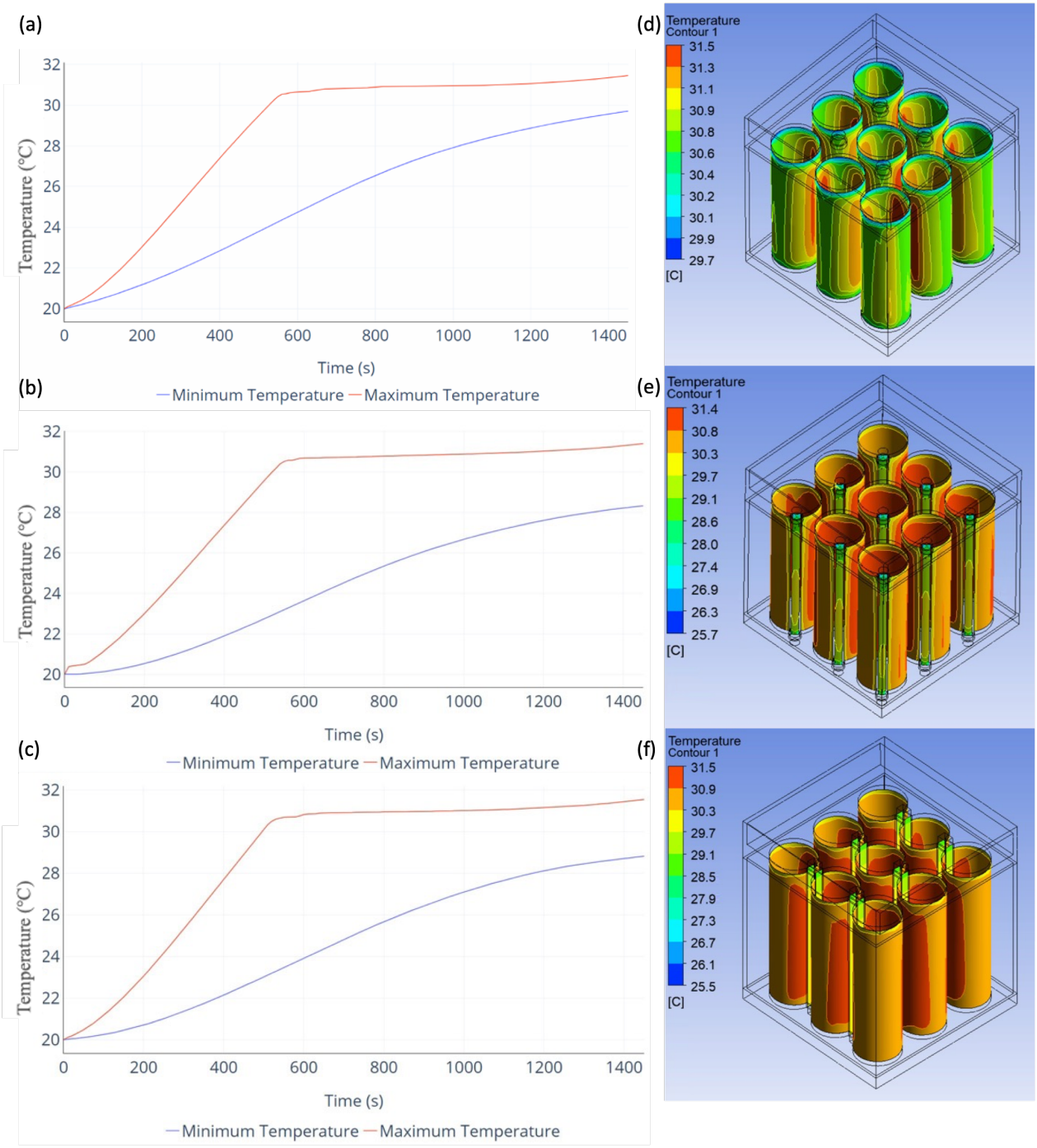

Figure 4.10: Transient maximum and minimum temperature for (a) BM3-C1, (b) BM3-C2, (c) BM3-C3, and temperature contours at the end of discharge cycle for (d) BM3-C1, (e) BM3-C2, and (f) BM3-C3.

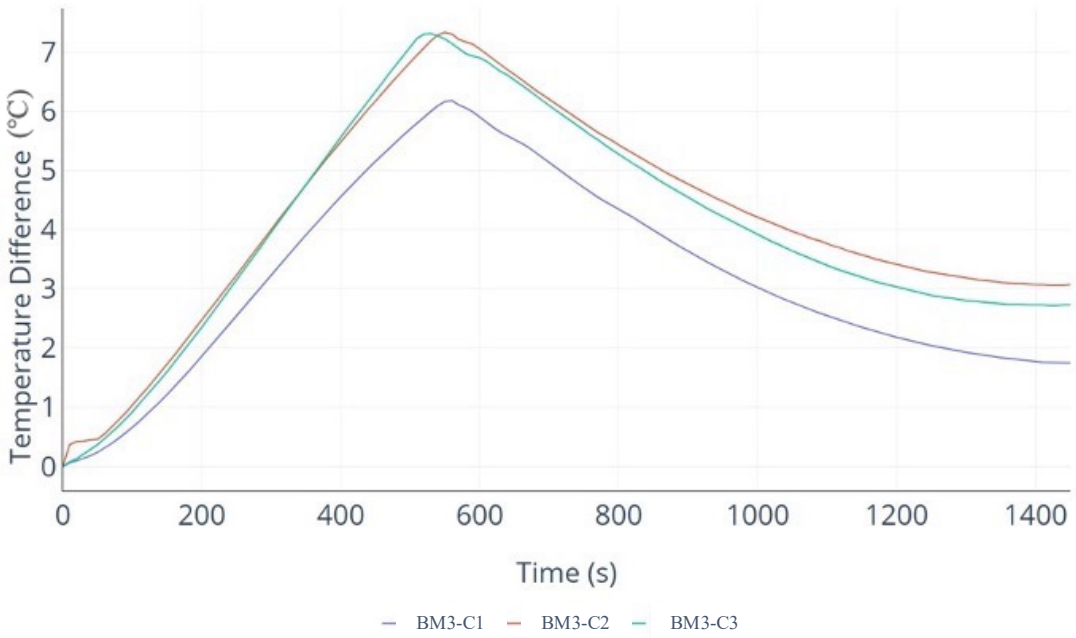

Figure 4.11: Comparison of transient temperature uniformity between BM3-C1, BM3-C2, and BM3-C3.

It can be seen from Figure 4.11 that the temperature uniformity in all three configurations decreases until the temperature reaches the point where the phase change of the PCM begins. At this point, the maximum temperature is limited, however, the minimum temperature of the cell keeps on increasing, which reduces the temperature difference. This then allows the hybrid BTMS to increase the temperature uniformity of the battery pack. Moreover, the highest temperature uniformity is exhibited by BM3-C1 when compared to BM3-C2 and BM3-C3.

Finally, the amount of PCM that was converted into liquid was extracted from the numerical results. The liquid fraction was 6.13% for BM3-C1 and 5.93% for BM3-C2 and BM3-C3. Since some of the heat from the surface of the cells was directly extracted by the fluid in BM3-C2 and BM3-C3, therefore, a slight decrease in the liquid fraction percentage was exhibited. However, due to a hybrid design by which water and air extract heat from the PCM, a low usage of approximately 6% is achieved.

4.4. Comparison Study of Primary Cooling Mediums in Strategy 1

The transient temperature profiles for BM3-C1, BM3-C4, and BM3-C5 are shown in Figure 4.12 (a), (b), and (c), and the temperature contours at the end of the discharge cycle are shown in Figure 4.12 (d), (e), and (f). The analysis of BM3-C1 has been discussed in previous sections. In BM3-C4 both the maximum and the minimum temperatures do not reach the phase change temperature of PCM during the discharge cycle, therefore, the gap between the maximum and minimum temperature keeps increasing. This results in a reduced temperature uniformity throughout the discharge cycle. Towards the end of discharge there is a temperature non-uniformity of 10 °C.

For BM3-C5, the maximum temperature increases throughout the discharge cycle and follows the heat generation rate of the cell. As the rate of heat generation reduces between 600 s and 1200 s, the rate of temperature increase also reduces and then increases, corresponding to an increase in the rate of heat generation. Since there is no continuous flow of fluid within the battery pack, the maximum temperature of the fluid also increases, and the secondary cooling medium (airflow) on top of the battery pack is not sufficient to provide enough cooling to keep the temperatures within the desired ranges. The maximum temperature goes beyond 60 °C, and the minimum temperature increases to more than 40 °C.

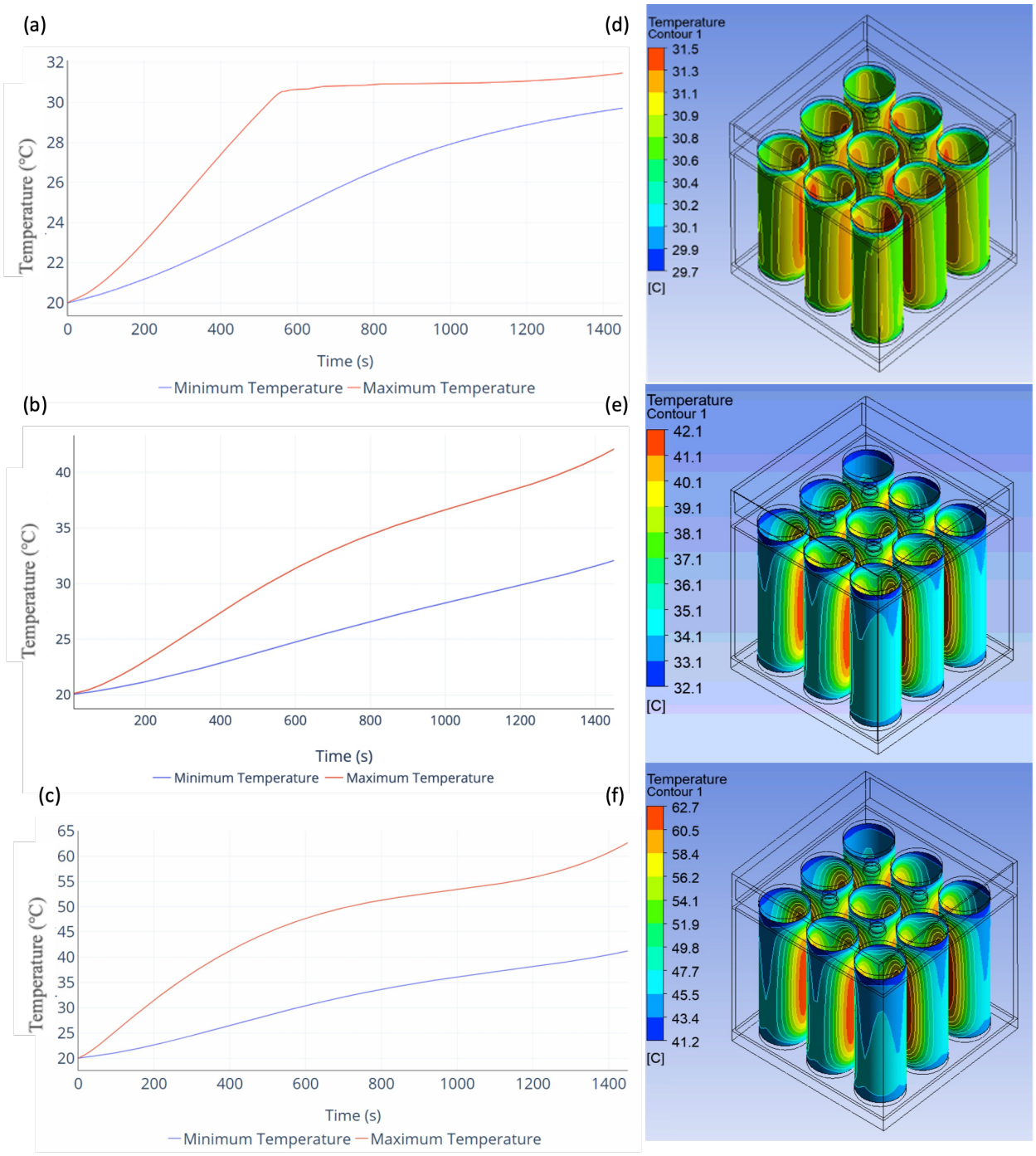

Figure 4.12: Transient maximum and minimum temperature for (a) BM3-C1, (b) BM3-C4, (c) BM3-C5, and temperature contours at the end of discharge cycle for (d) BM3-C1, (e) BM3-C4, and (f) BM3-C5.

It can be seen from Figure 4.12 (d), (e), and (f) that in all the configurations the temperature of the surface of the cell that faces the neighbouring cells is higher and the surface facing the battery pack housing is lower. Moreover, the lowest temperature is experienced by the part of the cell that in contact with the top plate and bottom plate of the housing. This is due to higher heat transfer through conduction between the cell and the top and bottom plates. Additionally, the airflow extracts some heat from the surface of the top plate which allows additional heat transfer from the cell surface, and it results in reduced temperatures at the top surface of the cell.

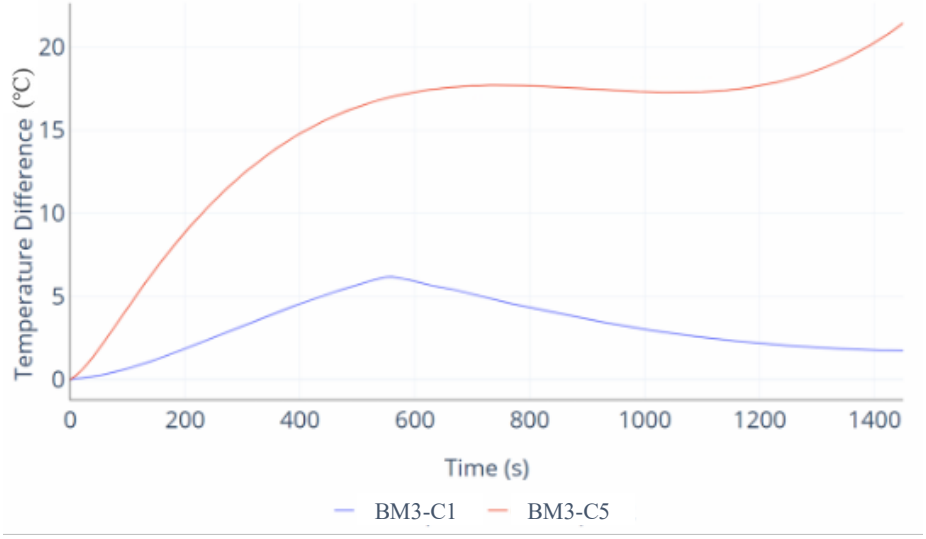

Figure 4.13: Comparison of transient temperature uniformity between configurations BM3-C1 and BM3-C5.

The difference between the maximum and minimum temperatures is shown in Figure 4.13. It can be seen that in BM3-C5 the temperature difference goes beyond 20 °C, which is not favourable for the operation of the Li-ion cells. Whereas, in BM3-C1, the temperature difference increases initially until phase change temperature is reached, and then it starts to reduce. Beyond ~500 s, the maximum temperature is maintained within a constant phase change temperature range, and the minimum temperature keeps increasing, which reduces the temperature difference and increases the temperature uniformity.

4.5. Experimental Temperature Profile and Multiple Discharge Cycle Analysis

4.5.1. Temperature Profile of Battery Module

Experiment 2 was conducted at a 1 C discharge rate. Since the cells were connected in series, therefore, the battery module was discharged at 2.5 A at an ambient of 25 °C. The transient temperature profile is shown in Figure 4.14. It can be seen that the temperature increases in all the cells follow the same trend. This trend corresponds to the heat flux profile shown in Figure 4.1. In areas where the heat flux reduces, the temperature increase rate also reduces and where the heat flux increases, the temperature increase rate also increases. At the end of the discharge cycle, the maximum temperature of the battery module was ~32.5 °C, and the minimum temperature was ~31.3 °C. This corresponds to a temperature uniformity of 1.2 °C.

The highest temperatures are exhibited by cell numbers C5, C6 and C8. Cell C5 is in middle of the battery module; therefore, the heat from the surrounding cells impacts the cell in the middle resulting in the highest temperature of the battery module. Moreover, for cells C6 and C8 the thermocouple was placed facing the center of the battery module; therefore, the surface of the cell that is facing towards the center of the battery module has a higher temperature. In contrast, cells C1 and C2 show the lowest temperatures, and this is because the thermocouple in these cells is placed on the surface of the cell facing the housing of the battery module. Additionally, cells C4 and C7 show intermediate temperature values of the battery module. In the case of cells C4 and C7 the thermocouple was placed on the surface facing each other. This is how temperature non-uniformity occurs at the cell level. The surface of the cell facing the center of the battery module has the highest temperature, whereas the surface of the cell that is facing the neighboring cells have intermediate temperatures, and the surface of the cell facing the housing of the battery module

has the lowest temperatures. Also, the temperature difference between the different cells shows the temperature non-uniformity within the battery module as well. As stated earlier, the primary objective of developing this configuration is to maintain the temperature uniformity to within 5 °C. However, due to the limited measuring capabilities of the experimental setup, it was not possible to measure the temperature of each cell at different surface points. Therefore, a numerical model was developed, and numerical simulations were performed to obtain the surface contours of all the cells within the battery module.

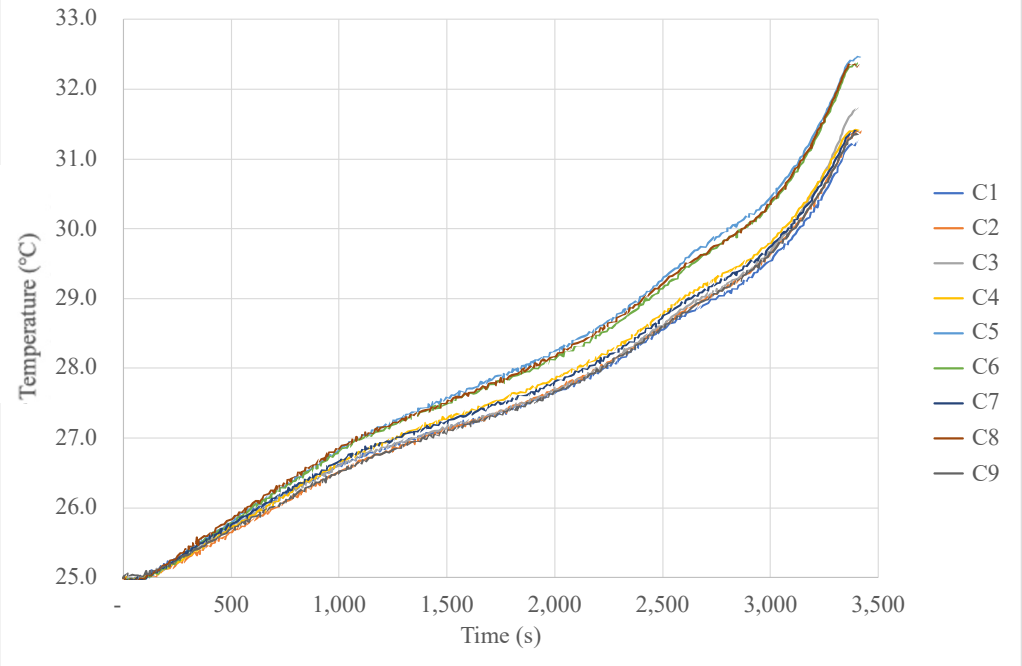

Figure 4.14: Temperature profile at 1 C discharge rate of Experiment 2.

4.5.2. Thermal Analysis of Single Discharge Cycle

Using the developed and validated numerical model, simulations were conducted using the methodology described in Section 3.5. An overview of the maximum and minimum temperature exhibited by the battery module and its temperature uniformity is shown in Figure 4.15.

The maximum temperature at the end of the discharge cycles reached 31.5 °C, and the minimum temperature reached 27.4 °C. According to Figure 4.15 (a), the maximum temperature increases at a higher rate than the minimum temperature increase. Additionally, the temperature uniformity also reduces due to the different temperature increase rates. By the end of the discharge cycle, the temperature uniformity is still high, with a value of 2.1 °C.

For an in-depth understanding, the temperature contours at the end of the discharge cycle of the cells are shown in Figure 4.16 (a). Moreover, temperature contours for the PCM material at the center plane of the battery module are shown in Figure 4.16 (b). It can be seen from Figure 4.16 (a) that the locations of high temperature regions are the center of the cells. The surfaces facing the neighboring cells have higher temperatures compared to the surfaces facing the battery module housing due to the compound heating effect from the neighboring cells. Additionally, the surfaces that are in contact with the top plate and the bottom plate of the battery module have comparatively lower temperatures due to heat conduction from the cell to the module housing. However, the surface of the cell at the top plate exhibits the minimum temperatures due to the air-cooling effect that occurs at the top plate. So, the top plate cools due to air cooling, and then this allows additional conduction from the cell surface to the top plate.

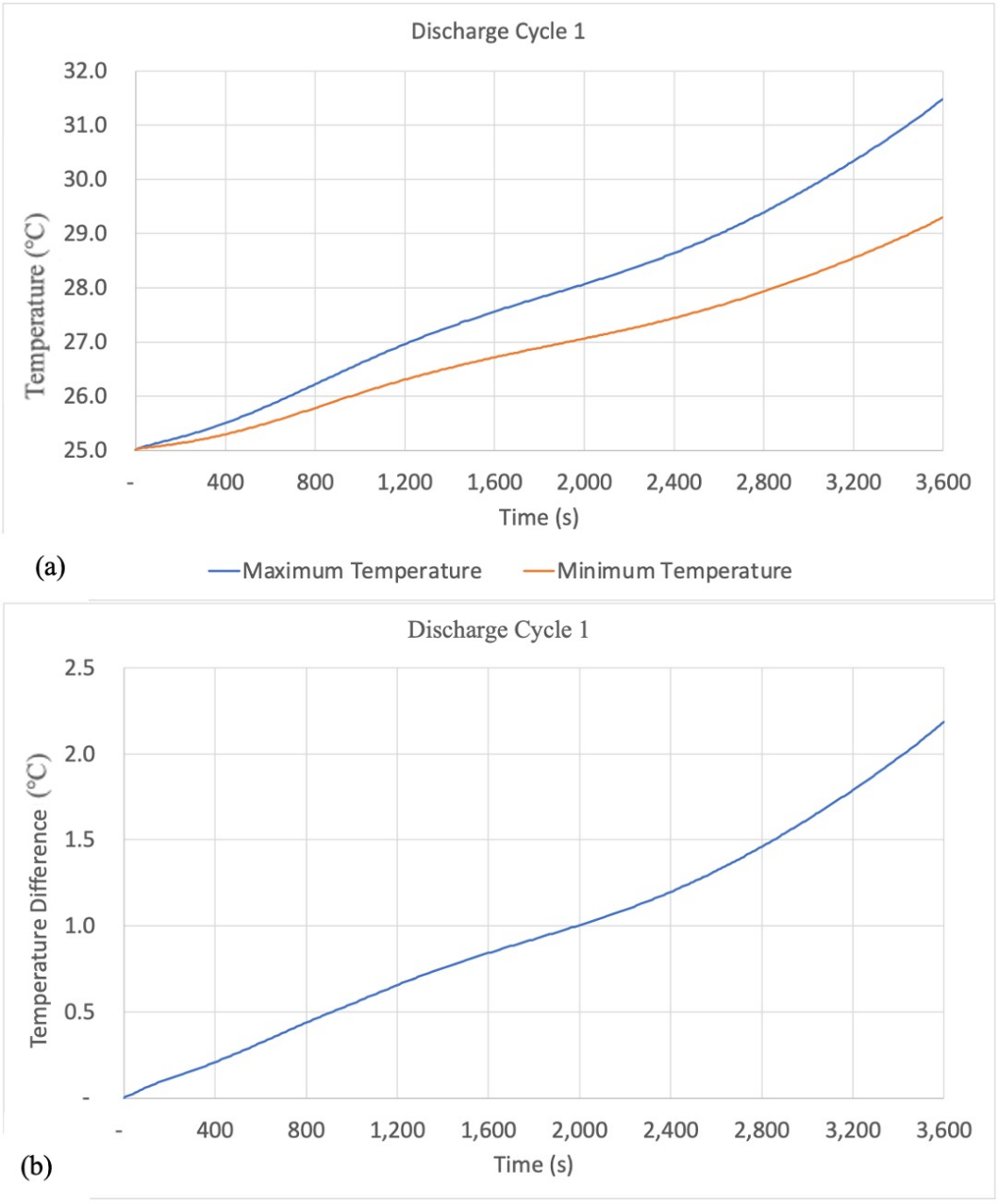

Figure 4.15: (a) Temperature profiles and (b) temperature uniformity profile of the battery module.

Moreover, the compound heating effect between the cells can be visualized in Figure 4.16 (b). The PCM sandwiched between the surfaces of the two adjacent cells has the highest temperature as there is no additional heat sink directly between the cells for the heat to dissipate. For all the other surfaces there are additional heat sinks in the form of module housing and liquid channels. Therefore, the temperature is lower in these areas. Additionally, since the maximum temperature

is below the phase change temperature of the PCM the phase change does not occur and latent heat of the PCM is not utilized. It is only using the thermal conductivity and heat capacity to transfer heat through conduction during this discharge cycle. Therefore, to assess the thermal performance of the proposed configuration multiple discharge cycles were simulated.

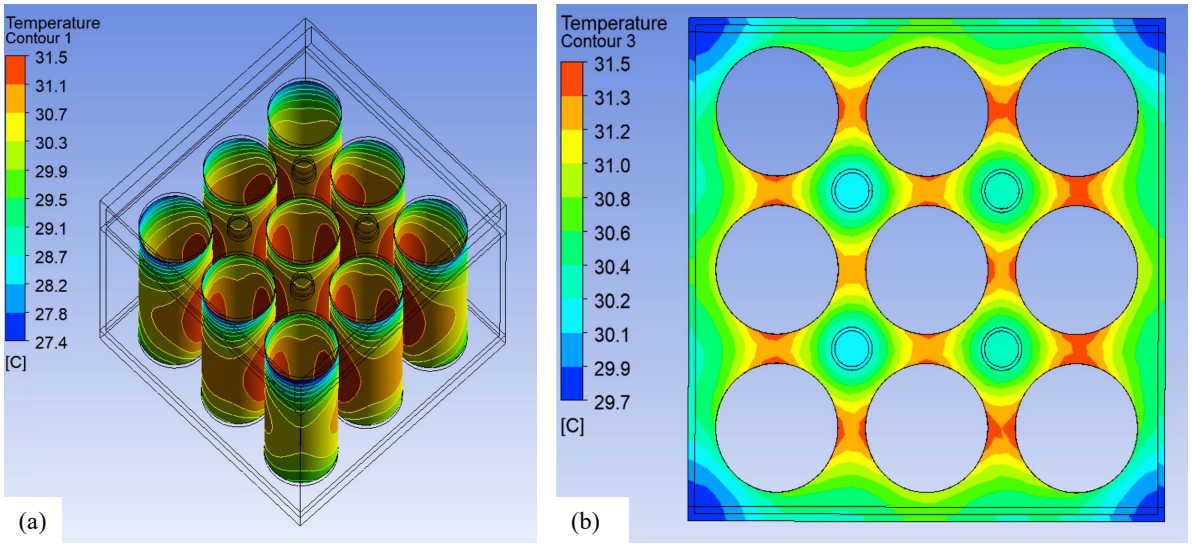

Figure 4.16: Temperature contours at the end of the discharge cycle for (a) cell and (b) PCM at the mid-plane of the battery module.

4.5.3. Thermal Analysis of Multiple Discharge Cycles

Six more discharge cycles were simulated in addition to the first one described in previous section. The final conditions at the end of the first cycle were used as the initial condition for the second discharge cycle. This was then repeated for all the subsequent discharge cycles. The temperature profiles for the maximum and minimum temperatures for discharge Cycles 2, 3, and 4 are shown in Figure 4.17. It can be seen that the maximum temperature increases up to 35.3 °C in discharge Cycle 2, and then it increases to 39 °C in discharge Cycle 3, and finally to 41.7 °C in discharge Cycle 4. Initially, the heat removal from the PCM is low at lower temperatures, and the rate of

temperature increase is low, however, as the temperatures approach the phase change temperature of the PCM, the heat removal of the PCM increases, resulting in a lower temperature increase rate.

By the end of the fourth discharge cycle, the maximum temperature reached the phase change temperature of the PCM. Therefore, three additional discharge cycles were simulated, and the temperature profiles are shown in Figure 4.18. The phase change temperature of the PCM ranges between 42 – 44 °C as stated in Table 3.2. Hence, it can be seen that the maximum temperature in discharge Cycles 5, 6, and 7 stays within the phase change temperature range. From discharge Cycle 5 the PCM starts to melt, and any additional heat generated in the cell is extracted by the PCM using latent heat. Since the PCM around the cell is melting, therefore, any heat generated in the minimum temperature region of the cell is being extracted by the latent heat of the PCM, and the temperature increase rate in the minimum temperature profile is low.

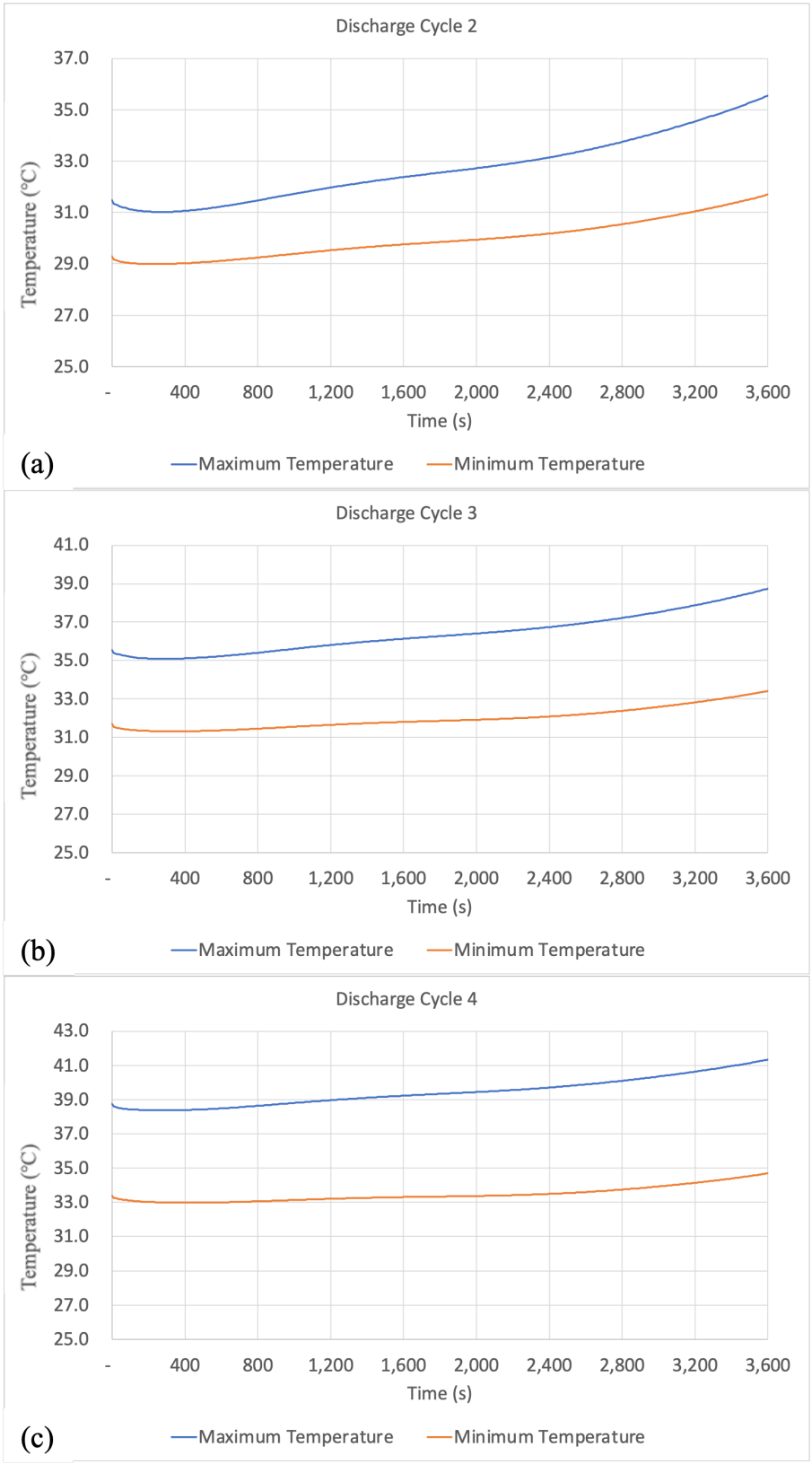

Figure 4.17: Maximum and minimum temperature profiles for (a) Discharge Cycle 2, (b) Discharge Cycle 3, and (c) Discharge Cycle 4.

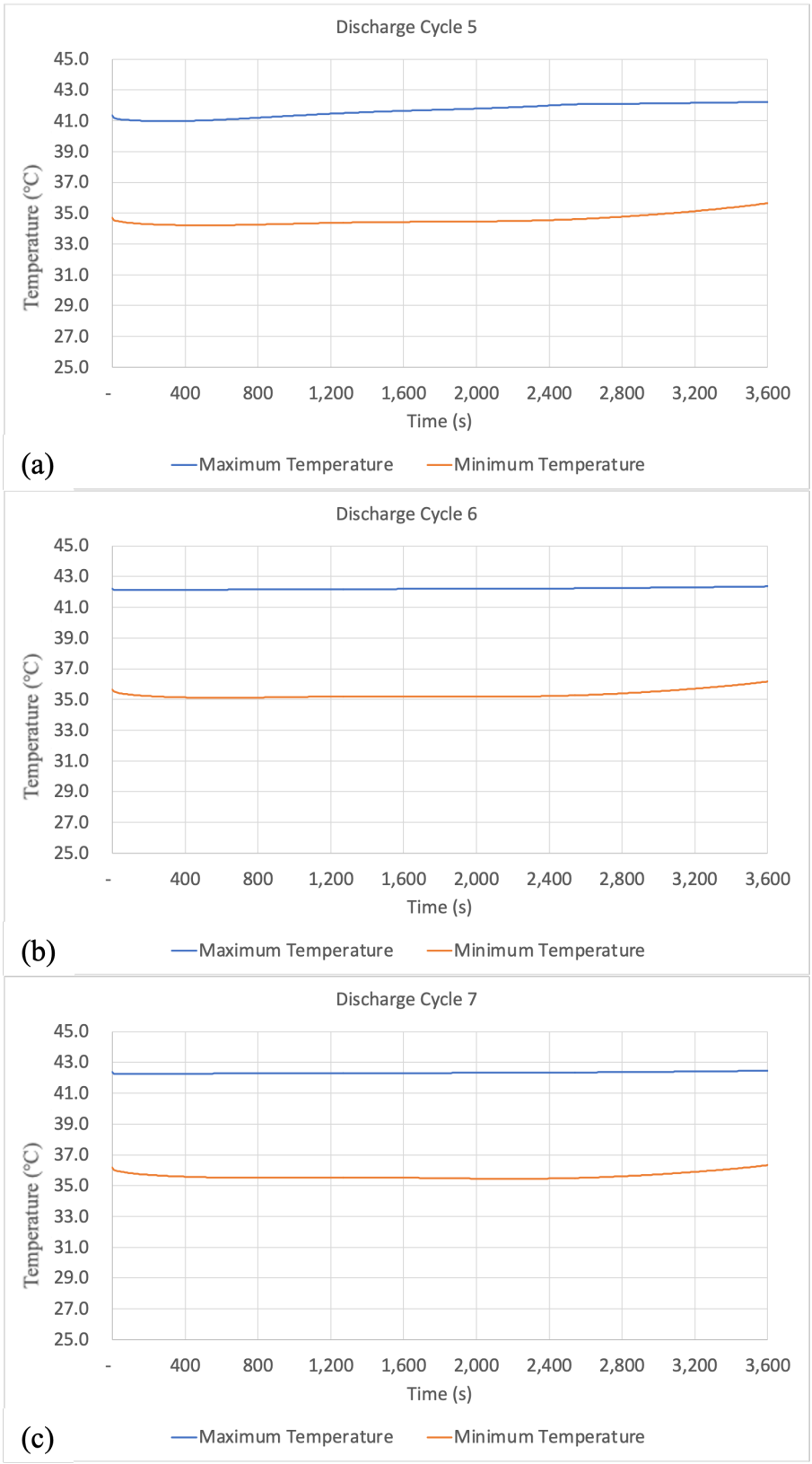

Figure 4.18: Maximum and minimum temperature profiles for (a) Discharge Cycle 5, (b) Discharge Cycle 6, and (c) Discharge Cycle 7.

The temperature contours of all the cells at the end of the discharge cycle are shown in Figure 4.19. The cooling phenomenon is the same as discussed in the previous section, with the top of the cells in contact with the top plate of the module housing exhibiting lower temperatures due to air cooling through the air duct. The difference starting from discharge Cycle 3 and through all the subsequent cycles can be seen in the cell surfaces that are facing the center cell in the module. The temperature on the surface towards the center of the battery module is lower as compared to surfaces facing the module housing. This is due to the additional cooling effect that is achieved through liquid cooling. Since some of the heat from the PCM is extracted using the water in the liquid channels, which is then expelled into the airflow, the PCM regains its heat extracting capability and extracts more heat from these surfaces. Whereas there is no additional cooling in the surface area that is exposed to the module housing. This can also be seen in Figure 4.20 in which the temperature contours of the PCM are shown at the end of discharge cycles. The temperature of the PCM in between the cells and the module housing keeps on increasing in each subsequent discharge cycle, whereas the temperature of the PCM in the center around the liquid channels is relatively low.

It can also be seen from Figure 4.20 that the temperature of water in the first column of liquid channels is low when compared to the second column of liquid channels. The airflow extracts heat from the first columns, and then once it reaches the second columns, it has less capacity for heat extraction resulting in a relatively higher temperature of water in the second columns. Since there is a lower temperature of the water, it extracts more heat from the surrounding PCM, so the temperature of the PCM is lower in this area and higher in the area of the second column of liquid channels.

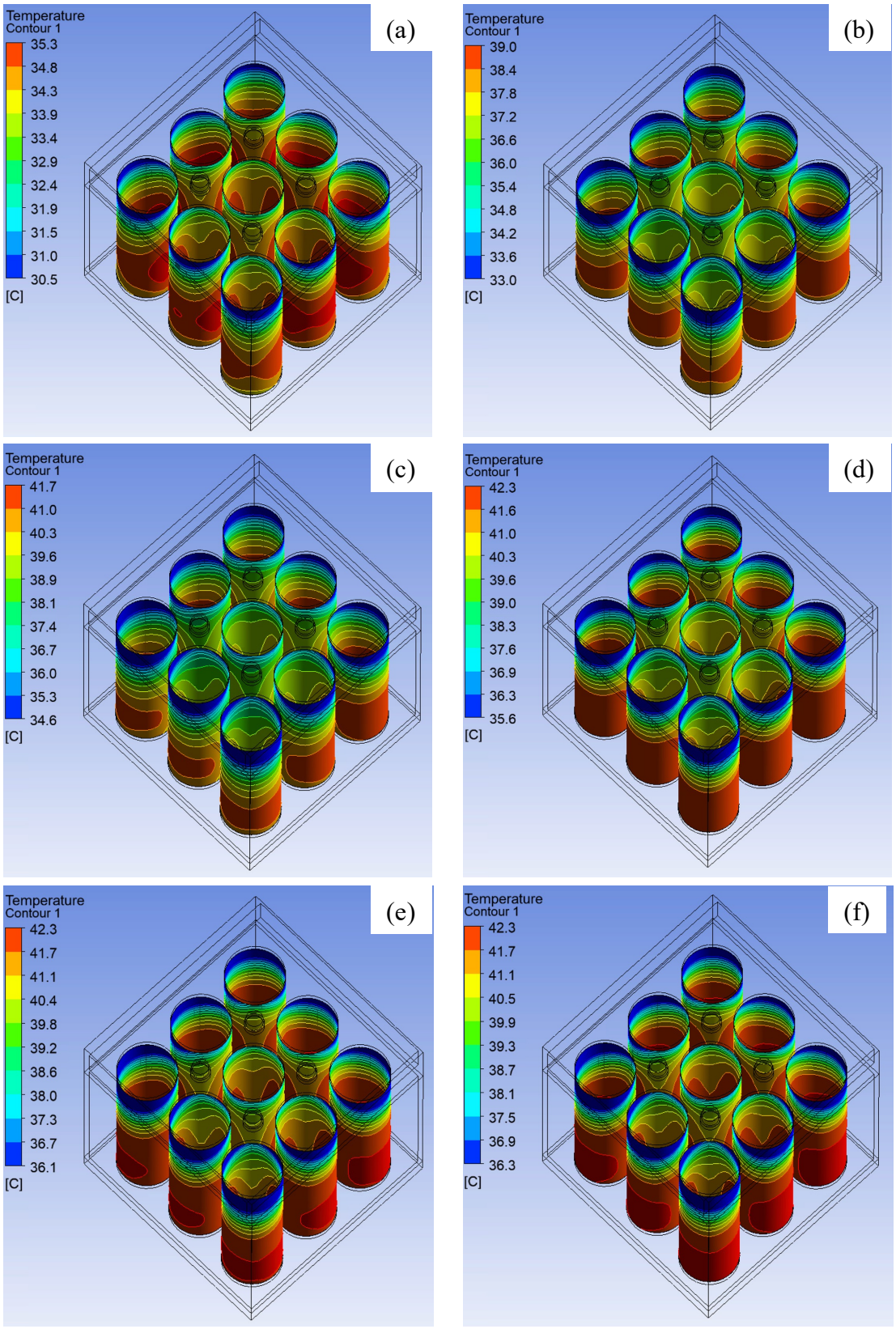

Figure 4.19: Temperature contours of cells at the end of (a) Discharge Cycle 2, (b) Discharge Cycle 3, (c) Discharge Cycle 4, (d) Discharge Cycle 5, (e) Discharge Cycle 6, and (f) Discharge Cycle 7.

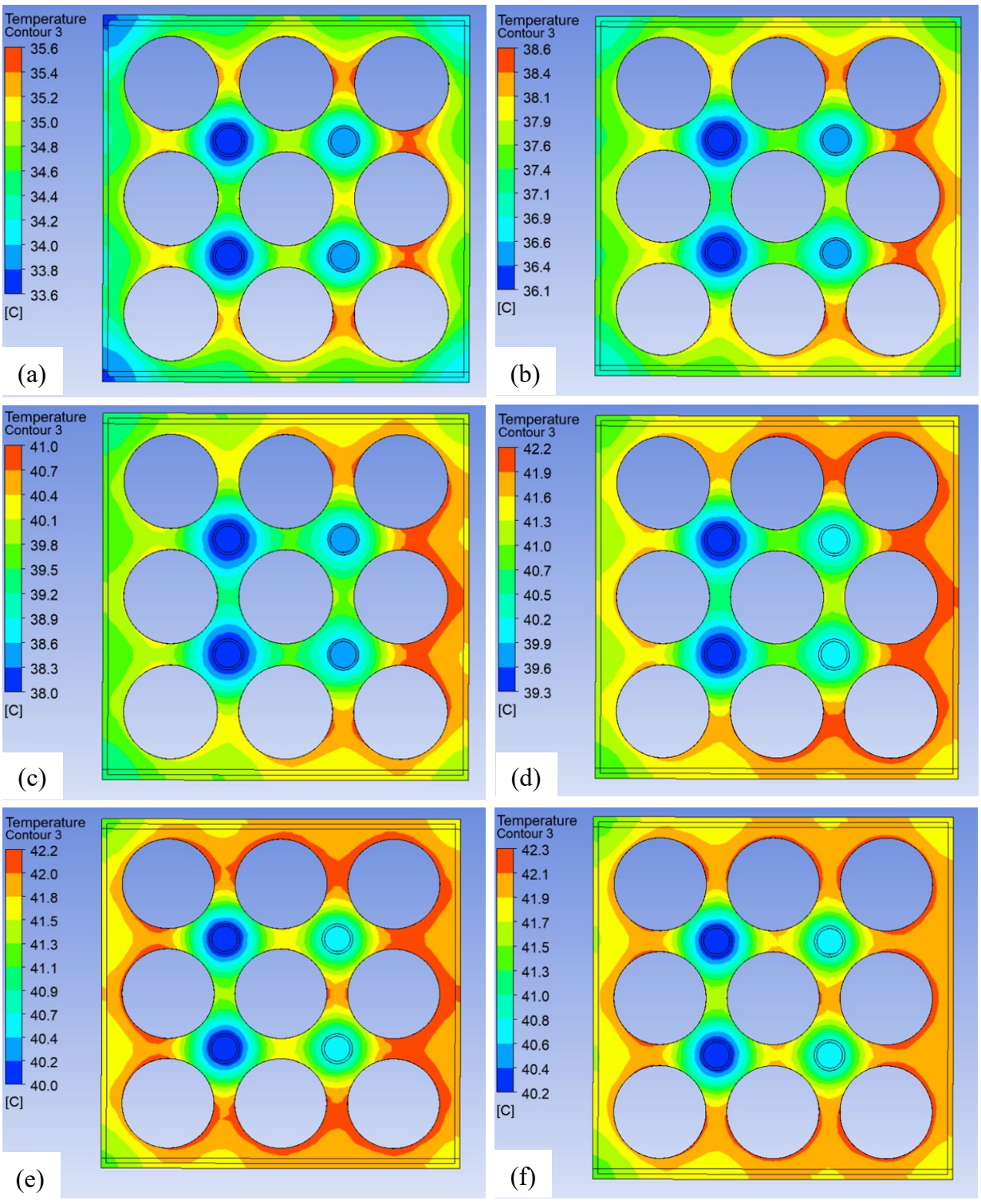

Figure 4.20: Temperature contours of PCM at the mid-plane of battery module at the end of (a) Discharge Cycle 2, (b) Discharge Cycle 3, (c) Discharge Cycle 4, (d) Discharge Cycle 5, (e) Discharge Cycle 6, and (f) Discharge Cycle 7.

4.5.4. PCM Melting Analysis

Since the temperature of the PCM reaches its phase change temperature in the fifth discharge, therefore, the amount of PCM that changes phase in discharge Cycles 5, 6, and 7 are shown in Figure 4.21. In discharge Cycle 5 the phase change starts to occur at approximately 1,800 s, and 0.3% of the PCM changed phase. In discharge Cycle 6, the phase change of the PCM continues as the heat from the cell is transferred to the PCM, and during this cycle additional 1% of PCM changes its phase. Similarly, in Cycle 7, additional 1% of PCM changes its phase. This shows that PCM utilization is low, which results in increased availability of PCM for the subsequent charge-discharge cycles, as stated earlier.

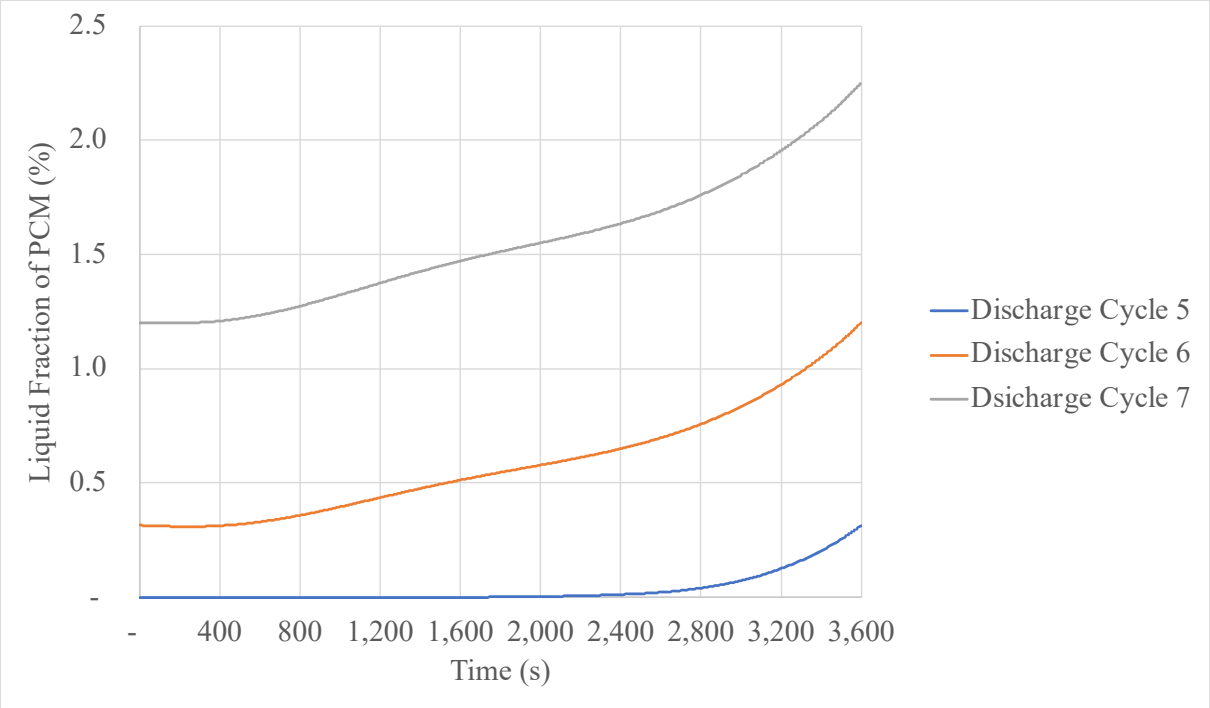

Figure 4.21: Liquid fraction of PCM in discharge Cycle 5, 6, and 7.

4.6. Analysis of Strategy 1 at Different Battery Module Discharge Rates

4.6.1. Heat Flux Profile at Various Discharge Rates

The heat flux profile of the 18650 Li-ion cell was obtained through Experiment 2, as described in Section 3.3.1. The cell was discharged at 1 C (2.5 A), 2 C (5 A), 3 C (7.5 A), 5 C (12.5 A), and 7 C (17.5 A) discharge rates. The results of the experiment are provided in Figure 4.22. It can be seen that in all the discharge rates, the initial increase in the heat flux is high and then the rate of heat flux reduces. Since there is more discharge time for 1 C, 2 C, and 3 C therefore, the rate of heat flux increases again. However, the discharge time for 5 C and 7 C is not enough for the rate of heat flux to increase again. The maximum heat flux obtained at the end of the discharge cycle at 1 C is 170 W/m^2; at 2 C, it is 323 W/m^2; at 3 C, it is 382 W/m^2; at 5 C, it is 540 W/m^2; and at 7 C, it is 584 W/m^2. These heat flux profiles were used as the transient surface boundary condition for the numerical modeling.

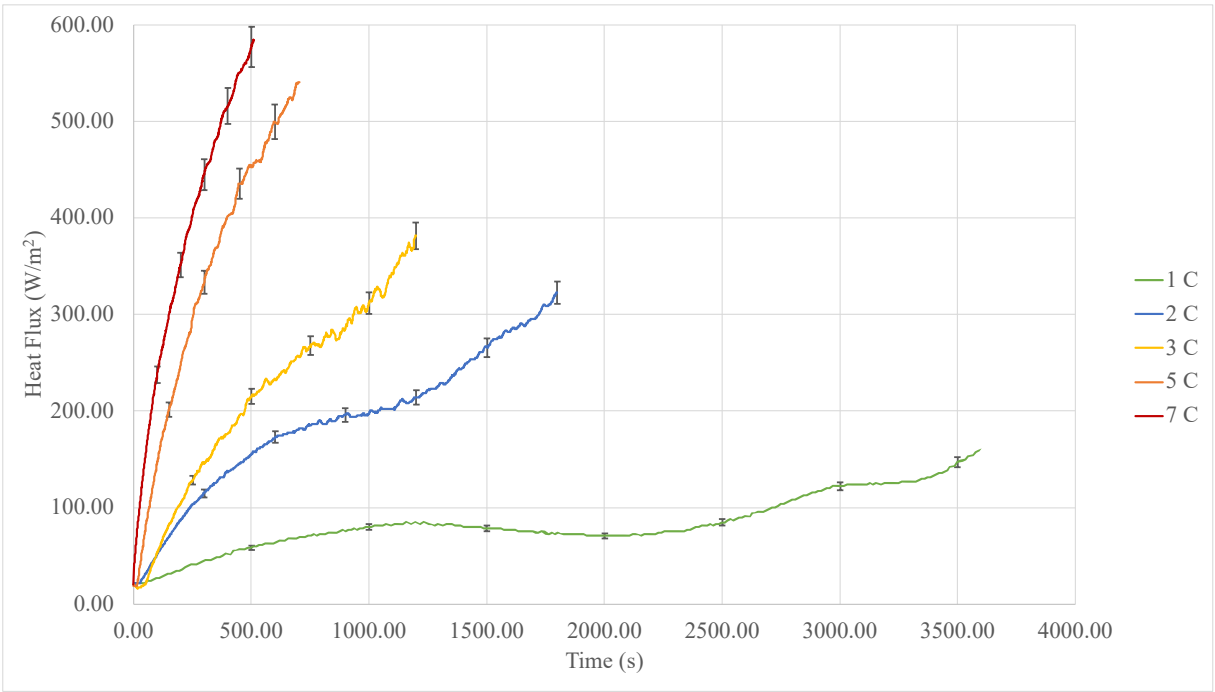

Figure 4.22: Transient heat flux at different discharge rates.

4.6.2. Thermal Analysis at Various Discharge Rates

The developed and validated numerical model was used to conduct numerical simulations at different discharge rates. The feasible operating temperature range for the Li-ion cells is from 20 – 40 °C, and a tolerable range for the operation ranges from 40 – 50 °C. Additionally, the temperature difference between the maximum and the minimum temperature (also referred to as temperature uniformity) should be maintained within 5 °C. The maximum and minimum temperatures and temperature uniformity for all the discharge rates are shown in Figure 4.23.

It can be seen from Figure 4.23 (a) that at 1 C discharge rate, the maximum temperature increase throughout the discharge cycle is up to 29.4 °C by the end of discharge. The phase change of the PCM starts at 30 °C (Table 3.2), and in this case, no phase change occurs since the temperature does not reach the phase change temperature of the PCM. At the 2 C discharge rate, the maximum temperature increases up to 30 °C at 1,390 s. At this point, the phase change of the PCM starts, and the maximum temperature increases to 30.3 °C by the end of the discharge rate. Any heat generated beyond 1,390 s is extracted through the latent heat of the PCM, which maintains the maximum temperature at ~30 °C. Similarly, the maximum temperature reaches 30 °C for 3 C at 985 s, 5 C at 520 s, and 7 C at 405 s. There is no further increase as the maximum temperature is limited by the phase change temperature of the PCM. At higher discharge rates, the maximum temperature reaches ~30 °C quicker due to increased heat generation from the cell, however, the time it stays at this temperature reduces with increasing discharge rates. At 2 C, it stays at ~30 °C for 410 s, at 3 C for 215 s, at 5 C for 200 s, and at 7 C for 109 s. In terms of percentage, at 2 C the maximum temperature stays at ~30 °C for 22.8%, at 3 C for 17.9%, at 5 C for 27.8%, and at 7 C for 21.2% of the total discharge time. The longer it takes for the maximum temperature to reach

the phase change temperature and the least it stays at this temperature until the completion of discharge is beneficial for the BTMS as this will result in the lowest utilization of the PCM.

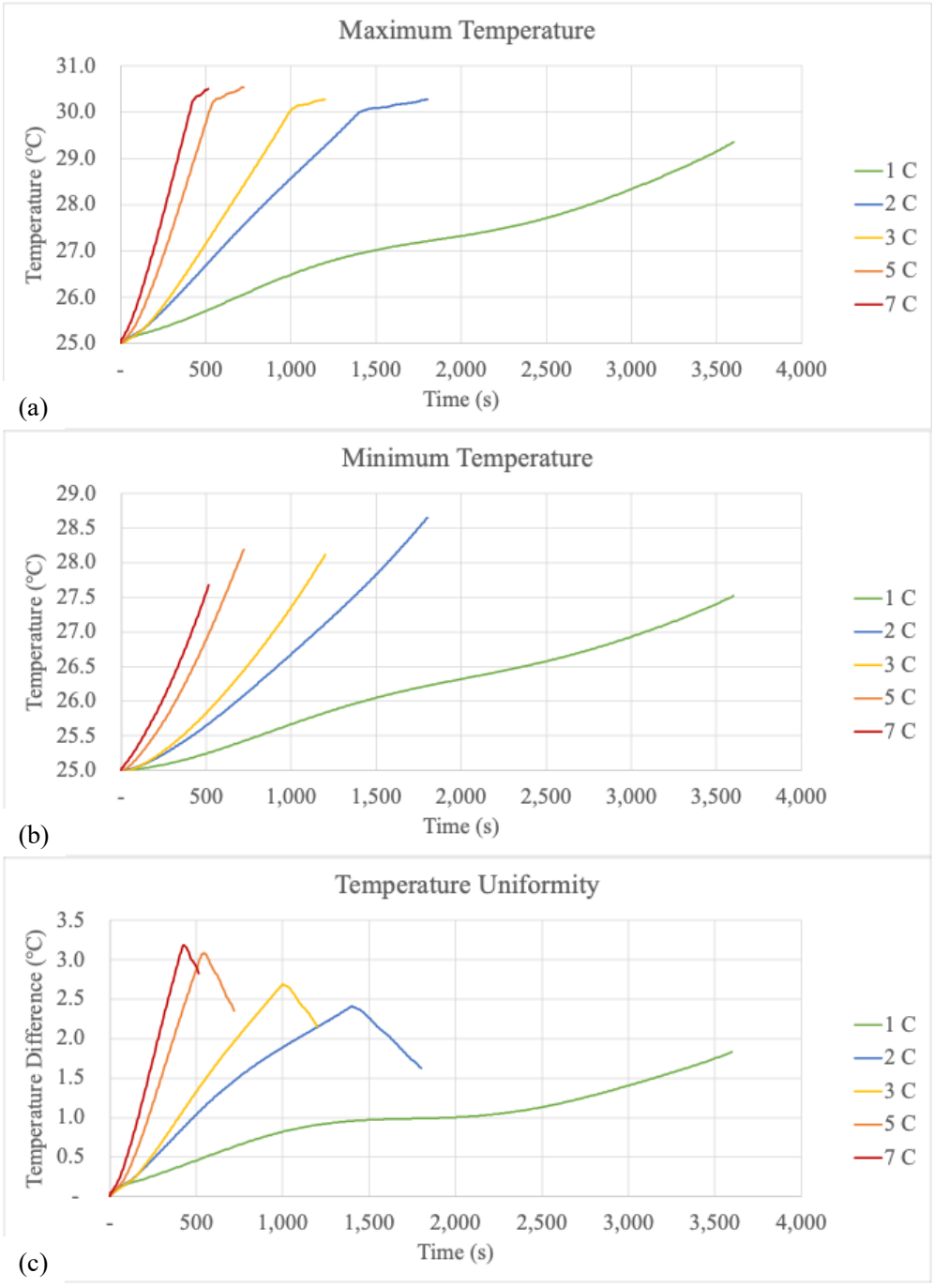

Figure 4.23: (a) Maximum temperature, (b) minimum temperature, and (c) temperature uniformity for all the discharge rates.

It can be seen from Figure 4.23 (b) that in all the discharge rates, the minimum temperature of the battery module does not reach the phase change temperature. It increases throughout the discharge, and at the end of discharge at 1 C, it reached 27.5 °C; at 2 C, it reached 28.6 °C; at 3 C, it reached 28.1 °C; at 5 C, it reached 28.2 °C, and at 7 C it reached 27.7 °C. The maximum temperature increases at a higher rate compared to the increase in the minimum temperature. This difference in temperature increase rates results in a temperature non-uniformity in the battery module.

It can be seen from in Figure 4.23 (c) that the temperature uniformity generally reduces with increasing discharge rate as expected. At 1 C discharge rate, the temperature difference keeps increasing throughout the discharge cycle and its 1.8 °C by the end of the discharge cycle. For all the other discharge rates, the temperature uniformity reduces until the phase change temperature of the PCM is reached, and then it increases until the end of the discharge cycle. Once the phase change temperature is reached, the maximum temperature does not increase, whereas the minimum temperature keeps increasing. This reduces the temperature difference, which then increases the temperature uniformity.

The temperature contours of all the cells at the end of the discharge cycle are shown in Figure 4.24. It can be seen that the high temperature locations are at the center of the cells, specifically the surfaces facing the neighboring cells. Whereas the surfaces facing the housing of the battery module have lower temperatures. Moreover, the surfaces of the cells that are in direct contact with the top and bottom plate of the battery module have relatively lower temperatures due to heat conduction from the cell to the module housing. Compared to the surface in contact with the bottom plate, the surface of the cell in contact with the top plate exhibits the minimum temperatures

due to the air-cooling effect that occurs at the top plate. Therefore, the top plate cools due to air cooling, and then this allows additional conduction from the cell surface to the top plate.

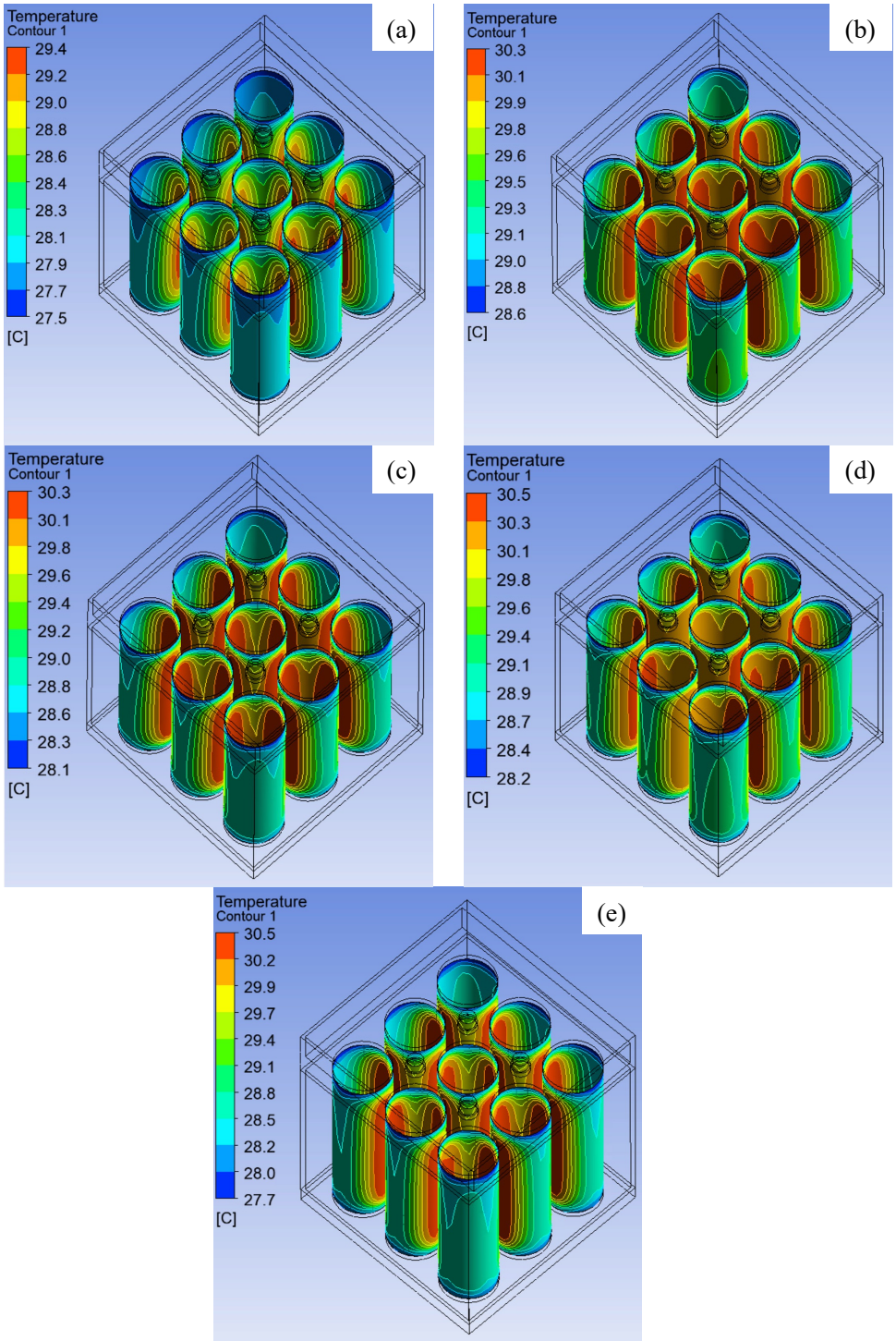

Figure 4.24: Temperature contours at the end of the discharge cycle for (a) 1 C, (b) 2 C, (c) 3 C, (d) 5 C, and (e) 7 C discharge rates.

Moreover, the compound heating effect between the cells can be visualized in Figure 4.25. The temperature contours at the center of the battery module for all the different discharge rates are shown in Figure 4.25. Since the contours are extracted at the end of the discharge cycle, therefore, they are similar. The highest temperature of the PCM is exhibited at the contact surface with the cells. The PCM that is in between the surfaces of the two neighboring cells has higher temperatures compared to the rest of the PCM. The effect of the liquid channel can also be seen in Figure 4.25. The fluid in the liquid channel acts as a heat sink for the PCM, which reduces the temperature of the PCM around the liquid channels. Additionally, the battery module housing also acts as a heat sink for the PCM, and the PCM near the housing of the battery module has the lowest temperatures. The housing is being cooled by the ambient temperature and the airflow within the air duct, which results in the lowest temperatures of the PCM.

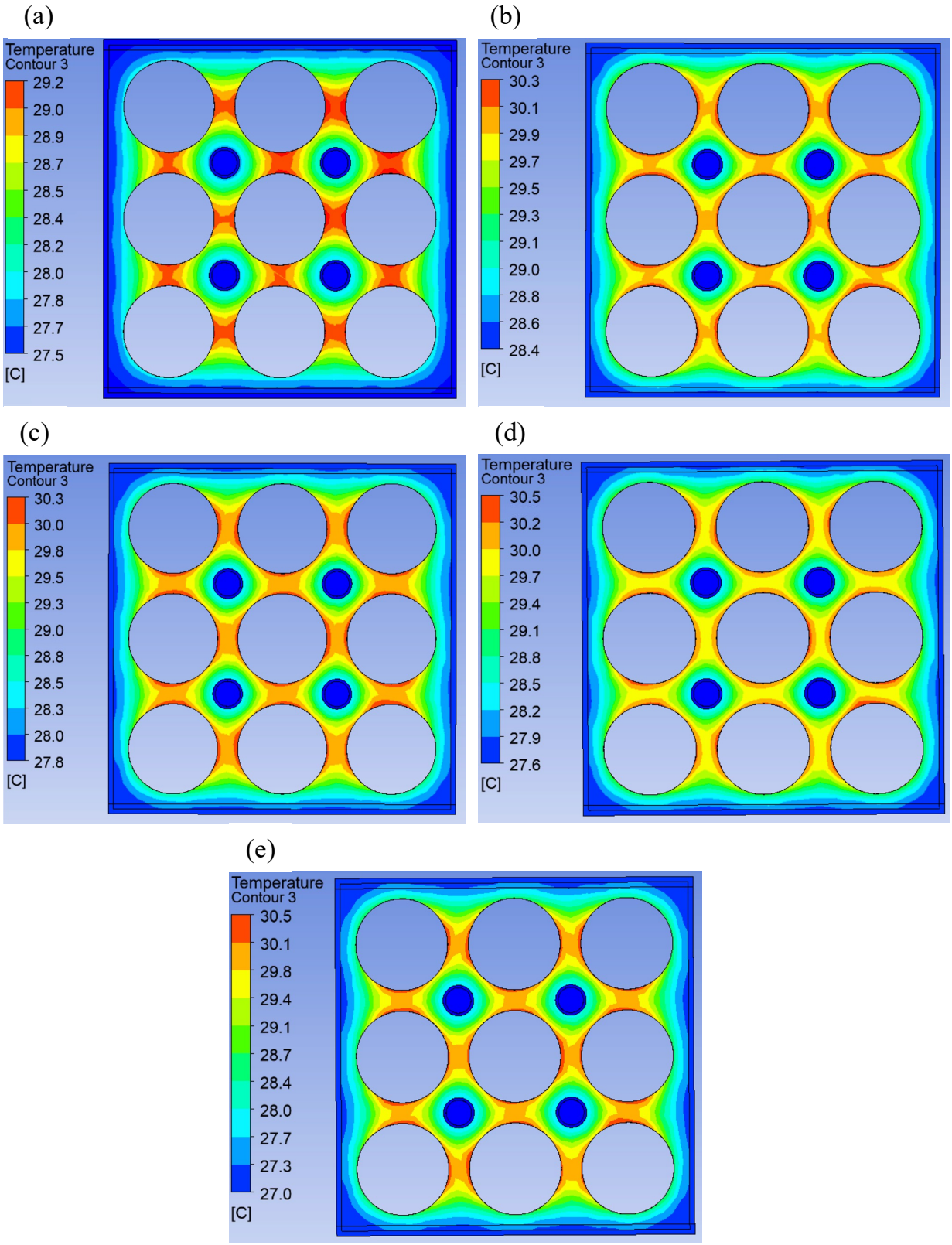

Figure 4.25: Temperature contours at the center of the battery module at the end of the discharge cycle for (a) 1 C, (b) 2 C, (c) 3 C, (d) 5 C, and (e) 7 C discharge rates.

4.6.3. PCM Melting Analysis

As discussed previously, the secondary coolants, which are water in liquid channels and airflow within the air duct, have assisted in removing heat from the PCM, resulting in an increase in its heat extraction capacity. However, it is necessary to study the amount of PCM that has melted in the discharge process. At 1 C, none of the PCM was utilized as the maximum temperature was below the phase change temperature of the PCM. At 2 C, the PCM utilization was 0.32%; at 3 C, it was 0.14%; at 5 C, it was 0.3%; and at 7 C, it was 0.12%. This shows that due to the secondary cooling, the amount of PCM that changes phase is low, and it is capable of extracting additional heat energy from the cells. The initial intuition is that the PCM utilization should be monotonic and as the discharge rate increases the PCM utilization should increase as well. However, this is not always the case as shown through this study. The PCM utilization is dependent on the discharge rate, the time interval percentage of maximum temperature at the phase change temperature, and the amount of heat flux increase during interval as shown in Table 4.3. It be seen that the highest PCM utilization is at 2 C which has the highest increase in the heat flux of 89.76 W/m^2 and the lowest utilization is at 7 C which has the lowest heat flux increase of 68.22 W/m^2 during the interval.

Table 4.3: PCM utilization summary.

Discharge Rate	Time Interval of Maximum Temperature at ~30°C (s)	Heat Flux Increase During Interval (W/m2)	PCM Utilization (%)
1 C	0 (0.0%)	-	0.00
2 C	410 (22.8%)	89.76	0.32
3 C	215 (17.9%)	76.97	0.14
5 C	200 (27.8%)	85.58	0.30
7 C	109 (21.2%)	68.22	0.12

4.7. Development of Strategy 2 and Comparison with Strategy 1

4.7.1. Overview of Thermal Profiles of the Proposed Strategies

The developed and validated numerical model was used to conduct numerical simulations. The maximum and minimum temperatures for BM3-C1, BM4-C1, and BM4-C2 are shown in Figure 4.26.

For BM3-C1 it can be seen from Figure 4.26 (a) that the maximum temperature increase reaches 30 °C, which is the phase change temperature of the PCM by 405 s. At this point, the phase change of the PCM starts, and the maximum temperature increases to 30.5 °C by the end of the discharge rate at 514 s. Any heat generated beyond 405 s is extracted through the latent heat of the PCM, which maintains the maximum temperature at ~30 °C. For BM4-C1, the maximum curve is similar to BM3-C1, as shown in Figure 4.26 (b). In this as well, the maximum temperature reaches 30 °C by 405 s. For both these strategies, in terms of percentage, the maximum temperature stays at ~30 °C for 21.2% of the total discharge time. Additionally, it can be seen from Figure 4.26 (c) for BM4-C2 that the maximum temperature increase throughout the discharge cycle is up to 29.1 °C by the end of discharge. The phase change of the PCM starts at 30 °C, and in this case, no phase change occurs since the temperature does not reach the phase change temperature of the PCM. The longer it takes for the maximum temperature to reach the phase change temperature and the least it stays at this temperature until the completion of discharge is beneficial for the BTMS as this will result in the lowest utilization of the PCM.

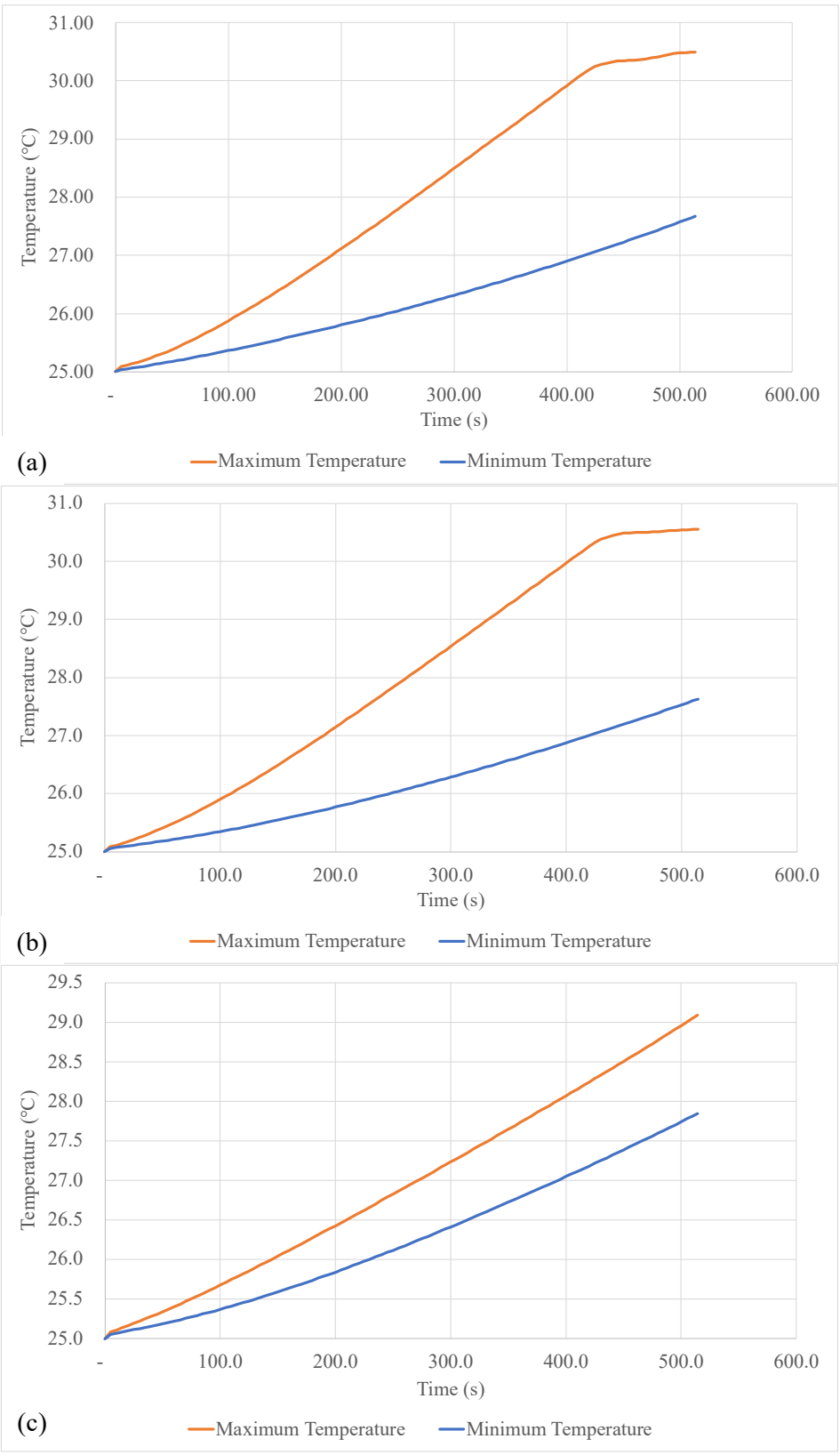

Figure 4.26: Maximum and minimum temperature for (a) BM3-C1, (b) BM4-C1, and (c) BM4-C2.

It can be seen from Figure 4.26 that in all strategies, the minimum temperature of the battery module does not reach the phase change temperature. It increases throughout the discharge, and at the end of discharge, it reaches 27.7 °C. The maximum temperature increases at a higher rate compared to the increase in the minimum temperature. This difference in temperature increase rates results in a temperature non-uniformity in the battery module and is shown in Figure 4.27.

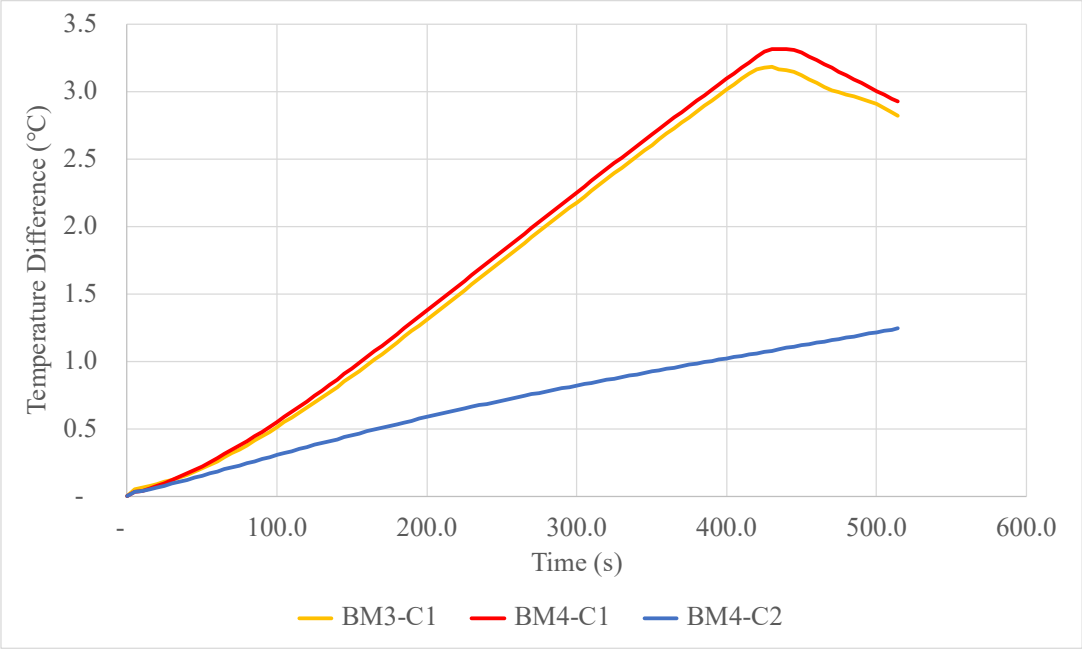

Figure 4.27: Temperature difference between the maximum and minimum temperature for BM3-C1, BM4-C1, and BM4-C2.

It can be seen from Figure 4.27 that the temperature uniformity (difference between the maximum and minimum temperature) generally reduces with increasing discharge time. In BM3-C1 and BM4-C1, the rate of maximum temperature compared to the rate of minimum temperature increases; therefore, the temperature uniformity reduces at a higher rate until the phase change temperature of the PCM is reached, and then it starts to increase until the end of the discharge cycle. Once the phase change temperature is reached, the maximum temperature does not increase, whereas the minimum temperature keeps increasing. This reduces the temperature difference,

which then increases the temperature uniformity. For BM4-C2, due to effective cooling from the cold plates, the rate of maximum temperature increase is significantly lower; therefore, the decrease in temperature uniformity throughout the discharge cycle is significantly lower.

In order to better understand the cooling phenomenon, the temperature contours of all the cells at the end of the discharge cycle are shown in Figure 4.28. In all the strategies, it can be seen that the surfaces of the cells that are in direct contact with the top and bottom plate of the battery module have relatively lower temperatures due to heat conduction from the cell to the module housing. Compared to the surface in contact with the bottom plate, the surface of the cell in contact with the top plate exhibits the minimum temperatures due to the air-cooling effect that occurs at the top plate. Therefore, the top plate cools due to air cooling, and then this allows additional conduction from the cells' surface to the top plate. For BM3-C1 and BM4-C1, it can be seen that the high temperature locations are at the center of the cells, specifically the surfaces facing the neighboring cells. Whereas the surfaces facing the housing of the battery module have lower temperatures. For BM4-C2, even lower temperature surfaces are the surfaces that are directly facing the cold plates. This shows the effectiveness of the cold plate utilization as it extracts a higher amount of heat from the PCM material, which increases the heat extraction capacity of the PCM, resulting in increased cooling from the surface of the cells. Finally, for BM4-C2, due to the presence of cold plates in between all the surfaces of the neighboring cells, the highest amount of cooling is achieved compared to the other two strategies. The lower temperature surfaces are the ones that are in front of the cold plates, whereas the higher temperature surfaces are the ones that are facing the module housing. Since the module housing is cooled through the ambient temperature and the airflow at the top of the battery module only as compared to the liquid cooling effect for the other cell

surfaces therefore, these temperatures are higher in comparison. This shows the effectiveness and importance of the presence of liquid cooling within the proposed battery module.

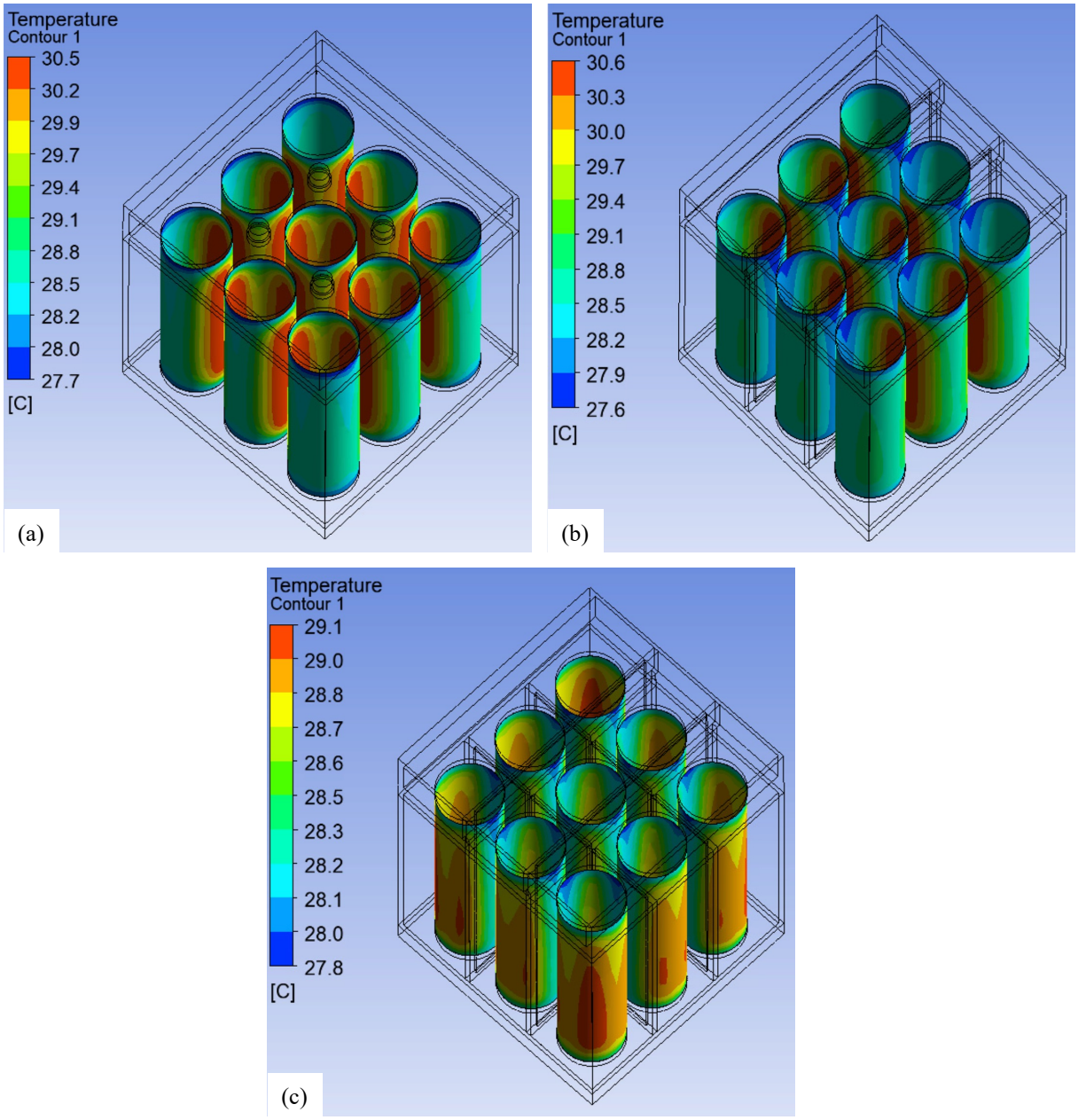

Figure 4.28: Temperature contours at the end of the discharge cycle for (a) BM3-C1, (b) BM4-C1, and (c) BM4-C2.

4.7.2. Effects of Secondary Liquid and Air Cooling

In order to better visualize the effect of liquid cooling, the temperature contours at the center of the battery module towards the end of the discharge cycle are provided in Figure 4.29. In all the strategies, the highest temperature of the PCM is exhibited at the contact surface with the cells. For BM3-C1 and BM4-C1, the PCM that is in between the surfaces of the two neighboring cells has higher temperatures compared to the rest of the PCM. In BM3-C1, the fluid in the liquid channel acts as a heat sink for the PCM, which reduces the temperature of the PCM around the liquid channels. Additionally, the battery module housing also acts as a heat sink for the PCM, and the PCM near the housing of the battery module has the lowest temperatures. The housing is cooled by the ambient temperature and the airflow within the air duct. Moreover, the cold plates also act as a heat sink for the PCM, and the effect of cold plates can be seen in BM4-C1 and BM4-C2. In BM4-C1, through the addition of a cold plate, the high temperature region with the PCM in the transverse direction is eliminated as all the fluid extracts the heat from the PCM. Similarly, through the placement of additional cold plates in the longitudinal direction, the high temperature regions between all the neighboring cells have been eliminated in BM4-C2. In BM3-C1 and BM4-C1, the high temperature regions in between the cells are the cause of the high temperature increase rate and increased temperature uniformity, as shown in Figure 4.26 (a), (b), and Figure 4.27. As a result, the melting of the PCM starts in these regions. However, in BM4-C2 these high temperature regions are eliminated; therefore, the temperature does not reach the phase change temperature of the PCM, and the melting of the PCM does not occur.

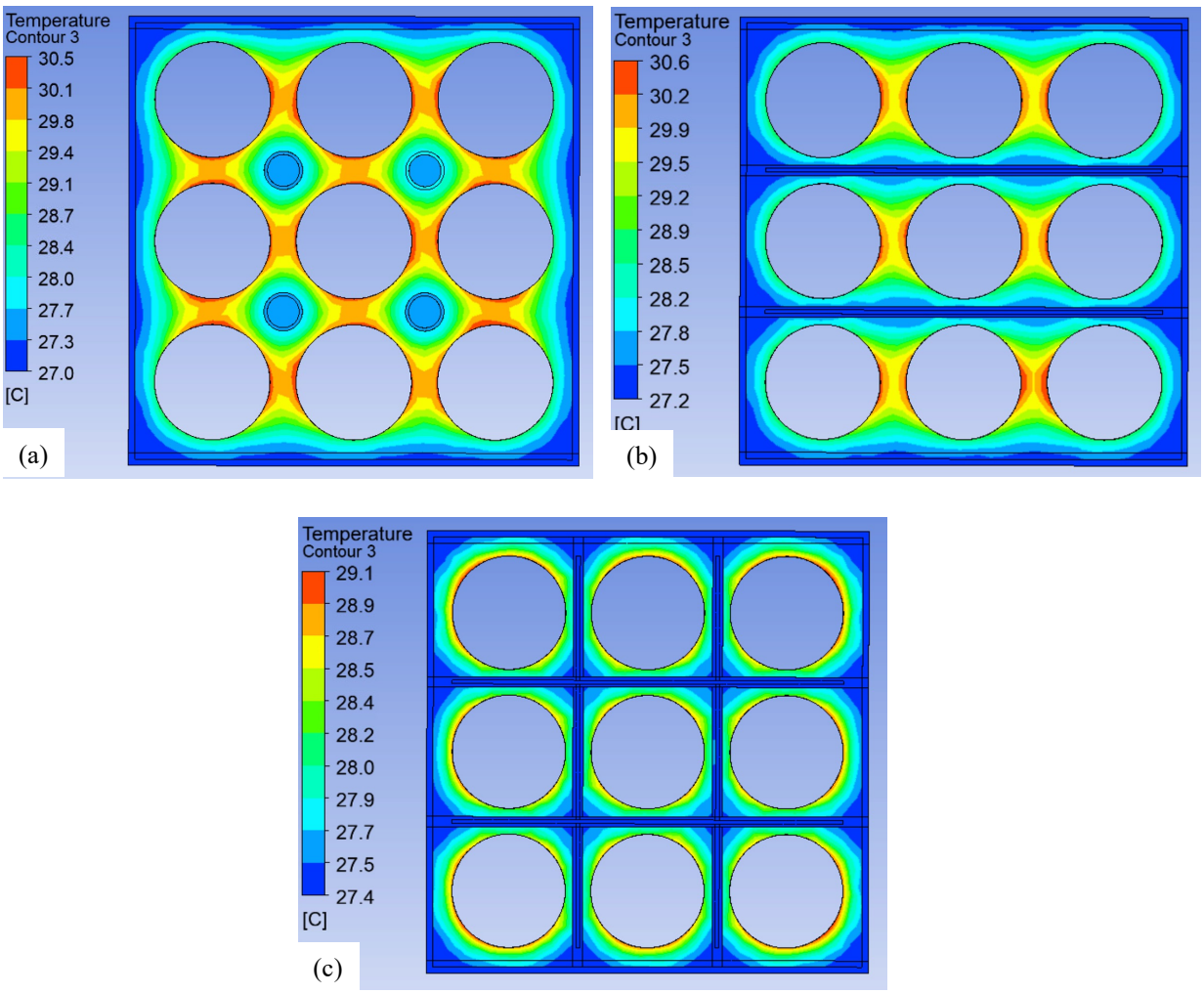

Figure 4.29: Temperature contours at the center of the battery module at the end of the discharge cycle for (a) BM3-C1, (b) BM4-C1, and (c) BM4-C2.

The temperature contours for the liquid channels and cold plates are provided in Figure 4.30. It can be seen that in BM3-C1, due to the minimal contact surface between the liquid channel and the PCM, the heat extraction from the PCM is lowest. Whereas, in BM4-C1, there is an increased heat extraction through the increased contact surface area. Finally, the highest heat extraction is achieved in BM4-C2 as it has the highest contact surface area with the PCM. Moreover, for BM4-C1 and BM4-C2, the lower portion of the fluid has the highest temperature, and it gradually reduces to the minimum towards the top portion of the fluid. This is due to the air-cooling effect that occurs at the top of the cold plates that is protruded within the air duct. Additionally, the lowest

temperature of the fluid is exhibited near the inlet of the air duct and as the air flows through the cold plate, its heat extraction capacity reduces, and the temperature of the fluid increases towards the outlet of the air duct. The impact of the single fluid body in BM4-C2 can be seen in Figure 4.30 (c), as the same airflow allows the fluid to cool in between the cell columns as well.

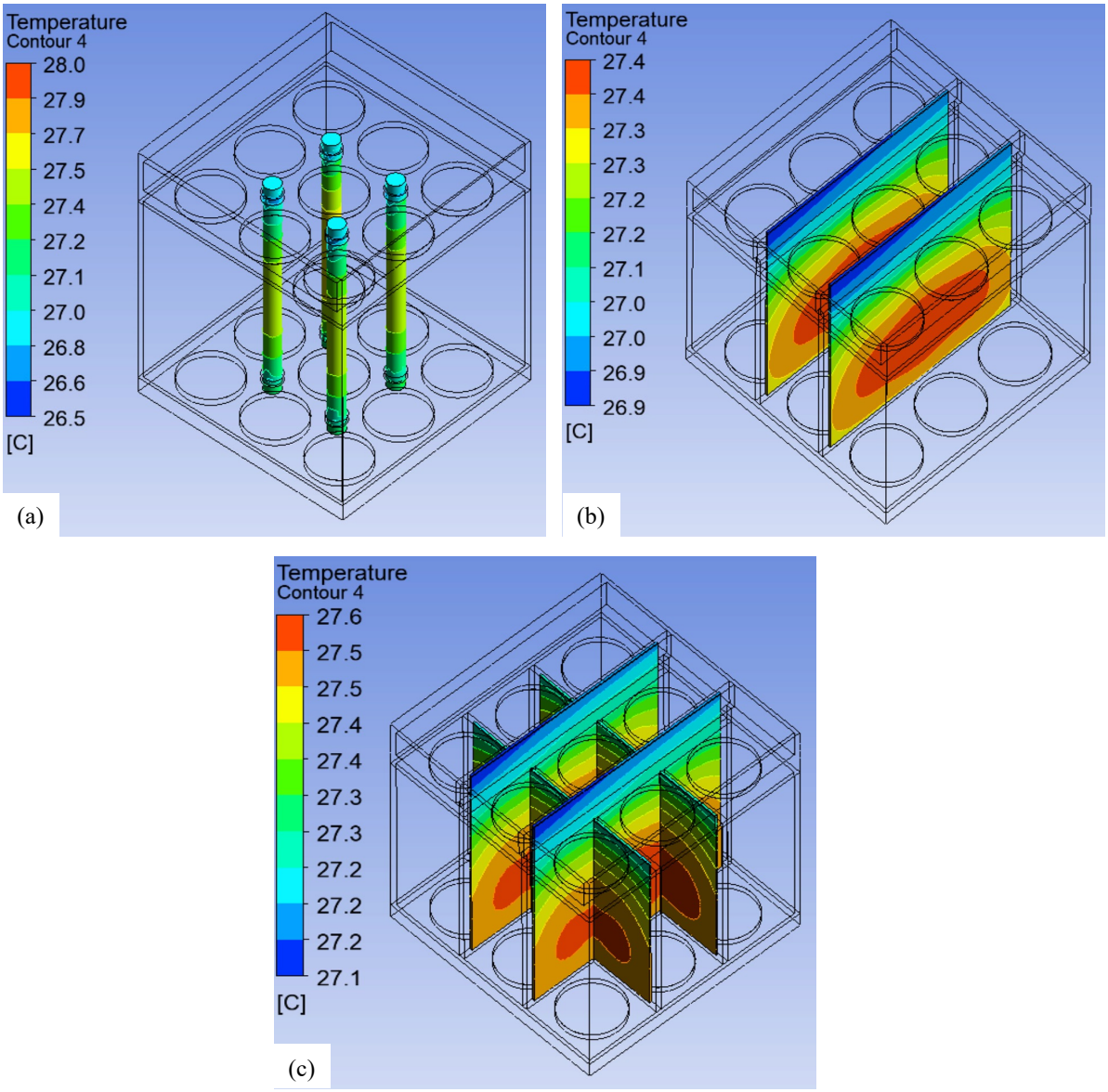

Figure 4.30: Temperature contours of (a) liquid channel in BM3-C1, and (b) cold plates for BM4-C1, and (c) BM4-C2.

Since the airflow has a low velocity with a Reynold number of 1,950 therefore, the temperature of airflow near the walls of the battery module and the cold plates will be the highest as compared to airflow in the center of the air duct. Hence, the temperature contours of airflow at the walls are shown in Figure 4.31. In all the strategies, the temperature of airflow near the inlet is the lowest, and it increases as it extracts heat and moves toward the outlet of the battery module. It can be seen that the lowest heat transfer to airflow occurs in BM3-C1, and the heat transfer increases slightly by 1.1% as it flows over the liquid channels. Whereas, in BM4-C1, the heat transfer is high as it flows over the cold plates because of the increased contact surface area with the protruding cold plates in the air duct. Finally, in BM4-C2, there is increased heat accumulation in the cold plates resulting in higher heat extraction from the airflow and the highest cooling achieved.

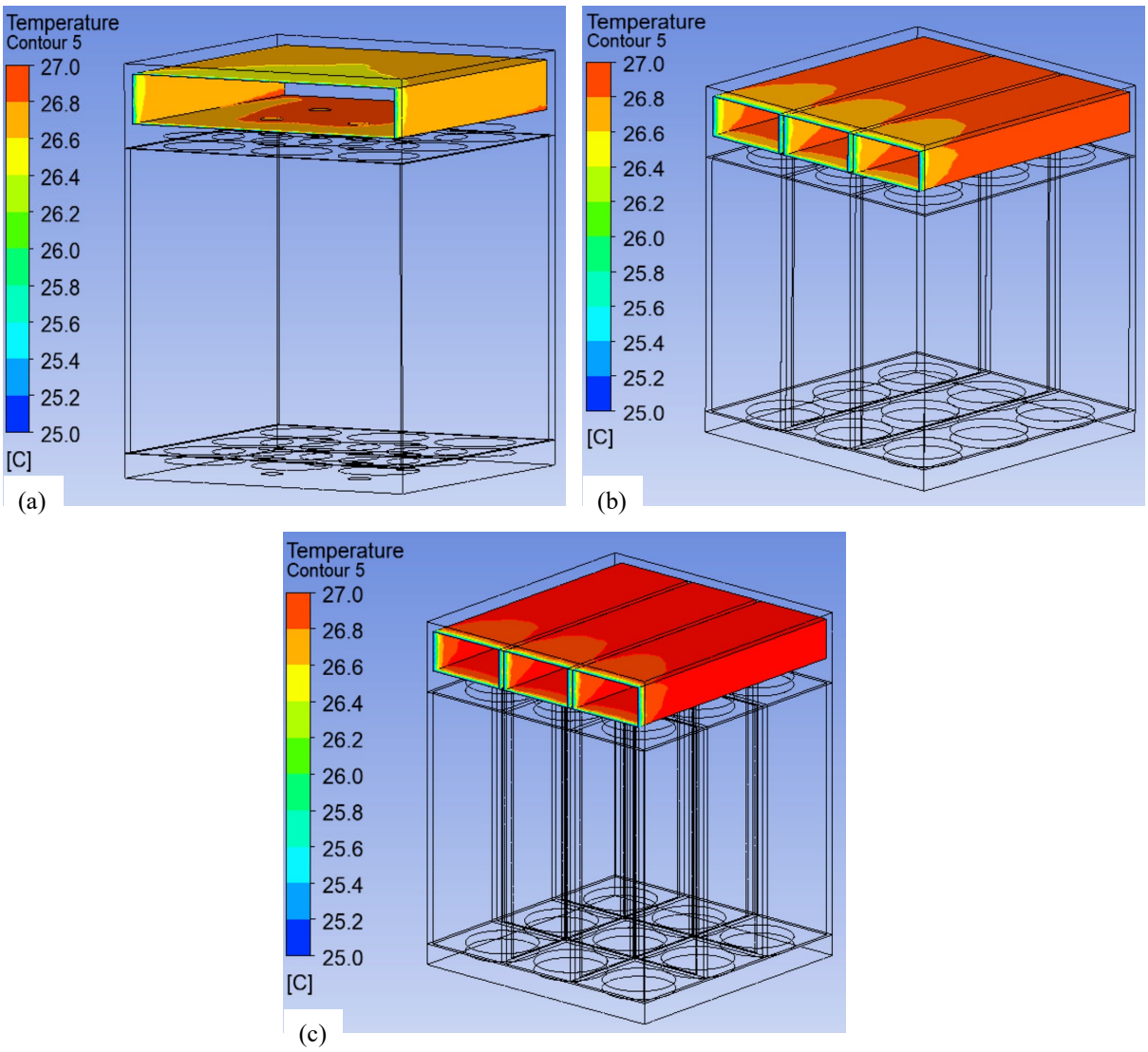

Figure 4.31: Temperature contours of air contact surfaces in (a) BM3-C1, (b) BM4-C1, and (c) BM4-C2.

4.7.3. PCM Melting Analysis

In BM3-C1, due to low heat extraction from the circular liquid channels, the highest amount of PCM melting occurred at 0.12%. This is followed by BM4-C1 with a PCM melting of 0.07%, and finally, due to exceptional cooling from the secondary coolants, none of the PCM was melted in BM4-C2. Overall, the melting amount of PCM is very low, even at a high discharge rate of 7 C. This shows that due to the secondary cooling, the amount of PCM that changes phase is low, and it is capable of extracting additional heat energy from the cells.

4.8. Analysis on the Impact of Ambient Temperature on Strategy 2

Since Strategy 2 exhibits better thermal performance compared to Strategy 1 therefore, it was used to analyze the effects of different ambient temperatures. The ambient temperature was changed from 25 °C to 40 °C in increments of 5 °C. The maximum and minimum temperatures were obtained for all the different ambient temperatures. The result for 25 °C ambient temperature is already provided in Figure 4.26 (c), and the results for 30 °C, 35 °C, and 40 °C are provided in Figure 4.32. It is to be noted that the phase change temperature of PARAFFIN starts at 30 °C.

At 25 °C the heat from the surface of cells is extracted using the thermal conductivity of the PCM. This results in a maximum increase of only 4.1 °C from the ambient temperature of 25 °C due to the impact of secondary coolants. At an ambient of 30 °C the phase change of the PCM starts with the discharge of the cells, and it begins to melt. During this process, all the heat generated at 7 C discharge rate is extracted through the latent heat of the PCM. This results in the maximum temperature increase of 0.83 °C and the minimum temperature increase of 0.51 °C as shown in Figure 4.32 (a). Additionally, during the discharge process, 12.2% of the PCM changed it phase. This shows that due to the availability of the secondary coolants, a limited amount of PCM and the remaining PCM has additional capacity to extract heat from subsequent charge and discharge cycles. At ambient temperatures 35 °C and 40 °C, the PCM has completely changed its phase and is in liquid form at the beginning of the discharge cycle. Hence, the latent heat of the PCM cannot be further utilized, and only the thermal conductivity is used to extract heat from the surface of the cells and transfer it to the secondary coolants. Therefore, the results for 35 °C and 40 °C ambient temperature shows a similar curve to 25 °C ambient temperature and the maximum temperature increases by 4.1 °C. This shows that it is vital to use a PCM or a CPCM with increased thermal

conductivity, as outside the phase change temperatures, the thermal conductivity will be used to extract the heat from the cells. However, since the temperature increase is limited to 4.1 °C by the hybrid BTMS strategy, it can be used at 45 °C ambient temperature as well. At 45 °C ambient temperature, the maximum temperature will be limited to less than 50 °C, which is the high end of the tolerable temperature range of the Li-ion cell.

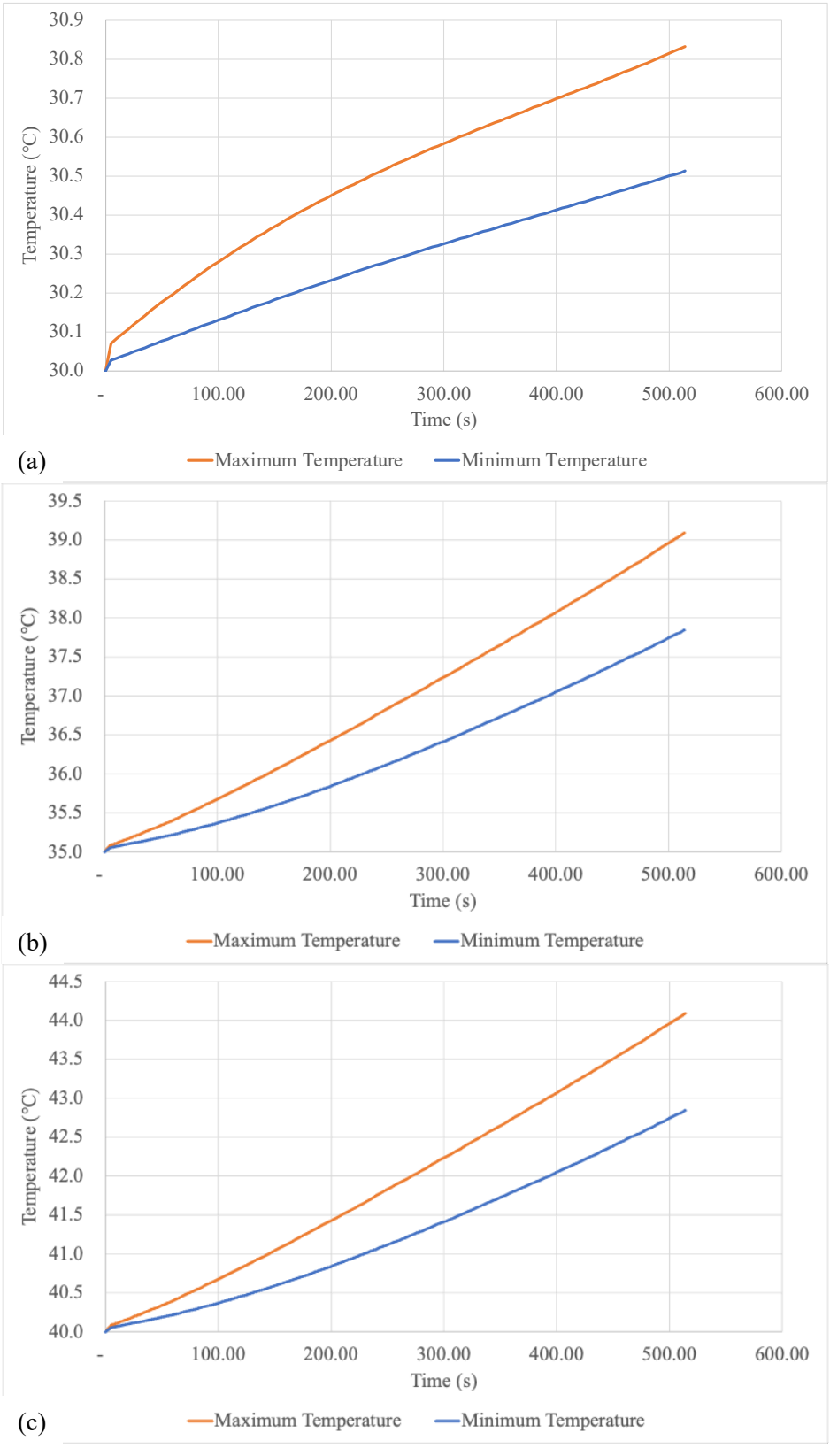

Figure 4.32: Maximum and minimum temperature for Strategy 2 at (a) 30 °C, (b) 35 °C, and (c) 40 °C ambient temperature.

4.9. Addition of Property Enhancing Materials to Paraffin based PCM in Strategy 2

The details of the selected CPCM are provided in Table 3.4. It can be seen that through the addition of various PEM to a paraffin base PCM the thermal conductivity can be increased, which results in improved cooling outside the phase change temperature regions of the PCM. The results for Strategy 2 with the selected CPCM are shown in Figure 4.33. Since the ambient temperature was 25 °C and due to the hybrid BTMS the maximum temperature of the cells remained below the phase change temperature of the PCM. Therefore, thermal conductivity is used to extract heat from the cells below the phase change temperature. It can be seen that the rate of maximum temperature increase for the CPCM increase with reducing thermal conductivity. The lowest thermal conductivity is of CPCM with expanded vermiculite which results in the highest maximum temperature of 28.2 °C at the end of the 7 C discharge rate.

Additionally, the maximum temperatures reduce with the subsequent PCM with higher thermal conductivities. However, it can be seen that after a certain point, the maximum temperature and the rate of temperature increase do not reduce significantly with an increase in thermal conductivity. This is shown in Figure 4.33 (c). The increase in the maximum temperature at the end of the discharge cycle is plotted against thermal conductivity. It can be seen that beyond the thermal conductivity of ~3 W/m.K, which corresponds to the thermal conductivity of paraffin with copper foam, there is no significant reduction in the maximum temperature. By increasing the thermal conductivity from ~3 W/m.K to ~14 W/m.K (an increase of 367%) the increase in the maximum temperature is only reduced by 3.2%. Therefore, the thermal conductivity of ~3 W/m.K is considered the feasible thermal conductivity for Strategy 2.

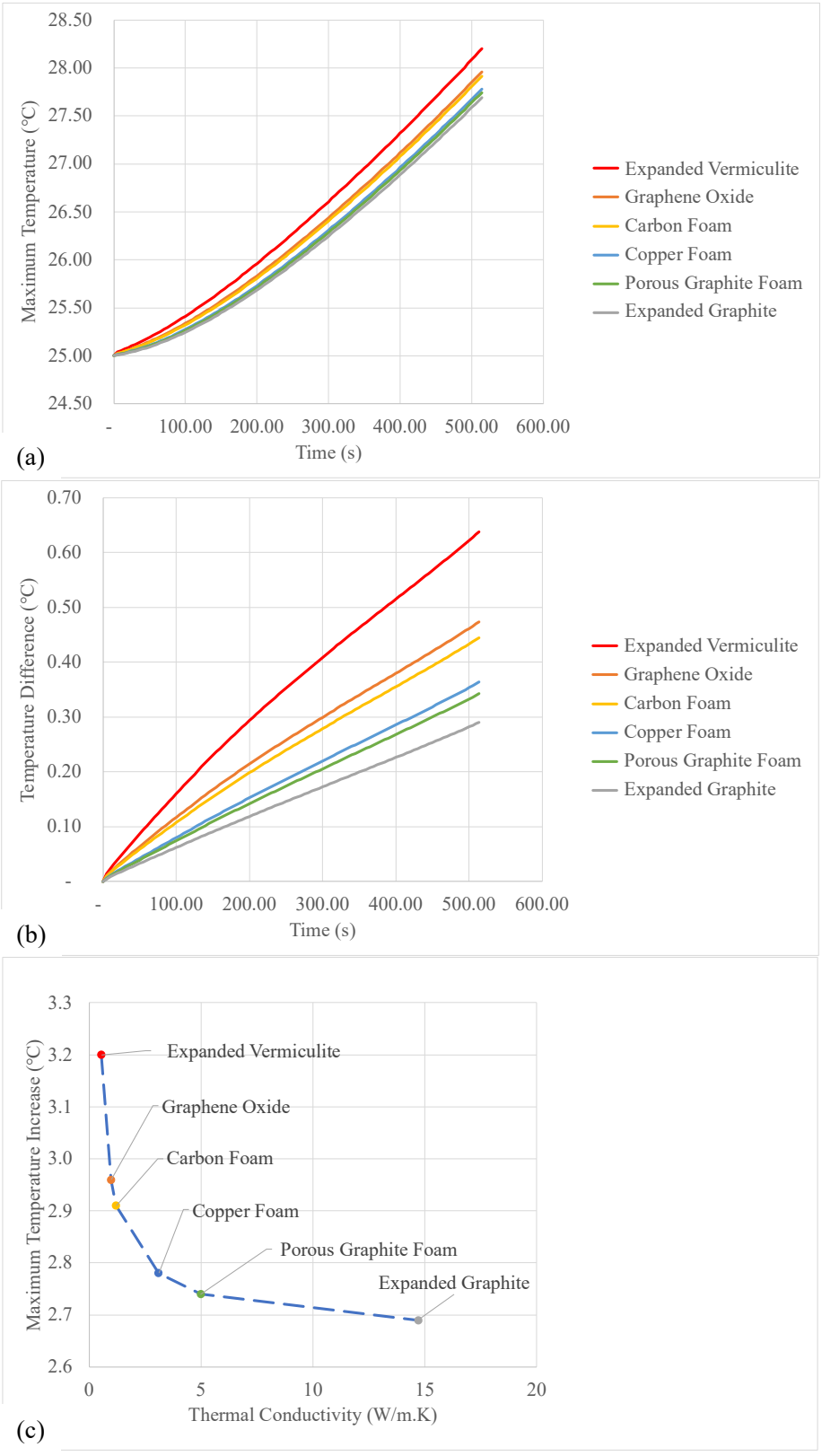

Figure 4.33: Variation of (a) maximum temperature and (b) temperature uniformity with time; (c) Variation of maximum temperature with thermal conductivity for different CPCM.

Moreover, the temperature uniformity of all the CPCM is provided in Figure 4.33 (b). The temperature uniformity by using paraffin was limited to 1.2 °C. Since the thermal conductivity of the CPCM is higher compared to paraffin, therefore, the lowest temperature uniformity is limited to 0.64 °C, which is of paraffin combined with expanded vermiculite. By increasing the thermal conductivity, the rate of maximum temperature increase reduces whereas the rate of minimum temperature increase is not significantly affected, therefore, the difference between the maximum temperature and the minimum temperature reduces, which increases the temperature uniformity further, as shown in Figure 4.33 (b).

By adding the PEM to paraffin base PCM, the latent heat also changes in addition to the change in thermal conductivity. The melting heat capacities for all the CPCM is also provided in Table 3.4. Since the latent heat is utilized when the phase change of the CPCM occurs, therefore, the ambient temperature for all the numerical simulations was set to the phase change temperature. It was setup such that the PCM is solid at the beginning of the discharge rate, and as soon as the cells start to discharge and heat is released, the CPCM uses its latent heat and changes its phase. Due to the CPCM changing its phase, the maximum and minimum temperatures do not increase and stay within the phase change temperature range. Hence, to evaluate the impact of the latent heat of the PCM, the amount of PCM that changed its phase during the discharge cycle was obtained and compared. This is shown in Figure 4.34. Paraffin combined with graphene oxide has the lowest latent heat, and it exhibited the highest phase change percentage of 18.2%. As the latent heat increased with subsequent CPCM, the phase change percentage reduced. The highest latent heat was of paraffin with copper foam which exhibited the lowest phase change percentage of 6.87%. Since paraffin with copper foam has the feasible thermal conductivity and highest latent heat

therefore, it provides the feasible thermal environment for the battery module both outside and within the phase change temperature ranges.

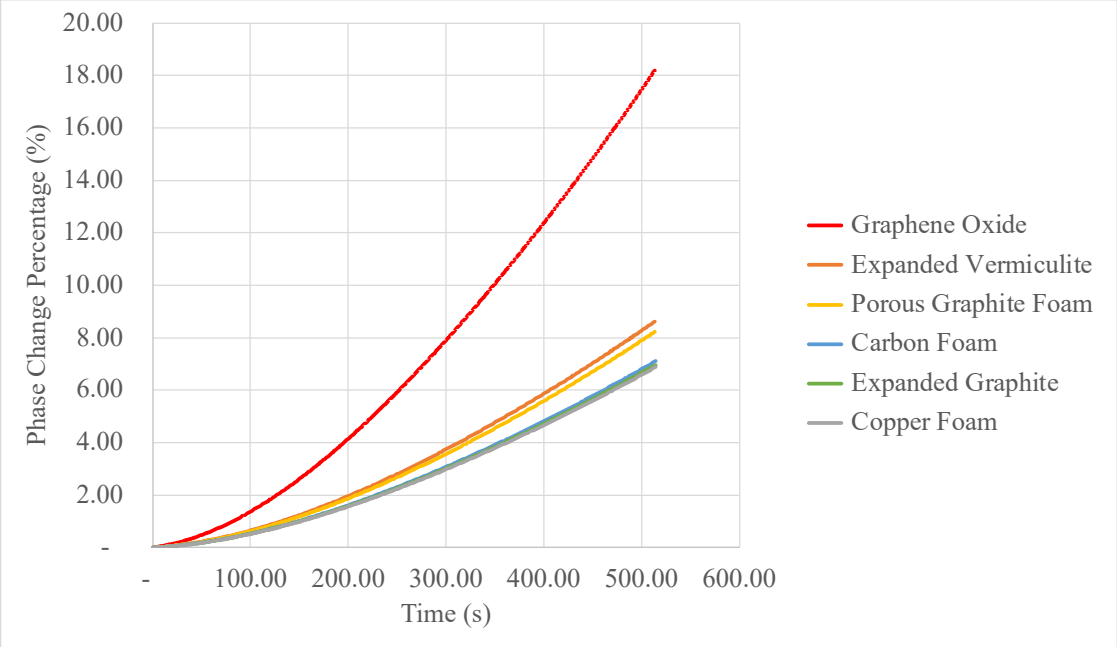

Figure 4.34: Temporal phase change percentage of different CPCM.

4.9.1. Thermal Analysis of Paraffin based CPCM Combined with Copper Foam

In the previous discussions, paraffin with copper foam was selected as the feasible CPCM. Therefore, in order to better understand the cooling phenomenon of Strategy 2 with CPCM (with copper foam) the temperature contours are provided in Figure 4.35. As discussed, two separate simulations were performed. The first simulation was conducted at 25 °C ambient temperature, and the second simulation was conducted at the phase change temperature of the CPCM, which is 42.24 °C in this case. The temperature contours for 25 °C ambient temperature are shown in Figure 4.35 (a), (b), and (c) and the temperature contours for 42.24 °C ambient temperature are shown in Figure 4.35 (d), (e), and (f).

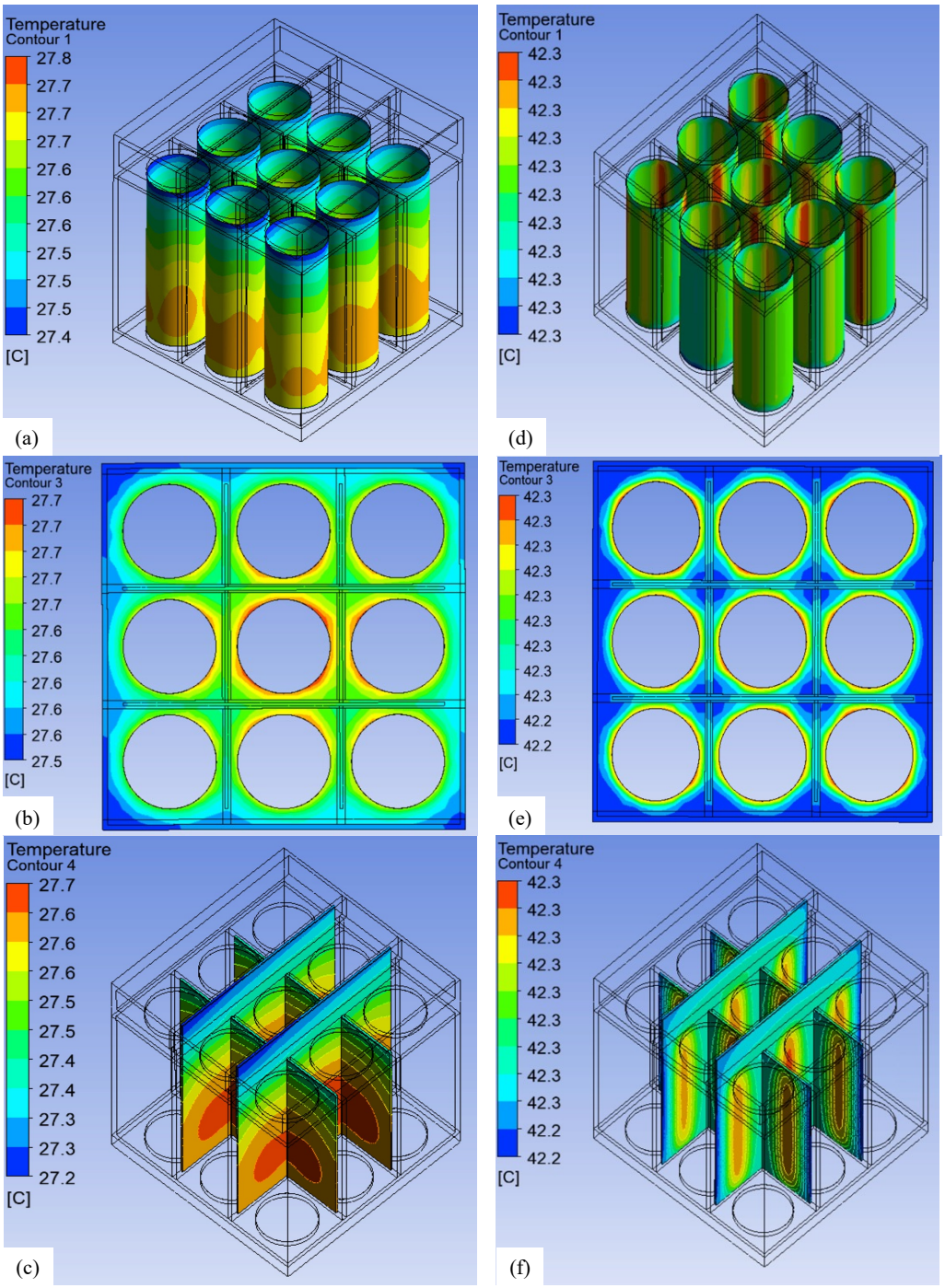

Figure 4.35: Temperature contours of (a) cells, (b) CPCM, and (c) fluid at 25 °C ambient temperature; Temperature contour of (d) cells, (e) CPCM, and (f) fluid at 42.24 °C.

It can be seen that due to the presence of cold plates in between all the surfaces of the neighboring cells, the highest amount of cooling is achieved. The lower temperature surfaces are the ones that are in front of the cold plates, whereas the higher temperature surfaces are the ones that are facing

the module housing. Since the module housing is cooled through the ambient temperature and the airflow at the top of the battery module only, as compared to the liquid cooling effect for the other cell surfaces therefore, these temperatures are higher in comparison. This shows the effectiveness and importance of the presence of liquid cooling within the proposed battery module.

Moreover, it can be seen from Figure 4.35 (b) that the cold plates also act as a heat sink for the CPCM. Through the addition of a cold plate, the high temperature region within the CPCM in between the neighboring cells is eliminated as the fluid extracts heat from the CPCM. Since the high temperature regions are eliminated, therefore the temperature does not reach the phase change temperature of the CPCM, and the melting does not occur.

Additionally, it can be seen in Figure 4.35 (c) that the lower portion of the fluid has the highest temperature, and it gradually reduces to the minimum towards the top portion of the fluid. This is due to the air-cooling effect that occurs at the top of the cold plates that is protruded within the air duct. Additionally, the lowest temperature of the fluid is exhibited near the inlet of the air duct and as the air flows through the cold plate, its heat extraction capacity reduces, and the temperature of the fluid increases towards the outlet of the air duct. The impact of the single fluid body can be seen in Figure 4.35 (c), as the same airflow allows the fluid to cool in between the cell columns as well.

Finally, at the ambient temperature of 42.24 °C, the phase change of the CPCM begins, and it can be seen from Figure 4.35 (d), (e), and (f) that all temperatures for the entire battery pack are within the range of 42.2 to 42.3 °C, as the phase change of the CPCM limits the temperature of the cells and PCM and the airflow at the same temperature limits the cooling of the fluid to the ambient temperature of 42.24 °C.

4.10. Increasing the Thermal Conductivity of Water through Nanoparticles

In the previous discussions, paraffin with copper foam was selected as the feasible CPCM, therefore, it was used as the primary coolant in BM4-C3 and BM4-C4. The thermal conductivity of the water is increased to 0.92 W/m.K (in BM4-C4) from 0.6 W/m.K (BM4-C3) through the addition of nanoparticles (0.04% of silver and 0.16% multi-walled carbon nano-tubes). To compare the two configurations, the amount of CPCM phase change at 42.24 °C ambient temperature and the maximum temperature at 25 °C ambient temperature was evaluated, and the results are provided in Figure 4.36. It can be seen that there is no difference in the graphs of BM4-C3 and BM4-C4 as they overlap each other. This shows that the cooling from the fluid is not sensitive enough to capture the change of 0.32 W/m.K thermal conductivity.

(a)

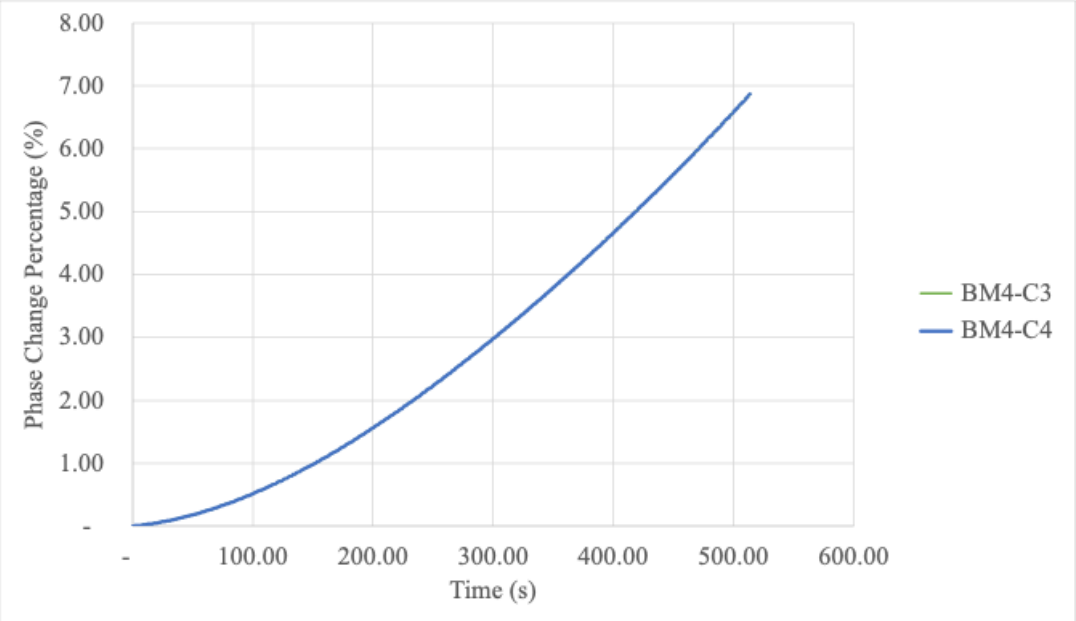

(b)

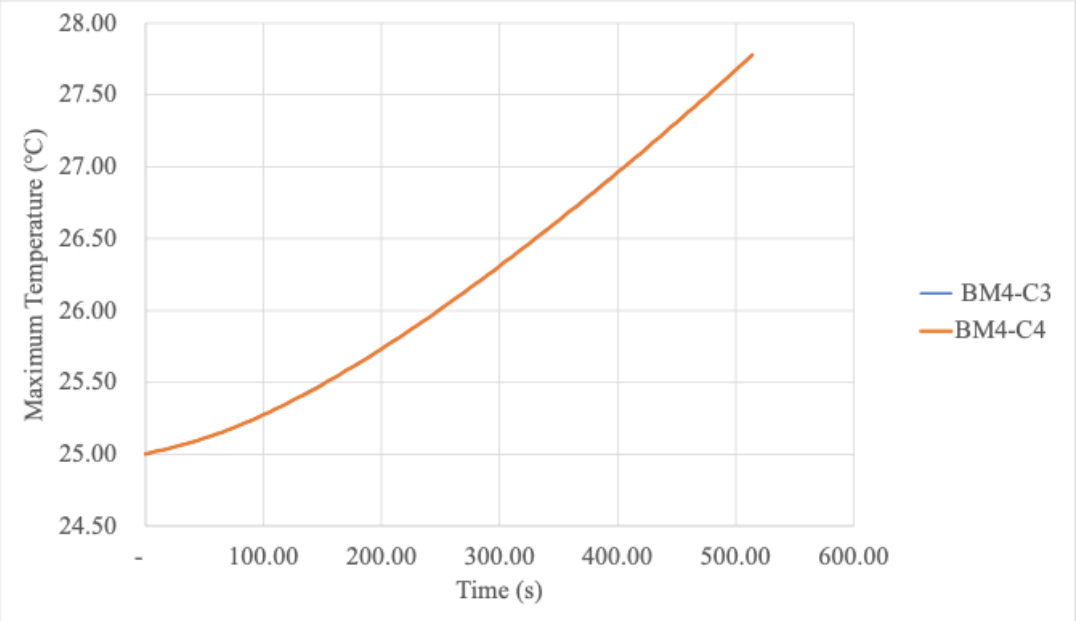

Figure 4.36: CPCM phase change comparison of BM4-C3 and BM4-C4.

4.11. Parametric Study on the Volume of Paraffin based CPCM Combined with Copper Foam

In this parametric study the volume of CPCM-4 was changed by modifying the battery module dimensions. The results of this study are provided in Table 4.4. The total volume of CPCM-4 that changes its phase is 8,045 mm^3 and is the same in all the test configurations as expected. This is the maximum volume of phase change that will occur as the cooling achieved through secondary coolants is the minimum due to high ambient temperature of 42.24 °C. In term of the total CPCM-4 volume the test configuration 6 results in 13.76% utilization of CPCM-4. This shows that at the highest utilization of CPCM-4 the test configuration 6 can sustain seven discharge cycles one after another at a 7 C discharge rate. Compared to test configuration 1, the total CPCM-4 volume is reduced by approximately half in test configuration 6.

Table 4.4: Utilization of CPCM-4 in the different test configurations.

Test Configuration No.	CPCM-4 Utilization (mm^3)	CPCM-4 Utilization in terms of Total CPCM-4 Volume (%)
1	8,045	6.91
2	8,045	7.98
3	8,045	8.63
4	8,045	9.38
5	8,045	10.26
6	8,045	13.76

4.12. Parametric Study on the Inlet Size of Battery Module

In this parametric study the height of the air duct inlet was varied. Since the Reynolds number was the same for all the test configurations therefore, constant CPCM-4 phase change of 8,045 mm^3 was obtained in all. Hence, to evaluate the impact of the inlet height the pressure drop across the air duct was compared. The fan power is dependent on the pressure drop of the airflow. A high pressure drop will result in a high power requirement of the fan. The results are shown in Figure 4.37. It can be seen that as the inlet height increases the maximum pressure drop reduces. The maximum pressure drop reduces at a high rate initially until 6 mm height and then the rate does not drastically reduce beyond this. Therefore, beyond 6 mm height of the air duct the reduction in the maximum pressure drop is not significant enough and it is considered as the feasible height.

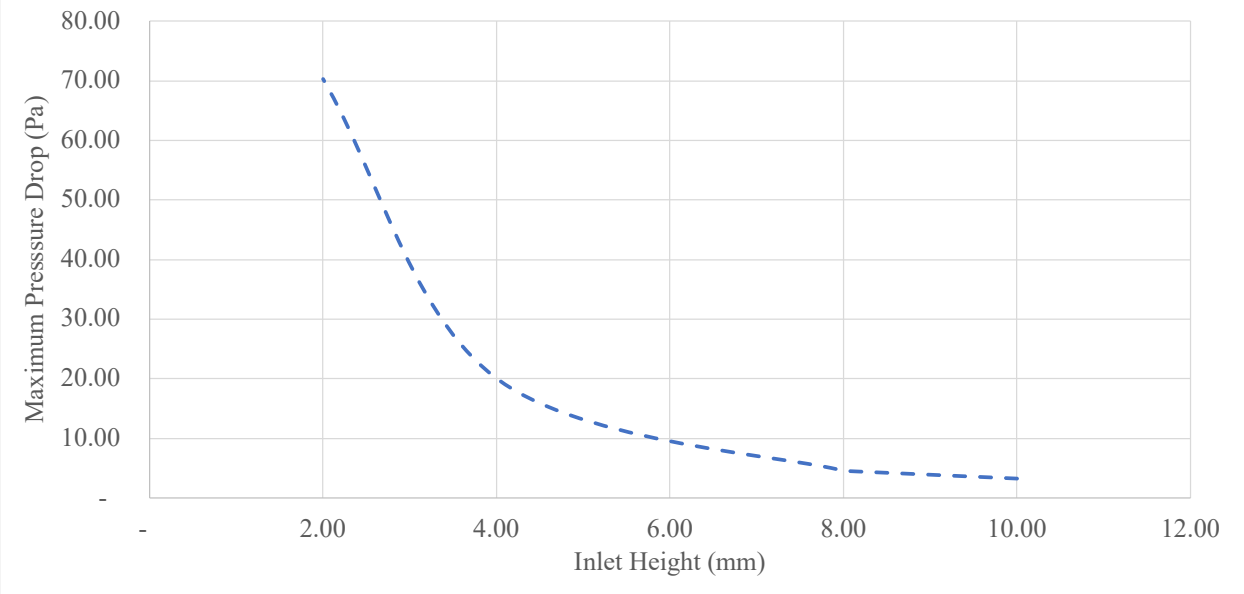

Figure 4.37: Variation of maximum pressure drop with increase in the inlet height.

4.13. Parametric Study on the Airflow Reynolds Number

In this parametric study the Reynolds number of the airflow was increased by a factor of 2 as provided in Table 3.7. This study is important as by increasing the Reynolds number of the airflow the cooling increases, however, after a certain point the increase in cooling is not significant enough compared to the Reynolds number increase. The results of this study are provided in Figure 4.38. It can be seen that the rate of reduction in the maximum and minimum temperatures of the battery module is high initially, however, beyond the Reynolds number of 1,950 and pressure drop of ~10 Pa the reduction is not significant enough. Moreover, a Reynolds number of 1,950 has a lower pressure drop compared to a turbulent flow. Therefore, the feasible Reynolds number is considered as 1,950.

(a)

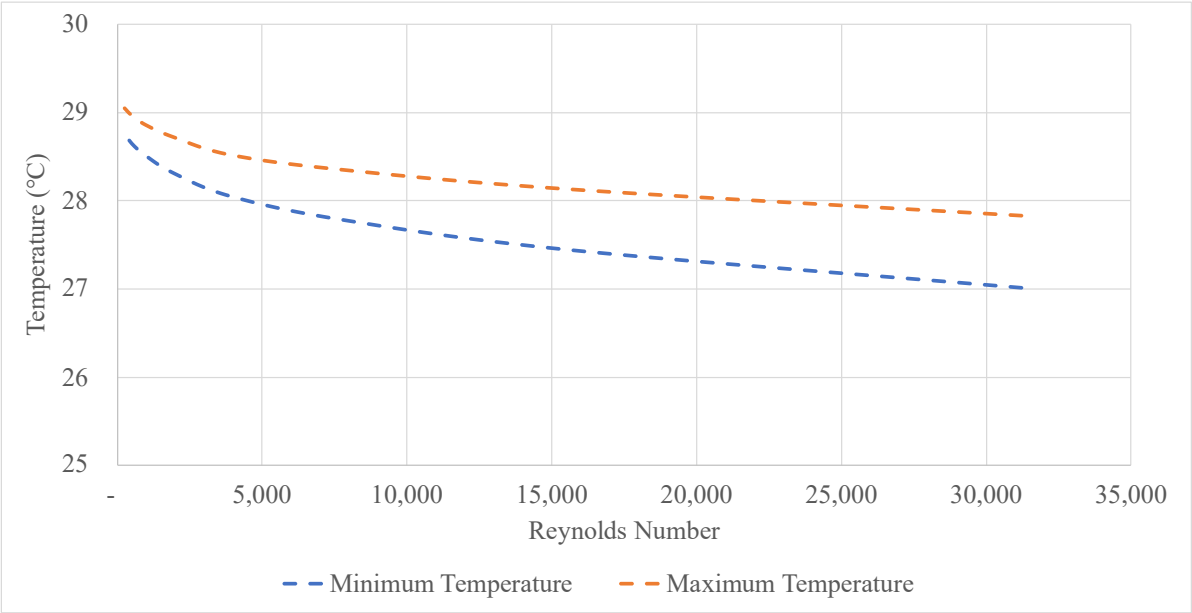

(b)

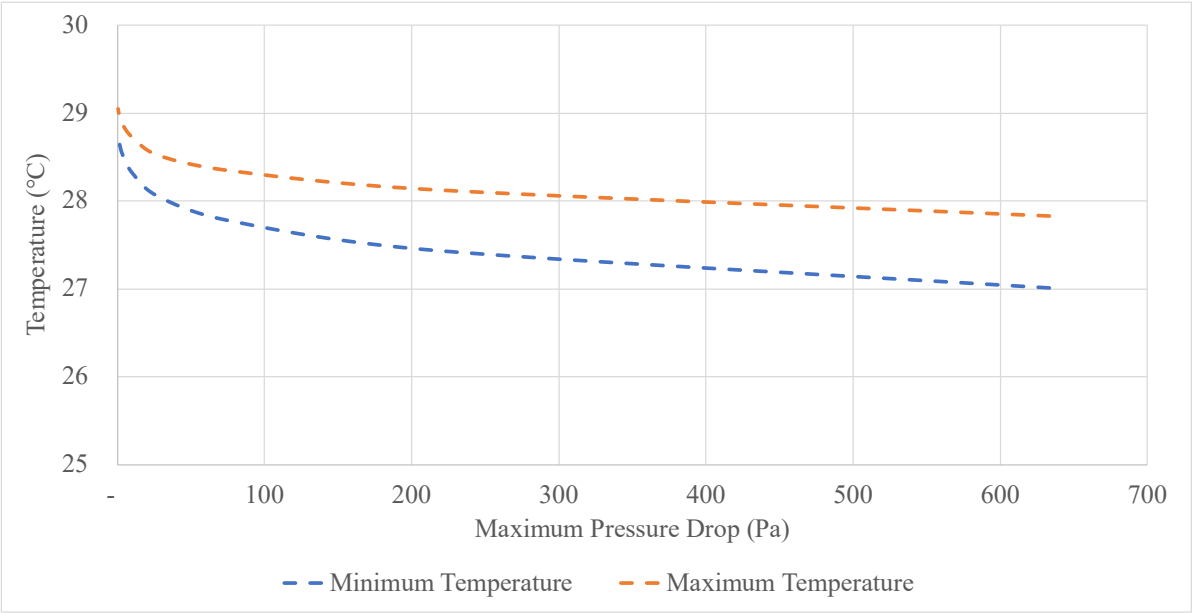

Figure 4.38: Maximum and minimum temperature variation with (a) Reynolds number and (b) maximum pressure drop of airflow.

4.14. Study on Adding Fins to Improve the Heat Transfer

Based on the parametric studies BM4-C3 with 6 mm height of air duct inlet and 1,950 Reynolds number is considered as the feasible configurations. Therefore, this configuration was used as the base configuration for this study. This configuration was then modified to BM5-C1 and BM5-C2 configurations. The fins will assist in improving the heat transfer to airflow as through the fins the contact area with the airflow will increase. However, this increase in heat transfer will come at a cost of higher pressure drop. The results for this study are shown in Figure 4.39. It can be seen that compared to the pressure drop increase the cooling achieved is not significant. With one fin BM5-C1 the pressure drop increases from ~11 Pa to ~38 Pa, whereas, the maximum temperature reduces by only ~0.6 °C. Similarly with two fins the pressure drop increases by ~70 Pa and the maximum temperature reduces by ~0.5 °C. Therefore, the addition of fins does assist in improving the cooling, however, the pressure drop increase is much higher which will result in higher fan power requirements.

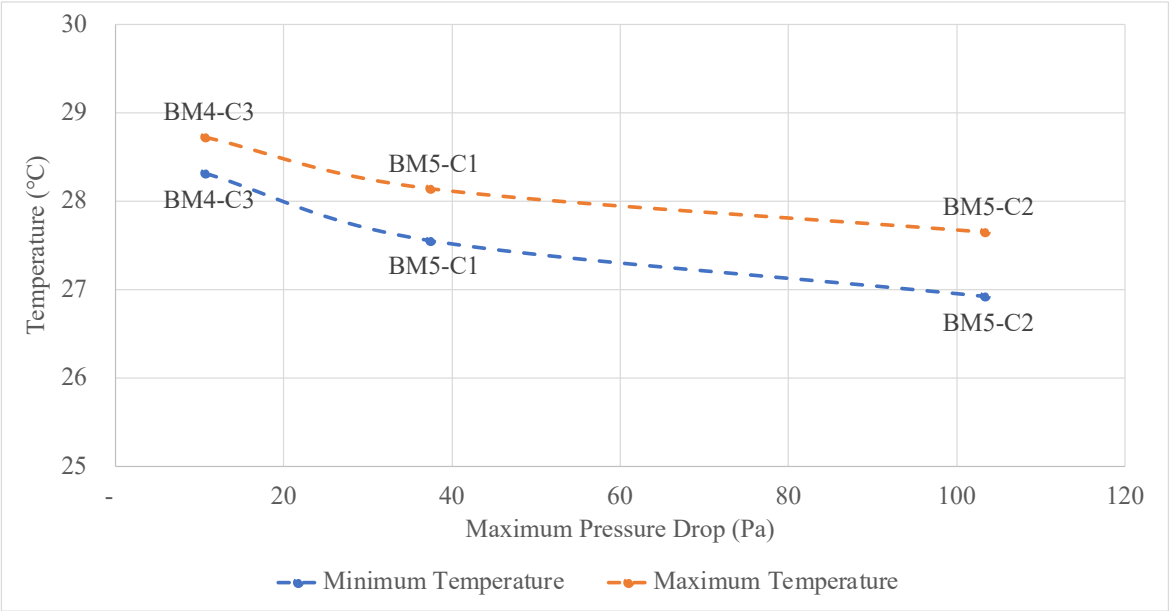

Figure 4.39: Variation of maximum and minimum temperatures with the maximum pressure drop for the three developed configurations.

4.15. Scalability Study of Battery Module

For this study four different numerical simulations were performed. The first simulation consisted of one battery module only, the second consisted of two battery modules in series, the third consisted of three battery modules in series and the fourth consisted of four battery modules in series. The maximum temperature of the airflow and cells was obtained and is provided in Figure 4.40. As expected, it can be seen that the temperature of the airflow and cells increase as the number of the modules increase in series. This is because the air extracts a higher amount of heat from the initial battery modules and as it moves along in series its heat extraction capacity reduces which results in an increase in the temperature. However, due to hybrid design of the developed battery module the impact of this phenomenon has significantly reduces as temperature difference for battery modules is approximately 0.31 °C across the four battery modules. This is mainly because the CPCM is used for the primary coolant, and it extracts the heat and maintains uniformity. This can also be seen in the temperature contours provided in Figure 4.41.

(a)

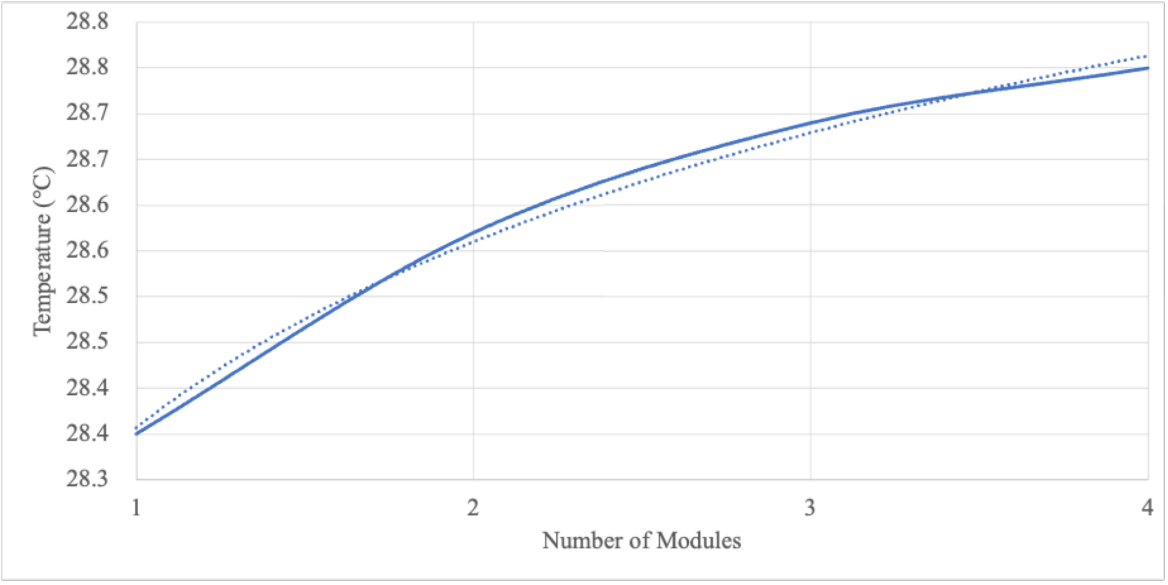

(b)

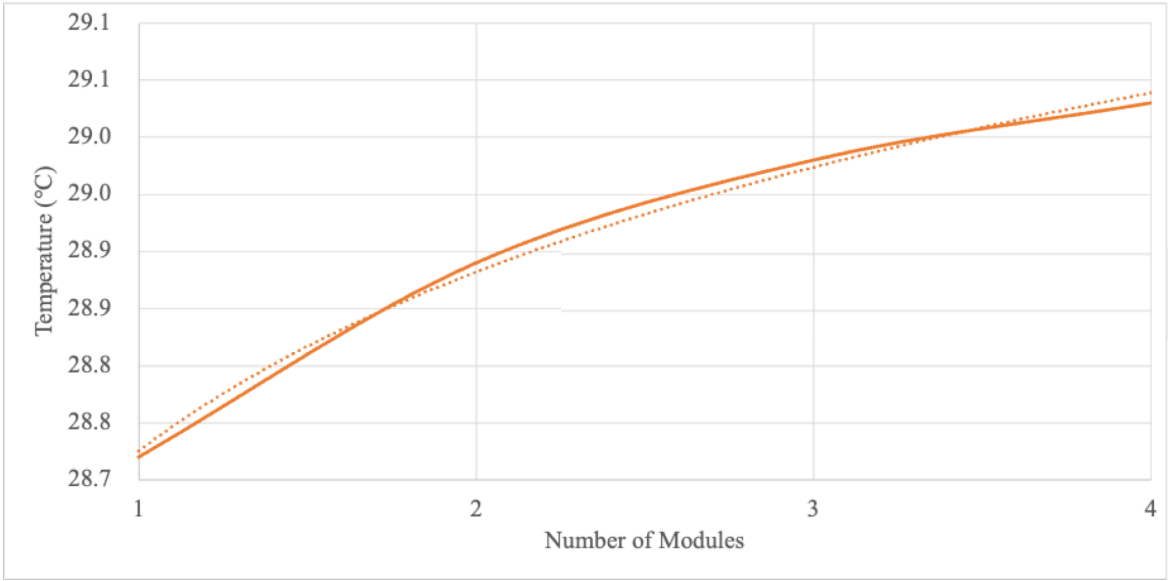

Figure 4.40: Maximum temperature with increasing battery modules for (a) airflow and (b) module.

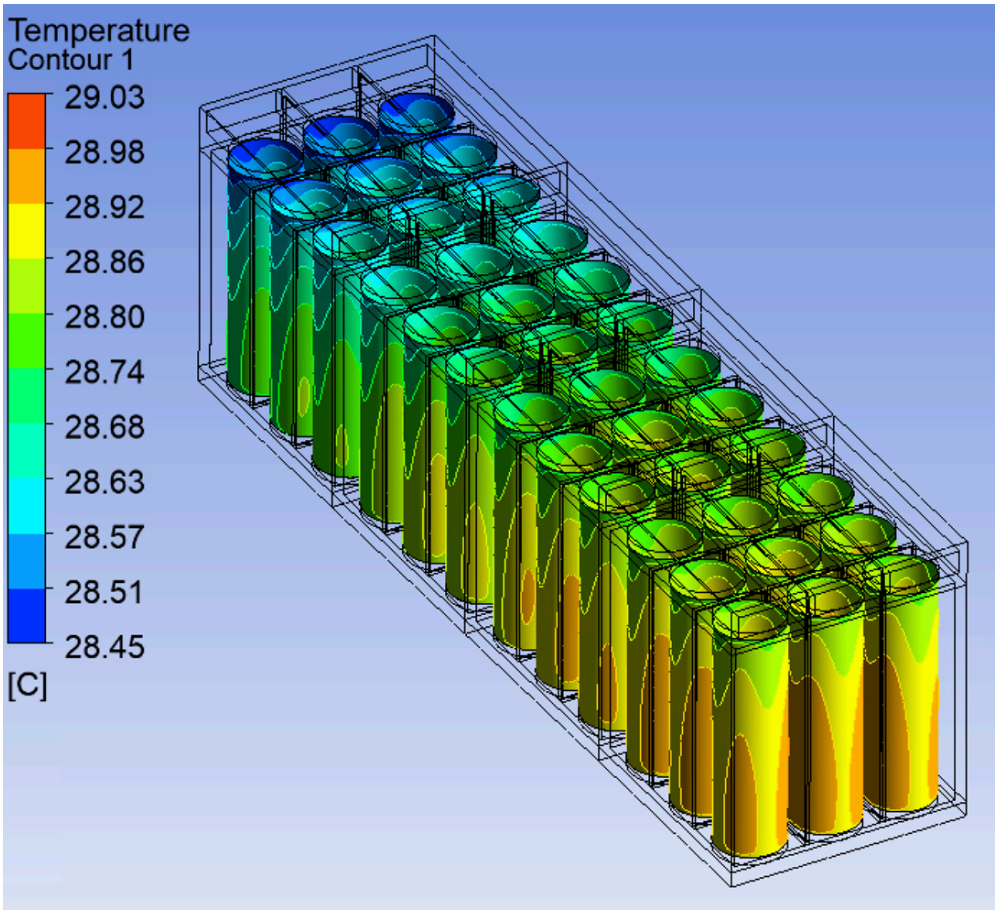

Figure 4.41: Temperature contours of the cells in four battery modules connected in series.

In order to extrapolate the results over the 25 battery modules in series the equations obtained from the trendlines for both the airflow and cell temperature was used and are provided below. The R^2 values for airflow trendline is 0.9953 and battery module trendline is 0.9963.

$$Air\ Flow\ Temperature = 0.293122289793738 \ln B + 28.3571103960402 \quad (4.1)$$

$$Battery\ Module\ Temperature = 0.226234840293359 \ln B + 28.7252533748119 \quad (4.2)$$

Where B is the number of modules attached in series.

The result of this extrapolation is provided in Figure 4.42. It can be seen that the temperature difference between the maximum temperature of the final module and the initial module is 0.72 °C. Whereas, the difference in the airflow is 0.94 °C. Moreover, the overall temperature uniformity across the entire battery pack is 1.14 °C. This shows that even with 25 modules stacked in series the temperature uniformity is still high. Therefore, the developed thermal management strategy is capable of being scaled up or down according to the vehicle requirements.

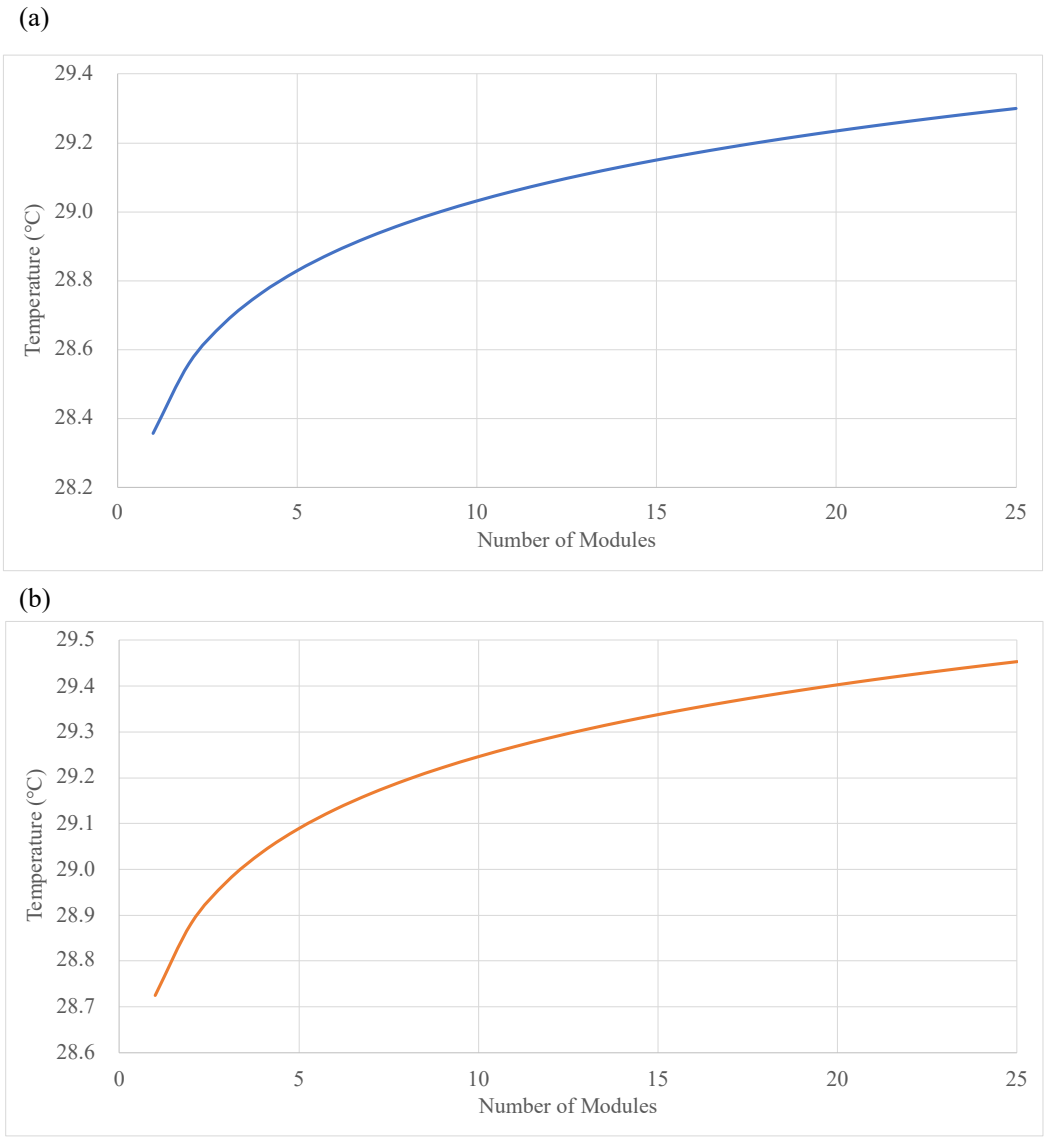

Figure 4.42: Maximum temperature across 25 battery modules for (a) airflow and (b) modules.

Similarly, the pressure drop was also obtained using the numerical simulations and the results for up to 4 battery modules is provided in Figure 4.43(a). A trendline was obtained and the results were extrapolated for entire 25 battery modules in series as shown in Figure 4.43(b) . The trendline equation is provided below.

$$Pressure\ Drop = -0.0459999999999923(B^2) + 2.89520000000002(B) + 7.92099999999991 \quad (4.3)$$

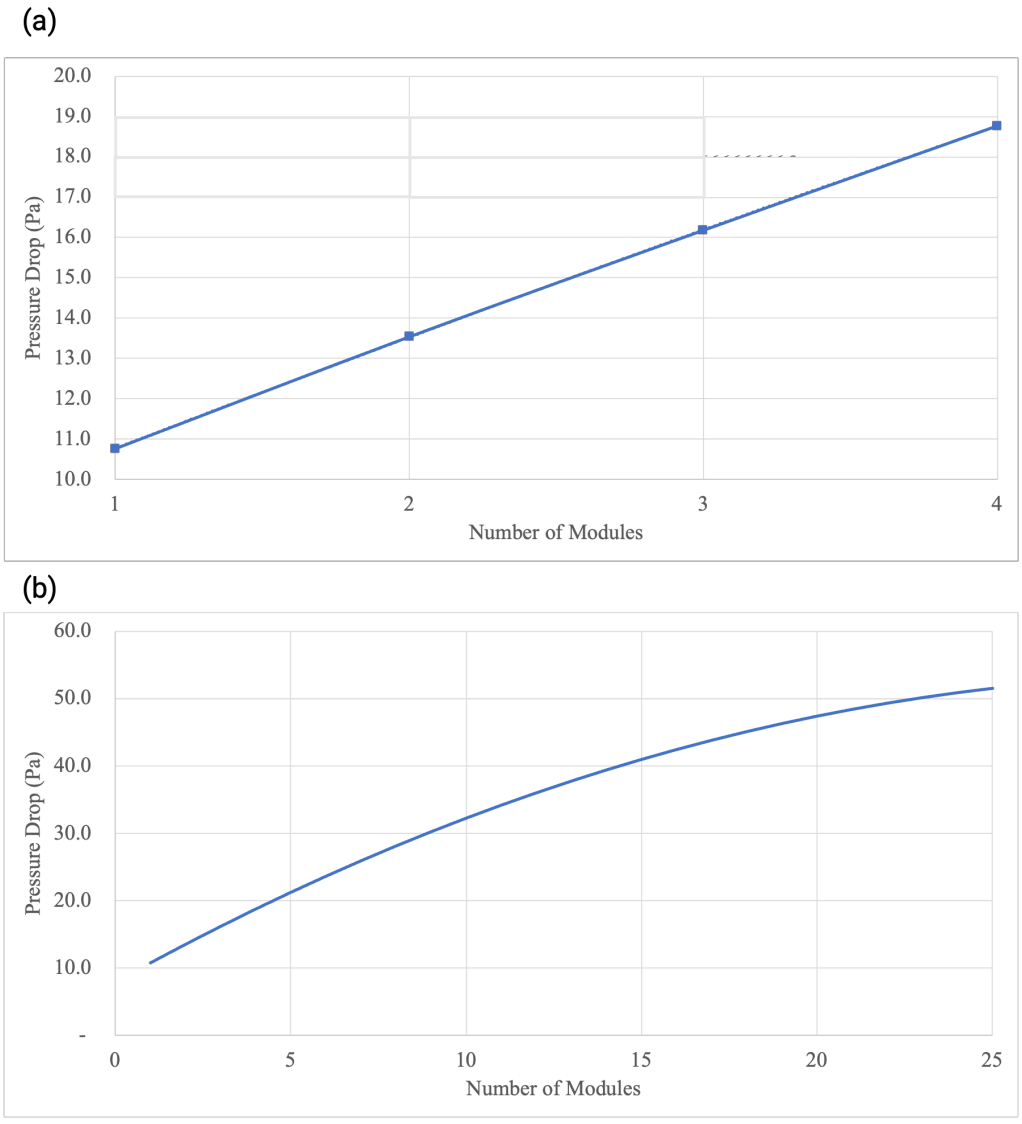

Figure 4.43: Pressure drop across increasing battery modules (a) through numerical simulations and (b) through extrapolation.

Furthermore, to verify a numerical simulation was conducted over the entire 25 battery modules in series and the pressure contours for the single air duct channel are provided in Figure 4.44. For a single battery module, the maximum pressure drop was ~ 10 Pa (Figure 4.37). Whereas, for the 25 battery modules the maximum pressure drop increases to ~51 Pa. Additionally, for a single channel of 19 mm width and 6 mm height the airflow in terms of cubic feet per minute (CFM) at 3.12 m/s amounts to ~0.75 CFM. Hence for the complete battery pack the total CFM requirement will be ~68 CFM.

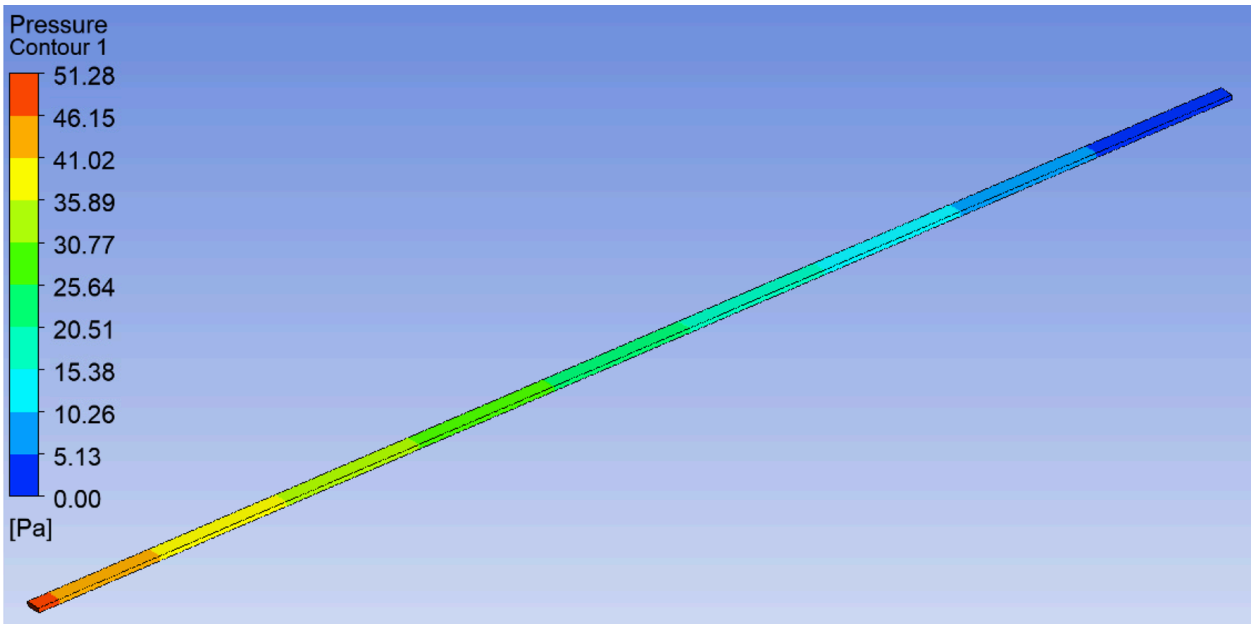

Figure 4.44: Pressure contours for the air duct channel for 25 battery modules in series.

4.16. Comparison with Open Literature

The results obtained from the scalability study was compared with maximum temperature and temperature uniformity of various thermal management strategies developed by researchers in open literature. The comparison is provided in Figure 4.45. Zeng et al. (2022) developed the hybrid strategy by combining liquid cooling and micro heat pipe arrays. Liu et al. (2023) developed the hybrid strategy by combining CPCM and copper tube liquid cooling. Xu et al. (2023) developed a liquid cooling strategy by using a wrench-shaped cold plate with a bifurcation structure. Xiong et al. (2023) developed a novel liquid cooling bionic flow channel in the shape of spider-web and the results were compared with honeycomb and helical flow channels. Ling et al. (2023) designed various configurations of mini-channel cold plates and optimized the designs.

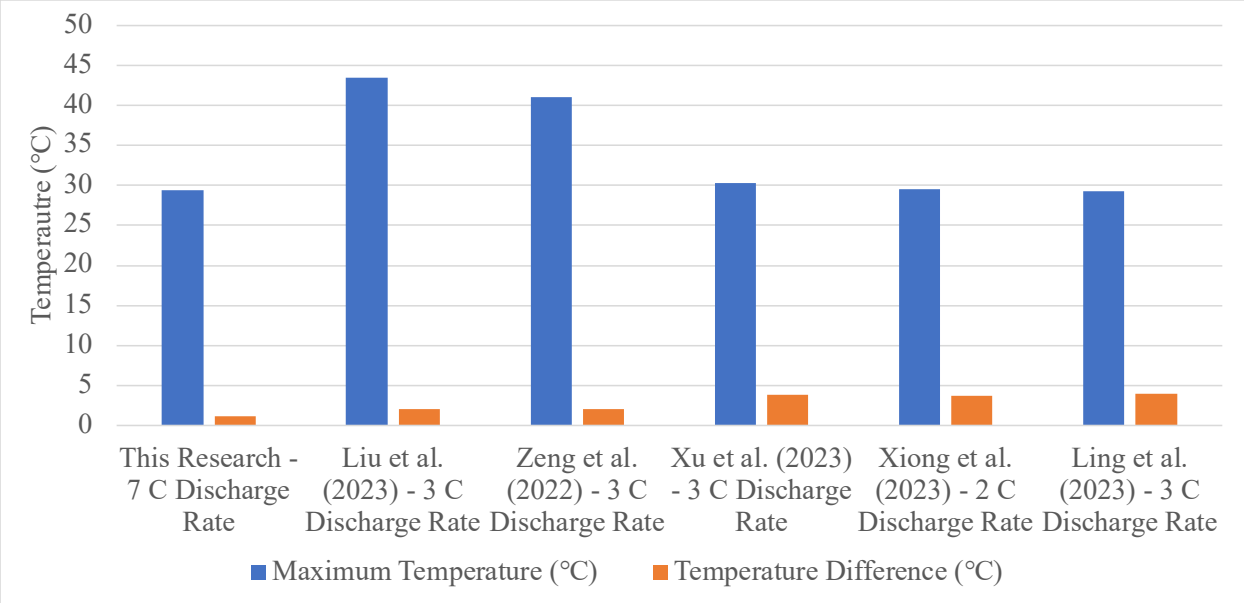

Figure 4.45: Comparison of results with thermal management results in open literature.

It can be seen from Figure 4.45 that the maximum temperature of the scaled battery pack at 7 C discharge rate is similar to the results obtained in the studies in open literature with a smaller sized battery module and discharge rates up to 3 C. Moreover, the temperature uniformity of 1.14 °C of

the scaled battery pack is higher when compared to the studies in open literature. Additionally, the open literature studies require flowing fluid through the entire battery modules which result in power consumption, however, the improved thermal performance obtained from the strategy developed in this research is achieved without flow of fluid and pumping power requirements.

CHAPTER 5: CONCLUSIONS AND FUTURE WORK

This chapter presents the concluding remarks for the research work done in this thesis. This is followed by a list of the novelties and contributions from this research. Finally, the limitations and recommendations for future work are presented.

5.1. Summary of Results and Conclusions

Lithium-ion batteries are the most promising batteries for electric vehicles, but they have problems associated with their thermal performance. In this research, the issues of thermal performance and temperature non-uniformity in lithium-ion batteries were investigated. A comprehensive literature review of the literature identified some gaps including a lack of thermal management strategies that can reduce the power requirements and improve the cooling and temperature uniformity of the lithium-ion batteries. To contribute in overcoming these challenges, multiple hybrid cooling strategies have been developed and proposed that combine air, liquid, and phase change material cooling. Based on the developed strategies distinct battery module configurations have been designed and developed. Experimental studies were conducted on the developed battery module to obtain heat flux and temperature profiles of the cells. Additionally, the numerical model was developed and validated using the experimental results. Numerical simulations were then conducted for all the battery module configurations proposed. The effectiveness of the new strategies was examined, and the results suggest that the primary coolant (composite phase change material) improves the temperature uniformity within the battery module, and the secondary coolants (fluid in cold plates and airflow in the air duct) increases the cooling within the battery module by extracting heat from the composite phase change material simultaneously. A summary of the results and the conclusions drawn are as follows:

- The results of the transient feasibility study concluded that the phase change percentage of the paraffin in configurations with PCM cooling only and hybrid of PCM and liquid cooling was ~10.3%. Whereas the phase change percentage of paraffin in hybrid configuration of PCM, liquid, and air cooling (Strategy 1) was ~6.1% and it exhibited a better thermal performance.
- When comparing different configuration of liquid channels within Strategy 1 the maximum temperature was maintained at approximately 31.5 °C in all the configurations, however, the highest temperature uniformity of 1.75 °C was exhibited by the configuration in which the liquid channels were placed in between the PCM.
- The results indicated that a single discharge cycle was not enough to completely analyze the thermal performance of Strategy 1 with a PCM of higher phase change temperature as the maximum temperature did not reach the phase change temperature of the PCM. Based on further investigation, it was found that the maximum temperature reached the phase change temperature of PCM in the fifth discharge cycle, and through the use of latent heat, the maximum temperature of the battery module was maintained between 42 – 44 °C. Moreover, the temperature uniformity started to increase once the phase change temperature of the PCM was reached. Finally, by the end of the last discharge cycle, phase change occurred in only 2.3% of the PCM.
- Thermal performance of Strategy 1 was obtained for 1 C, 2 C, 3 C, 5 C, and 7 C discharge rates. Based on the results, the maximum temperatures were limited to ~30 °C since, at this point, any additional heat from the cell is extracted using the latent heat of the PCM.
- When comparing Strategy 1 and Strategy 2 the results show that the highest cooling was achieved through Strategy 2 (with cold plates in between the cell columns and rows) as the maximum temperature was limited to 29.1 °C and a high temperature uniformity was achieved

by the end of the discharge cycle with the difference between the maximum and minimum temperature limited to 1.2 °C. Additionally, none of the PCM was melted as the maximum temperature was maintained below the phase change temperature of the PCM.

- Strategy 2 was then used to investigate the impact of different ambient temperatures on the thermal management system. The results concluded that it is vital to use a composite PCM with increased thermal conductivity as outside the phase change temperatures, the thermal conductivity will be used to extract the heat from the cells. Since the temperature increase is limited to 4.1 °C, it can be used at 45 °C ambient temperature and the maximum temperature will be limited to less than 50 °C, which is the high end of the tolerable temperature range of the Li-ion cell. Furthermore, various composite PCM were used to investigate the variations of the thermal conductivity. It was found that beyond a thermal conductivity of ~3 W/m.K, which corresponds to the thermal conductivity of paraffin combined with copper foam, there is no significant reduction in the maximum temperature. Since paraffin with copper foam has the feasible thermal conductivity and highest latent heat therefore, it provides the feasible thermal environment for the battery module both outside and within the phase change temperature ranges. Moreover, at a 7 C discharge rate, it exhibited the lowest phase change percentage of 6.87%.
- When comparing the addition of nanoparticles to increase the thermal conductivity of water the results concluded that the cooling from the fluid is not sensitive enough to capture the increase of 0.32 W/m.K thermal conductivity through the use of nanoparticles.
- Through the parametric studies the composite PCM volume requirement was reduced by ~50%. With the modified volume the battery module is capable of sustaining seven discharge cycles one after another at a 7 C discharge rate. Additionally, beyond 6 mm height of the air

duct the reduction in maximum pressure drop is not significant enough and it is considered as the feasible height. Furthermore, beyond the Reynolds number of 1,950 and pressure drop of ~10 Pa the reduction in the maximum and minimum temperatures is not significant enough.

- In order to enhance the cooling in the airflow Strategy 2 was modified by adding fins to the protruded cold plate section in the air duct. The results showed that the addition of fins does assist in improving the cooling, however, the pressure drop increase is much higher which will result in higher fan power requirements.
- When scaled up to an entire battery pack the overall temperature uniformity across the pack is 1.14 °C with a maximum temperature of 29.45 °C, which is within the feasible operating temperature and uniformity ranges. Therefore, the developed thermal management strategy is capable of being scaled up or down according to the energy and power requirements.

The hybrid thermal management strategies developed and used in this study was able to limit the maximum temperature of the battery module to below ~29 ºC, which is a significant improvement over battery modules developed for similar batteries in the open literature. The developed battery module also achieved the desired temperature uniformity to less than 5 ºC. Furthermore, the proposed strategy eliminates the requirement of a pump and reservoir since there is no flow of liquid within the battery module. This reduces the energy required for the operation of the thermal management system, thereby increasing the available energy for propulsion. Therefore, it can be concluded that the proposed battery module is capable of maintaining the thermal environment required by the Li-ion cells for effective performance with the ability to be scaled up to an entire battery pack for an electric vehicle.

5.2. Novelty

The novelty of this research are as follows:

- A novel hybrid thermal management strategy is developed by incorporating air cooling, liquid cooling, and phase change material.
- A novel configuration is developed that uses secondary coolants (air and liquid) to extract heat simultaneously from the phase change material which results in increased heat extraction capability of the phase change material and the thermal performance of the battery module.
- A novel configuration of hybrid thermal management strategy is developed which utilizes stationary fluid and does not require any pumps or reservoirs which increases the energy availability for the propulsion of the electric vehicle.
- A novel design of cold plate is developed for hybrid thermal management strategy which is capable of being placed in between the cell rows and columns and contains a single fluid body to improve thermal performance of the battery module.
- A novel modular battery pack design is developed which is capable of scalability in power and energy.

5.3. Contributions

The contributions from this research are as follows:

- The developed hybrid thermal management strategy is compared with traditional phase change cooling and liquid cooling strategies.
- Multiple configurations of the hybrid thermal strategies are developed and compared.
- Heat flux profiles are obtained for the Lithium-ion cell at various cell discharge rates ranging from 1 C to 7 C.
- New high-fidelity numerical models are developed and validated with experimental data to accurately predict the thermal performance of the developed hybrid thermal management strategies.
- The hybrid battery module is examined under various ambient conditions.
- Several composite phase change materials with property enhancing materials are added to the hybrid battery module and the results are compared and analyzed.
- Environmentally friendly fluid such as water is used to improve sustainability and eliminate the emission of harmful gases and vapors into the environment.

5.4. Limitations

The limitations of the research performed in this thesis are as follows:

- The research was conducted on 18650 Li-ion cells and it is not applicable to larger cells without further investigation.
- The research was conducted on cylindrical Li-ion cells and it is not applicable to different cell geometries without further investigation.
- The research is done on Li-ion cells and may not be applicable to cells with different battery chemistries without further investigation.
- The research is not applicable to discharge rates higher than 7 C without further investigation.
- The structural integrity of various developed components has not been investigated.

5.5. Future Directions and Outlook

As concluded above, the hybrid thermal management strategy is capable of maintaining the battery module temperatures within the feasible operating range while significantly reducing the energy requirements for the operation of the thermal management system. However, gaps still remain which require further investigation and research in order to apply this strategy to practical applications. Therefore, several recommendations can be made for future research as listed below:

- Experiments should be conducted to obtain heat flux profiles of Lithium-ion cells at high charging rates and at various drive cycles and use it to obtain and improve the thermal performance of the hybrid battery module.
- The developed numerical model should be modified by coupling the electrochemical model as well and comparing its impact in order to further improve the developed model.
- Experiment should be conducted by developing a prototype of the scaled-up battery pack to improve the numerical simulations for scaled battery pack and further validate it.
- A study should be conducted for the developed hybrid battery module with larger Lithium-ion cells such as the 26650 and 42120 cylindrical cells.
- A study should be conducted to evaluate the performance of the developed hybrid thermal management strategies with different cell geometries such as the prismatic and pouch cells.
- An experimental and numerical study should be conducted to evaluate the performance of the developed hybrid thermal management strategies and battery module in instances of thermal runaway.
- The developed hybrid strategy should be modified to withstand thermal runaway and its propagation.

REFERENCES

Abdul-Quadir, Y., Laurila, T., Karppinen, J., Jalkanen, K., Vuorilehto, K., Skogström, L., & Paulasto-Kröckel, M. (2014). Heat generation in high power prismatic Li-ion battery cell with LiMnNiCoO2 cathode material. *International Journal of Energy Research*, *38*(11), 1424–1437. https://doi.org/10.1002/er.3156

Al-Hallaj, S., & Selman, J. R. (2000). A Novel Thermal Management System for Electric Vehicle Batteries Using Phase-Change Material. *Journal of The Electrochemical Society*, *147*(9), 3231. https://doi.org/10.1149/1.1393888

Al-Zareer, M., Dincer, I., & Rosen, M. A. (2017a). Electrochemical modeling and performance evaluation of a new ammonia-based battery thermal management system for electric and hybrid electric vehicles. *Electrochimica Acta*, *247*, 171–182. https://doi.org/10.1016/j.electacta.2017.06.162

Al-Zareer, M., Dincer, I., & Rosen, M. A. (2017b). Novel thermal management system using boiling cooling for high-powered lithium-ion battery packs for hybrid electric vehicles. *Journal of Power Sources*, *363*, 291–303. https://doi.org/10.1016/j.jpowsour.2017.07.067

Al-Zareer, M., Dincer, I., & Rosen, M. A. (2018a). A novel phase change based cooling system for prismatic lithium ion batteries. *International Journal of Refrigeration*, *86*, 203–217. https://doi.org/10.1016/j.ijrefrig.2017.12.005

Al-Zareer, M., Dincer, I., & Rosen, M. A. (2018b). Heat and mass transfer modeling and assessment of a new battery cooling system. *International Journal of Heat and Mass Transfer*, *126*, 765–778. https://doi.org/10.1016/j.ijheatmasstransfer.2018.04.157

Al-Zareer, M., Dincer, I., & Rosen, M. A. (2018c). Heat transfer modeling of a novel battery thermal management system. *Numerical Heat Transfer; Part A: Applications*, *73*(5), 277–290. https://doi.org/10.1080/10407782.2018.1439237

Al-Zareer, M., Dincer, I., & Rosen, M. A. (2018d). Performance assessment of a new hydrogen cooled prismatic battery pack arrangement for hydrogen hybrid electric vehicles. *Energy Conversion and Management*, *173*, 303–319. https://doi.org/10.1016/j.enconman.2018.07.072

Amburi, P. K., Senthilkumar, G., & Nithya, A. (2023). Novel use of CuO nanoparticles additive for improving thermal conductivity of MgO/water and MWCNT/water nanofluids. *Journal of Thermal Analysis and Calorimetry*. https://doi.org/10.1007/s10973-023-12374-z

ANSYS. (2020). *ANSYS Fluent Theory Guide*.

Bandhauer, T. M., Garimella, S., & Fuller, T. F. (2011). A Critical Review of Thermal Issues in Lithium-Ion Batteries. *Journal of The Electrochemical Society*, *158*(3). https://doi.org/10.1149/1.3515880/XML

Beauregard, G. P. (2008). *REPORT OF INVESTIGATION: HYBRIDS PLUS PLUG IN HYBRID ELECTRIC VEHICLE Revision 1*.

Berini, G. A., Fagas, G., Paul, L. G. and D., Berini, G. A., Fagas, G., & Paul, L. G. and D. (2014). A Research Agenda Towards Zero-Power ICT. *ICT - Energy - Concepts Towards Zero - Power Information and Communication Technology*. https://doi.org/10.5772/57347

Bioucas, F. E. B., Köhn, C., Jean-Fulcrand, A., Garnweitner, G., Koller, T. M., & Fröba, A. P. (2022). Effective Thermal Conductivity of Nanofluids Containing Silicon Dioxide or Zirconium Dioxide Nanoparticles Dispersed in a Mixture of Water and Glycerol. *International Journal of Thermophysics*, *43*(11). https://doi.org/10.1007/s10765-022-03084-z

Blum, A., & Long, R. T. (2015). Full-scale Fire Tests of Electric Drive Vehicle Batteries. *SAE International Journal of Passenger Cars - Mechanical Systems*, *8*(2), 565–572. https://doi.org/10.4271/2015-01-1383

Chen, M., Bai, F., Lin, S., Song, W., Li, Y., & Feng, Z. (2019). Performance and safety protection of internal short circuit in lithium-ion battery based on a multilayer electro-thermal coupling model. *Applied Thermal Engineering*, *146*, 775–784. https://doi.org/10.1016/J.APPLTHERMALENG.2018.10.011

Chen, M., Dongxu, O., Liu, J., & Wang, J. (2019). Investigation on thermal and fire propagation behaviors of multiple lithium-ion batteries within the package. *Applied Thermal Engineering*, *157*, 113750. https://doi.org/10.1016/j.applthermaleng.2019.113750

Chen, S., Garg, A., Gao, L., & Wei, X. (2021). An experimental investigation for a hybrid phase change material-liquid cooling strategy to achieve high-temperature uniformity of Li-ion battery module under fast charging. *International Journal of Energy Research*, *45*(4), 6198–6212. https://doi.org/10.1002/ER.6241

Coman, P. T., Rayman, S., & White, R. E. (2016). A lumped model of venting during thermal runaway in a cylindrical Lithium Cobalt Oxide lithium-ion cell. *Journal of Power Sources*, *307*, 56–62. https://doi.org/10.1016/j.jpowsour.2015.12.088

Corasaniti, S., Bovesecchi, G., & Gori, F. (2021). Experimental Thermal Conductivity of Alumina Nanoparticles in Water With and Without Sonication. *International Journal of Thermophysics*, *42*(2). https://doi.org/10.1007/s10765-020-02771-z

Dhameja, S. (2001). Electric vehicle battery systems. *Elsevier.*

Dubey, P., Pulugundla, G., & Srouji, A. K. (2021). Direct Comparison of Immersion and Cold-Plate Based Cooling for Automotive Li-Ion Battery Modules. *Energies, 14*(5), 1259. https://doi.org/10.3390/EN14051259

EPA. (2021). *Fast Facts on Transportation Greenhouse Gas Emissions*. Retrieved September 27, 2023, from https://www.epa.gov/greenvehicles/fast-facts-transportation-greenhouse-gas-emissions

Fan, Y., Bao, Y., Ling, C., Chu, Y., Tan, X., & Yang, S. (2019). Experimental study on the thermal management performance of air cooling for high energy density cylindrical lithium-ion batteries. *Applied Thermal Engineering*, *155*, 96–109. https://doi.org/10.1016/j.applthermaleng.2019.03.157

Farrington, M. D. (2001). Safety of lithium batteries in transportation. *Journal of Power Sources*, *96*(1), 260–265. https://doi.org/10.1016/S0378-7753(01)00565-1

Feng, X., Fang, M., He, X., Ouyang, M., Lu, L., Wang, H., & Zhang, M. (2014). Thermal runaway features of large format prismatic lithium ion battery using extended volume accelerating rate calorimetry. *Journal of Power Sources*, *255*, 294–301. https://doi.org/10.1016/j.jpowsour.2014.01.005

Feng, X., He, X., Ouyang, M., Lu, L., Wu, P., Kulp, C., & Prasser, S. (2015). Thermal runaway propagation model for designing a safer battery pack with 25Ah LiNixCoyMnzO2 large format lithium ion battery. *Applied Energy*, *154*, 74–91. https://doi.org/10.1016/j.apenergy.2015.04.118

Feng, X., Ouyang, M., Liu, X., Lu, L., Xia, Y., & He, X. (2018). Thermal runaway mechanism of lithium ion battery for electric vehicles: A review. *Energy Storage Materials*, *10*, 246–267. https://doi.org/10.1016/j.ensm.2017.05.013

Feng, X., Sun, J., Ouyang, M., Wang, F., He, X., Lu, L., & Peng, H. (2015a). Characterization of penetration induced thermal runaway propagation process within a large format lithium ion battery module. *Journal of Power Sources*, *275*, 261–273. https://doi.org/10.1016/j.jpowsour.2014.11.017

Feng, X., Sun, J., Ouyang, M., Wang, F., He, X., Lu, L., & Peng, H. (2015b). Characterization of penetration induced thermal runaway propagation process within a large format lithium ion battery module. *Journal of Power Sources*, *275*, 261–273. https://doi.org/10.1016/j.jpowsour.2014.11.017

Finegan, D. P., Darcy, E., Keyser, M., Tjaden, B., Heenan, T. M. M., Jervis, R., Bailey, J. J., Malik, R., Vo, N. T., Magdysyuk, O. V., Atwood, R., Drakopoulos, M., DiMichiel, M., Rack, A., Hinds, G., Brett, D. J. L., & Shearing, P. R. (2017). Characterising thermal runaway within lithium-ion cells by inducing and monitoring internal short circuits. *Energy and Environmental Science*, *10*(6), 1377–1388. https://doi.org/10.1039/c7ee00385d

Ghasemi, M., Niknejadi, M., & Toghraie, D. (2021). Direct effect of nanoparticles on the thermal conductivity of CuO-water nanofluid in a phase transition phenomenon using molecular dynamics simulation. *Journal of Thermal Analysis and Calorimetry*, *144*(6), 2483–2495. https://doi.org/10.1007/s10973-020-10453-z

Ghiji, M., Novozhilov, V., Moinuddin, K., Joseph, P., Burch, I., Suendermann, B., & Gamble, G. (2020). A review of lithium-ion battery fire suppression. *Energies, 13*(9). https://doi.org/10.3390/en13195117

Goodenough, J. B. (2015). Energy storage materials: A perspective. *Energy Storage Materials*, *1*, 158–161. https://doi.org/10.1016/J.ENSM.2015.07.001

Hamisi, C. M., Chombo, P. V., Laoonual, Y., & Wongwises, S. (2022). An Electrothermal Model to Predict Thermal Characteristics of Lithium-Ion Battery under Overcharge Condition. *Energies*, *15*(6). https://doi.org/10.3390/EN15062284

He, F., Ams, A. A., Roosien, Y., Tao, W., Geist, B., & Singh, K. (2017). Reduced-order thermal modeling of liquid-cooled lithium-ion battery pack for EVs and HEVs. *2017 IEEE Transportation and Electrification Conference and Expo*, 507–511. https://doi.org/10.1109/ITEC.2017.7993322

He, F., Li, X., Zhang, G., Zhong, G., & He, J. (2018). Experimental investigation of thermal management system for lithium ion batteries module with coupling effect by heat sheets and phase change materials. *International Journal of Energy Research*, *42*(10), 3279–3288. https://doi.org/10.1002/er.4081

He, F., & Ma, L. (2015). Thermal Management in Hybrid Power Systems Using Cylindrical and Prismatic Battery Cells. *Heat Transfer Engineering*, *37*(6), 581–590. https://doi.org/10.1080/01457632.2015.1060776

Hoh, M., & Fuhr, J. (2009). *EVS24 Stavanger, Norway*. 1–10.

Hu, L. L., Zhang, Z. W., Zhou, M. Z., & Zhang, H. J. (2020). Crushing behaviors and failure of packed batteries. *International Journal of Impact Engineering*, *143*. https://doi.org/10.1016/j.ijimpeng.2020.103618

Huang, P., Ping, P., Li, K., Chen, H., Wang, Q., Wen, J., & Sun, J. (2016). Experimental and modeling analysis of thermal runaway propagation over the large format energy storage battery module with Li4Ti5O12 anode. *Applied Energy*, *183*, 659–673. https://doi.org/10.1016/j.apenergy.2016.08.160

Huat, B. S. L. (2014). THERMAL MANAGEMENT OF ELECTRIC VEHICLE BATTERY PACKS. *National University of Singapore*.

Hussain, A., Abidi, I. H., Tso, C. Y., Chan, K. C., Luo, Z., & Chao, C. Y. H. (2018). Thermal management of lithium ion batteries using graphene coated nickel foam saturated with phase change materials. *International Journal of Thermal Sciences*, *124*, 23–35. https://doi.org/10.1016/j.ijthermalsci.2017.09.019

Jabbari, F., Rajabpour, A., & Saedodin, S. (2021). Thermal conductivity of CNT–water nanofluid at different temperatures, volume fractions, and diameters: experimental investigation and molecular dynamics simulations. *Microfluidics and Nanofluidics*, *25*(12). https://doi.org/10.1007/s10404-021-02489-w

Jaguemont, J., Boulon, L., & Dubé, Y. (2016). A comprehensive review of lithium-ion batteries used in hybrid and electric vehicles at cold temperatures. *Applied Energy*, *164*, 99–114. https://doi.org/10.1016/j.apenergy.2015.11.034

Javani, N., Dincer, I., & Naterer, G. F. (2015). Numerical Modeling of Submodule Heat Transfer With Phase Change Material for Thermal Management of Electric Vehicle Battery Packs. *Journal of Thermal Science and Engineering Applications*, *7*(3). https://doi.org/10.1115/1.4029053

Jiang, G., Huang, J., Liu, M., & Cao, M. (2017). Experiment and simulation of thermal management for a tube-shell Li-ion battery pack with composite phase change material. *Applied Thermal Engineering*, *120*, 1–9. https://doi.org/10.1016/j.applthermaleng.2017.03.107

Jilte, R. D., & Kumar, R. (2018). Numerical investigation on cooling performance of Li-ion battery thermal management system at high galvanostatic discharge. *Engineering Science and Technology, an International Journal*, *21*(5), 957–969. https://doi.org/10.1016/j.jestch.2018.07.015

Julien, C. M., Mauger, A., Zaghib, K., & Groult, H. (2014). Comparative issues of cathode materials for Li-ion batteries. *Inorganics*, *2*(1), 132–154. https://doi.org/10.3390/inorganics2010132

Kalhammer, F. R., Kopf, B. M., Swan, D. H., Roan, V. P., & Walsh, M. P. (2007). Status and Prospects for Zero Emissions Vehicle Technology Report of the ARB Independent Expert Panel 2007. *Prepared for State of California Air Resources Board Sacramento, California*.

Kshetrimayum, K. S., Yoon, Y. G., Gye, H. R., & Lee, C. J. (2019). Preventing heat propagation and thermal runaway in electric vehicle battery modules using integrated PCM and micro-channel plate cooling system. *Applied Thermal Engineering*, *159*, 113797. https://doi.org/10.1016/j.applthermaleng.2019.113797

Mishra, D. K., Bhowmik, C., Bhowmik, S., & Pandey, K. M. (2022). Property-enhanced paraffin-based composite phase change material for thermal energy storage: a review. *Environmental Science and Pollution Research*. https://doi.org/10.1007/s11356-022-19929-x

Larsson, F., Andersson, P., Blomqvist, P., Lorén, A., & Mellander, B. E. (2014). Characteristics of lithium-ion batteries during fire tests. *Journal of Power Sources*, *271*, 414–420. https://doi.org/10.1016/J.JPOWSOUR.2014.08.027

Leising, R. A., Palazzo, M. J., Takeuchi, E. S., & Takeuchi, K. J. (2001). Abuse Testing of Lithium-Ion Batteries: Characterization of the Overcharge Reaction of LiCoO2/Graphite Cells. *Journal of The Electrochemical Society*, *148*(8), A838. https://doi.org/10.1149/1.1379740

Li, H., Duan, Q., Zhao, C., Huang, Z., & Wang, Q. (2019). Experimental investigation on the thermal runaway and its propagation in the large format battery module with Li(Ni1/3Co1/3Mn1/3)O2 as cathode. *Journal of Hazardous Materials*, *375*, 241–254. https://doi.org/10.1016/j.jhazmat.2019.03.116

Li, Q., Shi, H. B., Xie, G., Xie, Z., & Liu, H. ling. (2021). Parametric study and optimization on novel fork-type mini-channel network cooling plates for a Li-ion battery module under high discharge current rates. *International Journal of Energy Research*, *45*(12), 17784–17804. https://doi.org/10.1002/ER.6933

Ling, L., Li, L., Xie, Y., Wang, T., Zheng, K., Shan, S., Zhang, L., Bei, S., & Xu, Q. (2023). Optimal Design of Minichannel Cold Plate for the Thermal Management of Cylindrical Battery Modules. *Energy Technology*, *11*(4). https://doi.org/10.1002/ente.202201484

Ling, Z., Wang, F., Fang, X., Gao, X., & Zhang, Z. (2015). A hybrid thermal management system for lithium ion batteries combining phase change materials with forced-air cooling. *Applied Energy*, *148*, 403–409. https://doi.org/10.1016/j.apenergy.2015.03.080

Liu, G., Ouyang, M., Lu, L., Li, J., & Han, X. (2014). Analysis of the heat generation of lithium-ion battery during charging and discharging considering different influencing factors. *Journal of Thermal Analysis and Calorimetry*, *116*(2), 1001–1010. https://doi.org/10.1007/s10973-013-3599-9

Liu, T., Liu, Y., Wang, X., Kong, X., & Li, G. (2019). Cooling control of thermally-induced thermal runaway in 18,650 lithium ion battery with water mist. *Energy Conversion and Management*, *199*, 111969. https://doi.org/10.1016/j.enconman.2019.111969

Liu, T., Tao, C., & Wang, X. (2020). Cooling control effect of water mist on thermal runaway propagation in lithium ion battery modules. *Applied Energy*, *267*, 115087. https://doi.org/10.1016/j.apenergy.2020.115087

Liu, Y., Duan, Q., Xu, J., Chen, H., Lu, W., & Wang, Q. (2018). Experimental study on the efficiency of dodecafluoro-2-methylpentan-3-one on suppressing lithium-ion battery fires. *RSC Advances*, *8*(73), 42223–42232. https://doi.org/10.1039/C8RA08908F

Liu, Y. P., Ouyang, C. Z., Jiang, Q. B., & Liang, B. (2015). Design and parametric optimization of thermal management of lithium-ion battery module with reciprocating air-flow. *Journal of Central South University*, *22*(10), 3970–3976. https://doi.org/10.1007/s11771-015-2941-8

Liu, Z., Cao, M., Zhang, Y., Li, J., Jiang, G., & Shi, H. (2023). Thermal management of cylindrical battery pack based on a combination of silica gel composite phase change material and copper tube liquid cooling. *Journal of Energy Storage*, *71*. https://doi.org/10.1016/j.est.2023.108205

Mahamud, R., & Park, C. (2011). Reciprocating air flow for Li-ion battery thermal management to improve temperature uniformity. *Journal of Power Sources*, *196*(13), 5685–5696. https://doi.org/10.1016/j.jpowsour.2011.02.076

Maleki, H., & Howard, J. N. (2009). Internal short circuit in Li-ion cells. *Journal of Power Sources*, *191*(2), 568–574. https://doi.org/10.1016/J.JPOWSOUR.2009.02.070

Mao, B., Chen, H., Cui, Z., Wu, T., & Wang, Q. (2018). Failure mechanism of the lithium ion battery during nail penetration. *International Journal of Heat and Mass Transfer*, *122*, 1103–1115. https://doi.org/10.1016/J.IJHEATMASSTRANSFER.2018.02.036

Mao, N., Wang, Z. R., Chung, Y. H., & Shu, C. M. (2019). Overcharge cycling effect on the thermal behavior, structure, and material of lithium-ion batteries. *Applied Thermal Engineering*, *163*, 114147. https://doi.org/10.1016/j.applthermaleng.2019.114147

Menter, F. R. (1994). Two-equation eddy-viscosity turbulence models for engineering applications. *AIAA Journal*, *32*(8), 1598–1605. https://doi.org/10.2514/3.12149

Moffat, R. J. (1988). Describing the uncertainties in experimental results. *Experimental Thermal and Fluid Science*, *1*(1), 3–17. https://doi.org/10.1016/0894-1777(88)90043-X

Mohammed, A. H., Esmaeeli, R., Aliniagerdroudbari, H., Alhadri, M., Hashemi, S. R., Nadkarni, G., & Farhad, S. (2019). Dual-purpose cooling plate for thermal management of prismatic lithium-ion batteries during normal operation and thermal runaway. *Applied Thermal Engineering*, *160*(, 114106. https://doi.org/10.1016/j.applthermaleng.2019.114106

Monika, K., Chakraborty, C., Roy, S., Sujith, R., & Datta, S. P. (2021). A numerical analysis on multi-stage Tesla valve based cold plate for cooling of pouch type Li-ion batteries. *International Journal of Heat and Mass Transfer*, *177*, 121560. https://doi.org/10.1016/j.ijheatmasstransfer.2021.121560

Noh, H. J., Youn, S., Yoon, C. S., & Sun, Y. K. (2013). Comparison of the structural and electrochemical properties of layered Li[NixCoyMnz]O2 (x = 1/3, 0.5, 0.6, 0.7, 0.8 and 0.85) cathode material for lithium-ion batteries. *Journal of Power Sources*, *233*, 121–130. https://doi.org/10.1016/J.JPOWSOUR.2013.01.063

Ohsaki, T., Kishi, T., Kuboki, T., Takami, N., Shimura, N., Sato, Y., Sekino, M., & Satoh, A. (2005). Overcharge reaction of lithium-ion batteries. *Journal of Power Sources*, *146*, 97–100. https://doi.org/10.1016/j.jpowsour.2005.03.105

Ohzuku, T., & Brodd, R. J. (2007). An overview of positive-electrode materials for advanced lithium-ion batteries. *Journal of Power Sources*, *174*(2), 449–456. https://doi.org/10.1016/J.JPOWSOUR.2007.06.154

Omar, N., Monem, M. A., Firouz, Y., Salminen, J., Smekens, J., Hegazy, O., Gaulous, H., Mulder, G., Van den Bossche, P., Coosemans, T., & Mierlo, J. V. (2014). Lithium iron phosphate based battery - Assessment of the aging parameters and development of cycle life model. *Applied Energy*, *113*, 1575–1585. https://doi.org/10.1016/j.apenergy.2013.09.003

Panahi, M., Heydari, H. R., & Karimi, G. (2021). Effects of micro heat pipe arrays on thermal management performance enhancement of cylindrical lithium-ion battery cells. *International Journal of Energy Research*, *45*(7), 11245–11257. https://doi.org/10.1002/ER.6604

Panchal, S., Khasow, R., Dincer, I., Agelin-Chaab, M., Fraser, R., & Fowler, M. (2017). Thermal design and simulation of mini-channel cold plate for water cooled large sized prismatic lithium-ion battery. *Applied Thermal Engineering*, *122*, 80–90. https://doi.org/10.1016/j.applthermaleng.2017.05.010

Panchal, S., Mathewson, S., Fraser, R., Culham, R., & Fowler, M. (2015). Thermal Management of Lithium-Ion Pouch Cell with Indirect Liquid Cooling using Dual Cold Plates Approach. *SAE International Journal of Alternative Powertrains*, *4*(2), 2015-01–1184. https://doi.org/10.4271/2015-01-1184

Park, S., & Jung, D. (2013). Battery cell arrangement and heat transfer fluid effects on the parasitic power consumption and the cell temperature distribution in a hybrid electric vehicle. *Journal of Power Sources*, *227*, 191–198. https://doi.org/10.1016/j.jpowsour.2012.11.039

Peng, P., Wang, Y., & Jiang, F. (2022). Numerical study of PCM thermal behavior of a novel PCM-heat pipe combined system for Li-ion battery thermal management. *Applied Thermal Engineering*, *209*, 118293. https://doi.org/10.1016/J.APPLTHERMALENG.2022.118293

Pourrajab, R., Noghrehabadi, A., Behbahani, M., & Hajidavalloo, E. (2021). An efficient enhancement in thermal conductivity of water-based hybrid nanofluid containing MWCNTs-COOH and Ag nanoparticles: experimental study. *Journal of Thermal Analysis and Calorimetry*, *143*(5), 3331–3343. https://doi.org/10.1007/s10973-020-09300-y

Rao, H., Huang, Z., Zhang, H., & Xiao, S. (2015). Study of fire tests and fire safety measures on lithiumion battery used on ships. *ICTIS 2015 - 3rd International Conference on Transportation Information and Safety, Proceedings*, 865–870. https://doi.org/10.1109/ICTIS.2015.7232158

Rao, Z., Qian, Z., Kuang, Y., & Li, Y. (2017). Thermal performance of liquid cooling based thermal management system for cylindrical lithium-ion battery module with variable contact surface. *Applied Thermal Engineering*, *123*, 1514–1522. https://doi.org/10.1016/j.applthermaleng.2017.06.059

Rao, Z., & Wang, S. (2011). A review of power battery thermal energy management. *Renewable and Sustainable Energy Reviews*, *15*(9), 4554–4571. https://doi.org/10.1016/j.rser.2011.07.096

Rao, Z., Wang, S., & Zhang, G. (2011). Simulation and experiment of thermal energy management with phase change material for ageing LiFePO4 power battery. *Energy Conversion and Management*, *52*(12), 3408–3414. https://doi.org/10.1016/J.ENCONMAN.2011.07.009

Reif, R. H., Liffers, M., Forrester, N., & Peal, K. (2010). Lithium Battery Safety: A look at Woods Hole Oceanographic Institution's Program. *Professional Safety*, *55*(2), 32–37.

Roe, C., Feng, X., White, G., Li, R., Wang, H., Rui, X., Li, C., Zhang, F., Null, V., Parkes, M., Patel, Y., Wang, Y., Wang, H., Ouyang, M., Offer, G., & Wu, B. (2022). Immersion cooling for lithium-ion batteries – A review. In *Journal of Power Sources*, *525*. https://doi.org/10.1016/j.jpowsour.2022.231094

Saw, L. H., Poon, H. M., Thiam, H. S., Cai, Z., Chong, W. T., Pambudi, N. A., & King, Y. J. (2018). Novel thermal management system using mist cooling for lithium-ion battery packs. *Applied Energy*, *223*, 146–158. https://doi.org/10.1016/j.apenergy.2018.04.042

Saw, L. H., Ye, Y., & Tay, A. A. O. (2013). Electrochemical-thermal analysis of 18650 Lithium Iron Phosphate cell. *Energy Conversion and Management*, *75*, 162–174. https://doi.org/10.1016/j.enconman.2013.05.040

Saw, L. H., Ye, Y., Tay, A. A. O., Chong, W. T., Kuan, S. H., & Yew, M. C. (2016). Computational fluid dynamic and thermal analysis of Lithium-ion battery pack with air cooling. *Applied Energy*, *177*, 783–792. https://doi.org/10.1016/j.apenergy.2016.05.122

Saw, L. H., Ye, Y., Yew, M. C., Chong, W. T., Yew, M. K., & Ng, T. C. (2017). Computational fluid dynamics simulation on open cell aluminium foams for Li-ion battery cooling system. *Applied Energy*, *204*, 1489–1499. https://doi.org/10.1016/j.apenergy.2017.04.022

Sefidan, A. M., Sojoudi, A., & Saha, S. C. (2017). Nanofluid-based cooling of cylindrical lithium-ion battery packs employing forced air flow. *International Journal of Thermal Sciences*, *117*, 44–58. https://doi.org/10.1016/j.ijthermalsci.2017.03.006

Shahid, S. (2017). *Development and Analysis of Techniques to Improve Air-cooling and Temperature Uniformity in Battery Packs*.

Shahid, S., & Agelin-Chaab, M. (2017). Analysis of cooling effectiveness and temperature uniformity in a battery pack for cylindrical batteries. *Energies*, *10*(8). https://doi.org/10.3390/en10081157

Shahid, S., & Agelin-Chaab, M. (2018a). Development and analysis of a technique to improve air-cooling and temperature uniformity in a battery pack for cylindrical batteries. *Thermal Science and Engineering Progress*, *5*, 351–363. https://doi.org/10.1016/j.tsep.2018.01.003

Shahid, S., & Agelin-Chaab, M. (2018b). Experimental and numerical studies on air cooling and temperature uniformity in a battery pack. *International Journal of Energy Research*, *42*(6), 2246–2262. https://doi.org/10.1002/er.4018

Shahid, S., & Agelin-Chaab, M. (2019). Application of jets and vortex generators to improve air- cooling and temperature uniformity in a simple battery pack. *Journal of Thermal Science and Engineering Applications*, *11*(2), 1–16. https://doi.org/10.1115/1.4041493

Shahid, S., & Agelin-Chaab, M. (2021). Development of hybrid thermal management techniques for battery packs. *Applied Thermal Engineering*, *186*, 116542. https://doi.org/10.1016/j.applthermaleng.2020.116542

Shahid, S., & Agelin-Chaab, M. (2022). A review of thermal runaway prevention and mitigation strategies for lithium-ion batteries. *Energy Conversion and Management: X*, *16*, 100310. https://doi.org/10.1016/J.ECMX.2022.100310

Shahid, S., & Agelin-Chaab, M. (2023a). Comparison between Different PCM Mediums and Dielectric Fluid for Hybrid Thermal Management of Electric Battery Packs. *Journal of Fluid Flow, Heat and Mass Transfer*, *10*, 61–68. https://doi.org/10.11159/jffhmt.2023.009

Shahid, S., & Agelin-Chaab, M. (2023b). Comparison of Hybrid Cooling Concepts with PCM Cooling for Electric Battery Packs. *Journal of Fluid Flow, Heat and Mass Transfer*, *10*, 69–77. https://doi.org/10.11159/jffhmt.2023.010

Shahid, S., & Agelin-Chaab, M. (2023c). Development and analysis of hybrid cooling concepts for an electric battery pack. *Journal of Energy Storage*, *73*. https://doi.org/10.1016/j.est.2023.108952

Shahid, S., & Agelin-Chaab, M. (2023d). Experimental and Numerical Analysis of a Hybrid Thermal Management Concept at Different Discharge Rates for a Cylindrical Li-Ion Battery Module. *Batteries*, *9*(9). https://doi.org/10.3390/batteries9090474

Shan, C., Guanghui, G., & Fangfang, L. (2014). Study on the performance of LiMn2O4 using spent Zn-Mn batteries as manganese source. *Journal of Solid State Electrochemistry*, *18*(6), 1495–1502. https://doi.org/10.1007/s10008-013-2311-0

Shan, X. Y., Li, F., Wang, D. W., & Cheng, H. M. (2016). The smart era of electrochemical energy storage devices. *Energy Storage Materials*, *3*, 66–68. https://doi.org/10.1016/J.ENSM.2016.01.005

Smith, K., & Wang, C. Y. (2006). Power and thermal characterization of a lithium-ion battery pack for hybrid-electric vehicles. *Journal of Power Sources*, *160*(1), 662–673. https://doi.org/10.1016/j.jpowsour.2006.01.038

Spotnitz, R., & Franklin, J. (2003). Abuse behavior of high-power, lithium-ion cells. *Journal of Power Sources*, *113*(1), 81–100. https://doi.org/10.1016/S0378-7753(02)00488-3

Patil, M. S., Seo, J. H., & Lee, M. Y. (2020). A novel dielectric fluid immersion cooling technology for Li-ion battery thermal management. *Energy Conversion and Management, 229,* 113715. https://doi.org/10.1016/j.enconman.2020.113715

Tesla Model S/X Pack - 75kWh / 214Ah / 350V. (n.d.). Retrieved September 27, 2023, from https://www.secondlife-evbatteries.com/products/tesla-75kw-pack

Tong, W., Somasundaram, K., Birgersson, E., Mujumdar, A. S., & Yap, C. (2016). Thermo-electrochemical model for forced convection air cooling of a lithium-ion battery module. *Applied Thermal Engineering*, *99*, 672–682. https://doi.org/10.1016/j.applthermaleng.2016.01.050

Schalkwijk, W. V., & Scrosati, B. (2002). Advances in Lithium Ion Batteries Introduction. *Advances in Lithium-Ion Batteries*, 1–5. https://doi.org/10.1007/0-306-47508-1_1

Vendra, C. M. R., Shelke, A. V., Buston, J. E. H., Gill, J., Howard, D., Read, E., Abaza, A., Cooper, B., & Wen, J. X. (2022). Numerical and experimental characterisation of high energy density 21700 lithium-ion battery fires. *Process Safety and Environmental Protection*, *160*, 153–165. https://doi.org/10.1016/J.PSEP.2022.02.014

Wang, Q., Li, K., Wang, Y., Chen, H., Duan, Q., & Sun, J. (2018). The Efficiency of Dodecafluoro-2-Methylpentan-3-One on Suppressing the Lithium Ion Battery Fire. *Journal of Electrochemical Energy Conversion and Storage*, *15*(4). https://doi.org/10.1115/1.4039418

Wang, Q., Shao, G., Duan, Q., Chen, M., Li, Y., Wu, K., Liu, B., Peng, P., & Sun, J. (2015). The Efficiency of Heptafluoropropane Fire Extinguishing Agent on Suppressing the Lithium Titanate Battery Fire. *Fire Technology*, *52*(2), 387–396. https://doi.org/10.1007/S10694-015-0531-9

Wang, S., Li, Y., Li, Y. Z., Mao, Y., Zhang, Y., Guo, W., & Zhong, M. (2017). A forced gas cooling circle packaging with liquid cooling plate for the thermal management of Li-ion batteries under space environment. *Applied Thermal Engineering*, *123*, 929–939. https://doi.org/10.1016/j.applthermaleng.2017.05.159

Wang, T., Tseng, K. J., & Zhao, J. (2015). Development of efficient air-cooling strategies for lithium-ion battery module based on empirical heat source model. *Applied Thermal Engineering*, *90*, 521–529. https://doi.org/10.1016/j.applthermaleng.2015.07.033

Wang, T., Tseng, K. J., Zhao, J., & Wei, Z. (2014). Thermal investigation of lithium-ion battery module with different cell arrangement structures and forced air-cooling strategies. *Applied Energy*, *134*, 229–238. https://doi.org/10.1016/j.apenergy.2014.08.013

Wei, Y. (2018). *Development and Experimental Analysis of a Novel Hybrid Cooling Concept for Electric Vehicle Batteries*.

Wei, Y., & Agelin-Chaab, M. (2018). Experimental investigation of a novel hybrid cooling method for lithium-ion batteries. *Applied Thermal Engineering*, *136*, 375–387. https://doi.org/10.1016/j.applthermaleng.2018.03.024

Wei, Y., & Agelin-Chaab, M. (2019). Development and experimental analysis of a hybrid cooling concept for electric vehicle battery packs. *Journal of Energy Storage*, *25*, 100906. https://doi.org/10.1016/j.est.2019.100906

Weng, J., Ouyang, D., Liu, Y., Chen, M., Li, Y., Huang, X., & Wang, J. (2021). Alleviation on battery thermal runaway propagation: Effects of oxygen level and dilution gas. *Journal of Power Sources*, *509*. https://doi.org/10.1016/j.jpowsour.2021.230340

Weng, J., Ouyang, D., Yang, X., Chen, M., Zhang, G., & Wang, J. (2019). Alleviation of thermal runaway propagation in thermal management modules using aerogel felt coupled with flame-retarded phase change material. *Energy Conversion and Management*, *200*, 112071. https://doi.org/10.1016/j.enconman.2019.112071

Weng, J., Xiao, C., Ouyang, D., Yang, X., Chen, M., Zhang, G., Yuen, R. K. K., & Wang, J. (2022). Mitigation effects on thermal runaway propagation of structure-enhanced phase change material modules with flame retardant additives. *Energy*, *239*. https://doi.org/10.1016/j.energy.2021.122087

Wilke, S., Schweitzer, B., Khateeb, S., & Al-Hallaj, S. (2017). Preventing thermal runaway propagation in lithium ion battery packs using a phase change composite material: An experimental study. *Journal of Power Sources*, *340*, 51–59. https://doi.org/10.1016/j.jpowsour.2016.11.018

Wu, T., Chen, H., Wang, Q., & Sun, J. (2018). Comparison analysis on the thermal runaway of lithium-ion battery under two heating modes. *Journal of Hazardous Materials*, *344*, 733–741. https://doi.org/10.1016/j.jhazmat.2017.11.022

Wu, W., Wu, W., & Wang, S. (2017). Thermal optimization of composite PCM based large-format lithium-ion battery modules under extreme operating conditions. *Energy Conversion and Management*, *153*, 22–33. https://doi.org/10.1016/j.enconman.2017.09.068

Xiong, X., Wang, Z., Fan, Y., & Wang, H. (2023). Numerical analysis of cylindrical lithium-ion battery thermal management system based on bionic flow channel structure. *Thermal Science and Engineering Progress*, *42*. https://doi.org/10.1016/j.tsep.2023.101879

Xu, J., Guo, P., Duan, Q., Yu, X., Zhang, L., Liu, Y., & Wang, Q. (2020). Experimental study of the effectiveness of three kinds of extinguishing agents on suppressing lithium-ion battery fires. *Applied Thermal Engineering*, *171*, 115076. https://doi.org/10.1016/J.APPLTHERMALENG.2020.115076

Xu, Q., Xie, Y., Huang, Y., Li, X., Huang, H., Bei, S., Wang, H., Zheng, K., Wang, X., & Li, L. (2023). Enhancement of thermal management for cylindrical battery module based on a novel wrench-shaped design for the cold plate. *Sustainable Energy Technologies and Assessments*, *59*. https://doi.org/10.1016/j.seta.2023.103421

Yamauchi, T., Mizushima, K., Satoh, Y., & Yamada, S. (2004). Development of a simulator for both property and safety of a lithium secondary battery. *Journal of Power Sources*, *136*(1), 99–107. https://doi.org/10.1016/J.JPOWSOUR.2004.05.011

Yang, N., Zhang, X., Li, G., & Hua, D. (2015). Assessment of the forced air-cooling performance for cylindrical lithium-ion battery packs: A comparative analysis between aligned and staggered cell arrangements. *Applied Thermal Engineering*, *80*, 55–65. https://doi.org/10.1016/j.applthermaleng.2015.01.049

Yang, T., Yang, N., Zhang, X., & Li, G. (2016). Investigation of the thermal performance of axial-flow air cooling for the lithium-ion battery pack. *International Journal of Thermal Sciences*, *108*, 132–144. https://doi.org/10.1016/j.ijthermalsci.2016.05.009

Ye, J., Chen, H., Wang, Q., Huang, P., Sun, J., & Lo, S. (2016). Thermal behavior and failure mechanism of lithium ion cells during overcharge under adiabatic conditions. *Applied Energy*, *182*, 464–474. https://doi.org/10.1016/j.apenergy.2016.08.124

Yeh, W. T., Huang, Y. F., Wu, C. C., & Hong, P. D. (2022). Structure and morphological changes of multilayer separators for lithium-ion batteries under abuse/overcharge conditions. *Journal of Applied Polymer Science*, *139*(17), 52046. https://doi.org/10.1002/APP.52046

Yoshio, M., Brodd, R. J., & Kozawa, A. (2009). Lithium-ion batteries: Science and technologies. *Lithium-Ion Batteries: Science and Technologies*. https://doi.org/10.1007/978-0-387-34445-4/COVER

Yuan, Q. F., Zhao, F., Wang, W., Zhao, Y., Liang, Z., & Yan, D. (2015). Overcharge failure investigation of lithium-ion batteries. *Electrochimica Acta*, *178*, 682–688. https://doi.org/10.1016/j.electacta.2015.07.147

Zavalis, T. G., Behm, M., & Lindbergh, G. (2012). Investigation of Short-Circuit Scenarios in a Lithium-Ion Battery Cell. *Journal of The Electrochemical Society*, *159*(6), A848. https://doi.org/10.1149/2.096206JES

Zeng, W., Niu, Y., Li, S., Hu, S., Mao, B., & Zhang, Y. (2022). Cooling performance and optimization of a new hybrid thermal management system of cylindrical battery. *Applied Thermal Engineering*, *217*. https://doi.org/10.1016/j.applthermaleng.2022.119171

Zeng, Y., Wu, K., Wang, D., Wang, Z., & Chen, L. (2006). Overcharge investigation of lithium-ion polymer batteries. *Journal of Power Sources*, *160*, 1302–1307. https://doi.org/10.1016/j.jpowsour.2006.02.009

Zhang, H., Wu, X., Wu, Q., & Xu, S. (2019). Experimental investigation of thermal performance of large-sized battery module using hybrid PCM and bottom liquid cooling configuration. *Applied Thermal Engineering*, *159*, 113968. https://doi.org/10.1016/j.applthermaleng.2019.113968

Zhang, L., Duan, Q., Liu, Y., Xu, J., Sun, J., Xiao, H., & Wang, Q. (2021). Experimental investigation of water spray on suppressing lithium-ion battery fires. *Fire Safety Journal*, *120*, 103117. https://doi.org/10.1016/j.firesaf.2020.103117

Zhang, L., Li, Y., Duan, Q., Chen, M., Xu, J., Zhao, C., Sun, J., & Wang, Q. (2020). Experimental study on the synergistic effect of gas extinguishing agents and water mist on suppressing lithium-ion battery fires. *Journal of Energy Storage*, *32*, 101801. https://doi.org/10.1016/j.est.2020.101801

Zhang, S. S. (2007). A review on the separators of liquid electrolyte Li-ion batteries. *Journal of Power Sources*, *164*(1), 351–364. https://doi.org/10.1016/J.JPOWSOUR.2006.10.065

Zhang, W., Liang, Z., Yin, X., & Ling, G. (2021). Avoiding thermal runaway propagation of lithium-ion battery modules by using hybrid phase change material and liquid cooling. *Applied Thermal Engineering*, *184*, 116380. https://doi.org/10.1016/j.applthermaleng.2020.116380

Zhao, C., Kang, W., Zhao, S., & Shen, Q. (2011). Hydrazine-hydrothermal synthesis of pure-phase O-LiMnO2 for lithium-ion battery application. *Micro and Nano Letters*, *6*(10), 820–822. https://doi.org/10.1049/mnl.2011.0378

Zhao, C., Sousa, A. C. M., & Jiang, F. (2019). Minimization of thermal non-uniformity in lithium-ion battery pack cooled by channeled liquid flow. *International Journal of Heat and Mass Transfer*, *129*, 660–670. https://doi.org/10.1016/j.ijheatmasstransfer.2018.10.017

Zhao, C., Sun, J., & Wang, Q. (2020). Thermal runaway hazards investigation on 18650 lithium-ion battery using extended volume accelerating rate calorimeter. *Journal of Energy Storage*, *28*, 101232. https://doi.org/10.1016/j.est.2020.101232

Zhao, J., Lv, P., & Rao, Z. (2017). Experimental study on the thermal management performance of phase change material coupled with heat pipe for cylindrical power battery pack. *Experimental Thermal and Fluid Science*, *82*, 182–188. https://doi.org/10.1016/j.expthermflusci.2016.11.017

Zhao, J., Rao, Z., Huo, Y., Liu, X., & Li, Y. (2015). Thermal management of cylindrical power battery module for extending the life of new energy electric vehicles. *Applied Thermal Engineering*, *85*, 33–43. https://doi.org/10.1016/j.applthermaleng.2015.04.012

Zhao, J., Rao, Z., & Li, Y. (2015). Thermal performance of mini-channel liquid cooled cylinder based battery thermal management for cylindrical lithium-ion power battery. *Energy Conversion and Management*, *103*, 157–165. https://doi.org/10.1016/j.enconman.2015.06.056

Zhao, R., Liu, J., & Gu, J. (2016). Simulation and experimental study on lithium ion battery short circuit. *Applied Energy*, *173*, 29–39. https://doi.org/10.1016/j.apenergy.2016.04.016

Zhi, W., & Jian, W. (2020). Investigation of external heating-induced failure propagation behaviors in large-size cell modules with different phase change materials. *Energy*, *204*, 117946. https://doi.org/10.1016/j.energy.2020.117946

Zhong, G., Li, H., Wang, C., Xu, K., & Wang, Q. (2018). Experimental Analysis of Thermal Runaway Propagation Risk within 18650 Lithium-Ion Battery Modules. *Journal of The Electrochemical Society*, *165*(9), A1925–A1934. https://doi.org/10.1149/2.0461809jes

Zhou, H., Zhou, F., Xu, L., Kong, J., & Yang, Q. (2019). Thermal performance of cylindrical Lithium-ion battery thermal management system based on air distribution pipe. *International Journal of Heat and Mass Transfer*, *131*, 984–998. https://doi.org/10.1016/j.ijheatmasstransfer.2018.11.116

Zhu, F., Du, X., Lei, J., Audisio, L., & Sypeck, D. (2020). Experimental study on the crushing behaviour of lithium-ion battery modules. *International Journal of Crashworthiness*, 1–10. https://doi.org/10.1080/13588265.2020.1766397

Zhu, F., Zhou, R., Sypeck, D., Deng, J., & Bae, C. (2022). Failure behavior of prismatic Li-ion battery cells under abuse loading condition - A combined experimental and computational study. *Journal of Energy Storage*, *48*, 103969. https://doi.org/10.1016/J.EST.2022.103969

Zhu, M. X., Zhu, S. B., Gong, J. H., & Zhou, Z. (2018). Experimental Study on Fire and Explosion Characteristics of Power Lithium Batteries with Surfactant Water Mist. *Procedia Engineering*, *211*, 1083–1090. https://doi.org/10.1016/J.PROENG.2017.12.113